POLYTECHNIQUE MONTRÉAL
affiliée à l'Université de Montréal

Evaluation of existing constitutive models in nonlinear 1D effective stress ground response analysis

CAROLINE BESSETTE
Département des Génies Civil, Géologique et des Mines

Mémoire présenté en vue de l'obtention du diplôme de *Maîtrise ès sciences appliquées*
génie civil

Janvier 2020

© Caroline Bessette, 2020.

POLYTECHNIQUE MONTRÉAL
affiliée à l'Université de Montréal

Ce mémoire intitulé :

Evaluation of existing constitutive models in nonlinear 1D effective stress ground response analysis

présenté par **Caroline BESSETTE**
en vue de l'obtention du diplôme de *Maîtrise ès sciences appliquées*
a été dûment accepté par le jury d'examen constitué de :

Benoît COURCELLES, président
Samuel YNIESTA, membre et directeur de recherche
Carlos OVALLE, membre

ACKNOWLEDGEMENTS

The author would first like to acknowledge the following for providing the strong motion data, site profiles and properties for this study: The National Research Institute for Earth Science and Disaster Prevention (NIED) – KiK-net sites *KSRH07 & TCGH16*, The Earthquake Engineering Group, Earth Research Institute at University of California, Santa Barbara and United States Geotechnical Survey (USGS) – *Wildlife Liquefaction Array*, Center for Earthquake Engineering Simulation (CEES), Network for Earthquake Engineering Simulation (NEES), and Professor Scott J. Brandenberg at University of California, Los Angeles – *CSP3 centrifuge experiment*, Professor Shideh Dashti at the University of Colorado Boulder, Boulder – *CFF2 centrifuge experiment* [1], Professor Ahmed-Waeil Elgamal at the University of California, San Diego & the Electric Power Research Institute (EPRI) – *Lotung Array (LSST)* and Recorded by Kobe-city and provided by the GeoResearch Institute and Yoshinori Iwasaki – *Port Island Downhole Array (PIDA)*.

I would also wish to thank my thesis advisor, Professor Samuel Yniesta, for his continuous support, guidance, and for introducing me to geotechnical earthquake engineering and research in the first place. His valuable comments on my work have always steered me in the right direction whenever needed and helped me towards the success of this study. Thanks to my fellow student colleagues Mohammad Zarrabi and Jessica Huo-Kang, and all my friends from undergraduate studies for their help and support. Finally, I would like to express my profound gratitude to my parents, Josée Surprenant and Robert Bessette, and my sister, Stéphanie Bessette, for their unconditional love and support throughout all of my studies.

ABSTRACT

The National Building Code of Canada recommends that effective stress ground response analysis be performed if a liquefiable stratum is identified within a soil profile. While constitutive models for total stress ground response analysis have been well verified against earthquake recordings, existing models for effective stress ground response analysis have yet to be thoroughly validated. The present research project investigates the predictions of five constitutive models derived for effective stress ground response analysis. The recordings from seven liquefaction case histories are used, including data from downhole arrays and centrifuge experimental results, where the potential for liquefaction was identified during at least one earthquake. The ground motion records were selected to represent varying ground motion intensity and excess-pore pressure generation levels. The difference between predictions of the effective stress models against commonly used one dimensional ground response total stress equivalent-linear and nonlinear analyses are evaluated. The predicted and measured motions are compared in terms of spectral response and ratio of surface to downhole amplification spectra. The pore pressure response of all constitutive models is evaluated as a function of time and shear strain and compared with the expected behavior of liquefiable soils. Finally, the performance of each analyses is evaluated through the prediction of common ground motion parameters such as the Arias intensity, significant durations, number of equivalent loading cycles, cumulative absolute velocity, shaking intensity rate and characteristic periods. The results indicate that existing models are limited in their predictive capabilities, and that effective stress ground analysis is not yet a satisfying tool for practicing engineers. In general, total stress simulations were found to be at least as precise as the effective stress simulations. The available models also showed the ability of capturing liquefaction when it was triggered. In addition, the findings of this study highlight the need to address current limitations of these models in term of the selection of input parameters and the consideration of dilative behavior.

RÉSUMÉ

Le Code National du Bâtiment Canadien recommande de réaliser une analyse de réponse de sol en contraintes effectives lorsqu'un potentiel de liquéfaction est identifé dans un profil de sol. Alors que les modèles constitutifs pour l'analyse de réponse de sol en contraintes totales ont été validés de façon exhaustive par l'entremise de plusieurs enregistrements de séismes, les modèles en contraintes effectives n'ont pas encore été complètement validés. La présente étude évalue les prévisions de cinq modèles constitutifs dérivés pour l'analyse de réponse de sol en contraintes effectives. Les enregistrements de sept études de cas de liquéfaction sont utilisés, incluant des données de stations d'accéléromètres et d'essais en centrifugeuse, où un potentiel de liquéfaction a été identifié pendant au moins un séisme. Des séismes d'intensités sismiques et de potentiels de génération de surpressions interstitielles variés ont été sélectionnés. Les prévisions des analyses en contraintes effectives sont comparées à des analyses linéaires et non-linéaires en contraintes totales. Les réponses prédites et mesurées sont comparées en terme de réponse spectrale et du ratio de surface à profondeur des spectres d'amplification. La réponse de pression interstitielle de tous les modèles constitutifs est évaluée en fonction du temps et de la contrainte de cisaillement et comparée au comportement attendu des sols liquéfiables. Enfin, la performance de chaque analyse est évaluée par l'entremise de paramètres de mouvement du sol communément utilisés, tels que l'intensité d'Arias, les durées significatives, le nombre de cycles de chargement équivalents, la vitesse absolue cumulée, le taux d'intensité de secousse sismique et les périodes caractéristiques. Les résultats indiquent que les capacités prédictives des modèles existants sont limitées et que l'analyse en contraintes effectives ne constitue pas encore un outil satisfaisant pour être utilisée par les ingénieurs en pratique. En général, la précision des modèles en contraintes totales s'est avérée au moins aussi précise que les méthodes en contraintes effectives. Or, les modèles disponibles démontrent la capacité de capturer la liquéfaction lors de son déclenchement de même que la génération de surpressions interstitielles. En outre, les résultats de cette étude soulignent la nécessité d'adresser les limites actuelles de ces modèles en termes de sélection des paramètres d'entrée des modèles et de la prise en considération des mécanismes de dilatation.

TABLE OF CONTENTS

ACKNOWLEDGEMENTS iii

ABSTRACT iv

RÉSUMÉ v

TABLE OF CONTENTS vi

LIST OF TABLES ix

LIST OF FIGURES x

LIST OF APPENDICES xiii

CHAPTER 1 INTRODUCTION 1
1.1 Background and motivation 1
1.2 Research objectives and methodology 2
1.3 Organization of thesis 3

CHAPTER 2 EFFECTIVE STRESS ANALYSIS 5
2.1 Excess pore water pressure generation and liquefaction 5
2.2 Cyclic degradation due to excess pore water pressure generation 6
2.3 Dissipation and redistribution 6
2.4 Pore pressure generation models 7
2.4.1 Granular soils 7
2.4.2 Cohesive soils 9
2.4.3 Limitations 9
2.5 Past validation studies 10

CHAPTER 3 SITE SELECTION 12
3.1 Time-frequency analysis 13
3.2 Simplified liquefaction analysis 14
3.3 Description of the case studies 15
3.3.1 KSRH07 15
3.3.2 TCGH16 16
3.3.3 Wildlife Liquefaction Array 19

3.3.4 Lotung (LSST) . . . 21
3.3.5 Port-Island Downhole Array (PIDA) . . . 22
3.3.6 CSP3 . . . 25
3.3.7 CFF2 . . . 26

CHAPTER 4 METHODS . . . 27
4.1 Site response analysis parameters . . . 27
4.1.1 Layer thickness . . . 27
4.1.2 Modulus reduction and damping curves . . . 27
4.1.3 Nonlinear soil constitutive model . . . 28
4.1.4 Input earthquake motions and boundary condition . . . 28
4.1.5 Additional notes . . . 29
4.2 Effective stress analysis - Calibration of the input parameters . . . 30
4.2.1 Dobry & Matasovic (1988) . . . 31
4.2.2 Green-Mitchell-Polito - GMP (2000) . . . 32
4.2.3 Park and Ahn (2013) . . . 32
4.2.4 Generalized (1985) . . . 34
4.2.5 Matasovic & Vucetic (1995) . . . 35
4.2.6 Degradation parameter . . . 35
4.2.7 Dissipation and redistribution parameters . . . 36

CHAPTER 5 RESULTS AND DISCUSSION . . . 37
5.1 Wildlife Liquefaction Array (WLA) case study . . . 37
5.2 Centrifuge tests . . . 39
5.2.1 CSP3 . . . 39
5.2.2 CFF2 . . . 41
5.2.3 Modifications to the site properties . . . 43
5.3 Validity of 1D assumptions of the sites . . . 44
5.4 Quantification of uncertainty . . . 45
5.5 Accuracy of the predictions . . . 51
5.5.1 Level of nonlinearity . . . 52
5.5.2 Site . . . 55
5.5.3 Pore pressure ratio . . . 56
5.5.4 Comparison of the calibrations of the effective stress models . . . 57
5.6 Pore pressure response of the considered models . . . 58
5.6.1 Maximum shear strain . . . 58
5.6.2 Time . . . 60

5.7 Ground motion parameters comparison 62
5.7.1 Arias intensity - AI 62
5.7.2 Significant durations - D_{5-95} and D_{25-75} 65
5.7.3 Number of equivalent loading cycles - N_{eq} 66
5.7.4 Cumulative absolute velocity - CAV & CAV_{STD} 67
5.7.5 Shakin intensity Rate - SIR 71
5.7.6 Frequency content - T_m, T_o, and T_p 72
5.7.7 Comparison against PGA, PGV, and $PSA(T)$ for each scenario . . . 76
5.7.8 Summary 80
5.8 Limitations 83

CHAPTER 6 CONCLUSION 85

BIBLIOGRAPHY 87

APPENDICES 104

LIST OF TABLES

Table 2.1	Modulus and shear stress degradation index functions	6
Table 4.1	Pore pressure generation models and input parameters	31
Table 5.1	Description of the motions considered at each site for the two analyzed scenarios	44
Table 5.2	Computed standard deviations and correlation coefficients at each site	45
Table 5.3	Ground motion parameter prediction: min, max, and std. deviation for scenario 1	78
Table 5.4	Ground motion parameter prediction: min, max, and std. deviation for scenario 2	79
Table S1	Detailed list of input motions and properties	104
Table S2	Effective Stress Analysis – List of the calibrations for all sites	105

LIST OF FIGURES

Figure 3.1 Shear wave velocity profiles of the 7 selected sites 12
Figure 3.2 Distribution of the magnitude and surface PGA versus the observed surface PGA and V_{S30} (respectively) for the 98 ground motions . . . 13
Figure 3.3 Normalized Stockwell Transform of the 2011 Tohoku Earthquake (NS component) at site TCGH16 14
Figure 3.4 Probability of liquefaction versus the observed PGA at the ground surface 15
Figure 3.5 Station KSRH07 - Geological and velocity profiles description 17
Figure 3.6 Station TCGH16 - Geological and velocity profiles description 18
Figure 3.7 Wildlife Liquefaction Array (WLA) profile description 19
Figure 3.8 Wildlife Liquefaction Array - Instrumentation 20
Figure 3.9 Lotung Array - Geological and velocity profile description 22
Figure 3.10 Port Island Downhole Array (PIDA) - Geological and velocity profile description 24
Figure 3.11 Centrifuge test CSP3 model layout 25
Figure 3.12 Centrifuge test CFF2 model layout 26
Figure 4.1 Example of the Park and Ahn calibration at the WLA site 34
Figure 5.1 Results for the Wildlife Liquefaction Array for the Superstition Hills Earthquake (M2.1) 38
Figure 5.2 Results for centrifuge test CSP3 EQ#4 (M1.1) 40
Figure 5.3 Results for centrifuge test CFF2 EQ#1 (M1.1) 41
Figure 5.4 Results for centrifuge test CFF2 EQ#2 (M1.1) 42
Figure 5.5 Median empirical transfer function (ETF), 95% confidence interval and $SH1D$ at each site. 46
Figure 5.6 Period dependence of the mixed effect regression analysis for the NL-ES analysis and the calibrations 48
Figure 5.7 Period dependence of the mixed effect regression analysis for the EQL, NL-TS and NL-ES analysis for scenario 1 49
Figure 5.8 Period dependence of the mixed effect regression analysis for the EQL, NL-TS and NL-ES analysis for scenario 2 50
Figure 5.9 Correlation coefficients between the observed and predicted amplification spectra for EQL, NL-TS and NL-ES analyses as a function of the shear strain ratio I_γ computed from the Fourier Amplitude Ratio. . . 52

Figure 5.10 Correlation coefficients between the observed and predicted amplification spectra for EQL, NL-TS and NL-ES analyses as a function of the shear strain ratio I_γ for each event computed from the Fourier Amplitude Ratio 54
Figure 5.11 Correlation coefficients between the observed and predicted amplification spectra for NL-ES analysis as a function of the shear strain ratio I_γ for each event computed from the Fourier amplitude ratio for the centrifuge tests. 54
Figure 5.12 Correlation coefficients between the observed and predicted amplification spectra for EQL, NL-TS and NL-ES analyses binned by sites. . . 55
Figure 5.13 Comparison of correlation coefficients between the observed and predicted spectra for NL-ES analysis (M1, M2, M3, M4) based on the estimated pore pressure ratio r_u 56
Figure 5.14 Correlation coefficients between the observed and predicted amplification spectra for the individual calibrations of NL-ES analyses binned by the shear strain ratio I_γ. 57
Figure 5.15 Pore pressure response versus the maximum computed shear strains in effective stress analysis for calibrations M1.1, M2.1, M3.1 and M4.1. . 59
Figure 5.16 Pore pressure response vs the maximum computed shear strain for the Park and Ahn model calibration M3.6. 60
Figure 5.17 Predicted and observed pore pressure response as a function of time – Site CSP3: (a) PPT52 – 1.1m, (b) PPT55 – 6.82 m. 61
Figure 5.18 Arias intensity residuals as a function of the shear strain index I_γ for EQL, NL-TS, and NL-ES. 64
Figure 5.19 Arias intensity (AI) residuals as a function of the shear strain index I_γ for the NL-ES calibrations. 64
Figure 5.20 Significant duration D_{5-95} and D_{25-75} residuals as a function of the observed downhole shear strain index I_γ for EQL, NL-TS, and NL-ES analyses. 66
Figure 5.21 Significant duration D_{5-95} residuals as a function of the observed downhole shear strain index I_γ for NL-ES analysis per calibration. 66
Figure 5.22 Number of equivalent loading cycles N_{eq} residuals as a function of the observed downhole shear strain index I_γ for EQL, NL-TS, and NL-ES analyses. 67

Figure 5.23 Number of equivalent loading cycles N_{eq} residuals as a function of the observed downhole shear strain index I_γ for NL-ES analysis per calibration. 68

Figure 5.24 Cumulative Absolute Velocity Residuals as a function of the observed downhole shear strain index I_γ for EQL, NL-TS and NL-ES analyses. 70

Figure 5.25 Cumulative absolute velocity (a) CAV & (b) CAV_{STD} residuals as a function of the observed downhole shear strain index I_γ for NL-ES analysis per calibration. 70

Figure 5.26 Shaking intensity Rate residuals as a function of the observed downhole shear strain index I_γ for EQL, NL-TS and NL-ES analyses. 71

Figure 5.27 Shaking intensity Rate residuals as a function of the observed downhole shear strain index I_γ for NL-ES analysis per calibration. 72

Figure 5.28 Residuals (a) and Ratio ratio of surface to downhole (b) of T_m as a function of the observed downhole shear strain index I_γ for EQL, NL-TS, and NL-ES analyses. 74

Figure 5.29 Residuals (a-b) and Ratio ratio of surface to downhole (c-d) of T_o and T_p as a function of the observed downhole shear strain index I_γ for EQL, NL-TS, and NL-ES analyses. 75

Figure 5.30 Ratio of surface to downhole of T_m, T_o, and T_p as a function of the observed downhole shear strain index I_γ for NL-ES analysis per calibration. 76

Figure 5.33 Residuals of parameters AI, D_{5-95}, D_{25-75}, N_{eq}, CAV as a function of I_γ, PGA, PGV, $PSA_{T=0.1s}$, and $PSA_{T=1s}$ – scenario 2. 78

Figure 5.34 Residuals of parameters CAV_{STD}, SIR, T_m, T_o, and T_p as a function of I_γ, PGA, PGV, $PSA_{T=0.1s}$, and $PSA_{T=1s}$ – scenario 2. 79

Figure 5.31 Residuals of parameters AI, D_{5-95}, D_{25-75}, N_{eq}, CAV as a function of I_γ, PGA, PGV, $PSA_{T=0.1s}$, and $PSA_{T=1s}$ – scenario 1. 80

Figure 5.32 Residuals of parameters CAV_{STD}, SIR T_m, T_o, and T_p as a function of I_γ, PGA, PGV, $PSA_{T=0.1s}$, and $PSA_{T=1s}$ – scenario 1. 81

Figure 5.35 Range of residuals for each ground motion parameter for the EQL and NL-TS analyses for scenario 1. 81

Figure S1 Results for the centrifuge test CFF2 EQ#4 (M1.1) 106

Figure S2 Pore pressure response vs the maximum computed shear strain for the Generalized model calibration M1.5. 107

Figure S3 Pore pressure response vs the maximum computed shear strain for the Dobry and Matasovic model calibration M4.5. 107

LIST OF APPENDICES

Appendix A – Supplementary Material 104

CHAPTER 1 INTRODUCTION

1.1 Background and motivation

One-dimensional ground response analyses are used to study the potential of amplification of vertically propagating horizontal shear waves in horizontally layered deposits. Several methods of analysis can be used, such as the equivalent linear and the nonlinear analysis. Equivalent-linear analyses can be performed in both time or frequency domain and are based on the work of [2] and [3], and is implemented in the SHAKE [4] program. In this approach, an iterative procedure is used to adjust the shear modulus and damping ratio as a function of equivalent shear strain which depends on the maximum shear strain reached during the analysis. The input properties are the shear-wave velocity V_S, mass density ρ, and modulus reduction and damping curves (MRD curves). In the nonlinear analysis, the soil can be represented as a multiple-degree of freedom lumped mass system (MDOF), or as a continuum discretized into finite elements, and the dynamic equation of motion is solved using a numerical time-stepping procedure such as the Newmark β method [5]. In addition to the parameters listed above for the equivalent-linear analysis, nonlinear analyses require a soil constitutive model, which usually consists of a set of unload-reload rules and a functional form of the backbone curve for the initial loading. Regarding the application of the two approaches, the equivalent-linear analysis is considered easier to use since it benefits from low computational efforts and few input parameters [6]. However, previous researchers have proven that the equivalent linear method introduces significant bias when modeling motions that induce shear strain (γ_{max}) levels greater than 0.05% [7], and recommended that nonlinear analysis should be prioritized. Several other studies have reached similar conclusions when studying ground response analysis [8–15].

While both approaches can be performed in the total stress formulation, only the nonlinear approach can integrate an effective stress formulation, which allows for the consideration of generation, redistribution, and dissipation of the excess pore water pressures. Under cyclic loading, excess pore pressure buildup can result in the cancellation of the effective confining pressure and a loss of stiffness and strength called liquefaction [16]. Consequently, the National Building Code of Canada recommends that a site-specific effective ground response analysis be conducted when a liquefiable layer is identified within a soil profile. However, despite this recommendation, total stress equivalent-linear and nonlinear analyses have remained the standard of practice and the main focus of research. In contrast, effective stress models have received much less attention, and their application in practice remains challeng-

ing due to several limitations that have yet to be thoroughly investigated. These limitations include the poor accuracy of the predictions of the existing models, the difficulty in the selection of input parameters and the poor modeling of the dilatation behavior or other in-situ effects, such as void redistribution, stratified soil effects, initial static stresses, etc. [17]. Previous work has focused on the validation of these models against motions triggering liquefaction and their application to lower amplitude motions has mostly been overlooked.

1.2 Research objectives and methodology

In this study, the validation of effective stress models in 1D ground response analysis is performed by investigating their predictive capabilities. In more detail, the objectives of this work are to:

- Compile and synthesize a dataset of instrumented liquefiable sites to provide a framework to validate effective stress models;
- Perform and compare total stress equivalent-linear, total stress nonlinear and effective stress nonlinear analyses for ground motion recordings presenting a wide range of strain levels;
- Compare the predictions of five existing 1D simplified effective stress constitutive models and propose a calibration scheme to account for the difficulties in selecting the input parameters of these models;
- Quantify the accuracy and variability of the predicted motion at the surface in terms of response spectra, amplification spectra, pore pressure responses and other commonly used ground motion parameters (i.e. Arias intensity, significant durations, cumulative absolute velocity, etc.).

For this purpose, equivalent-linear (EQL), total stress nonlinear (NL-TS) and effective stress nonlinear (NL-ES) ground response analyses are performed using the site response code Deepsoil (version 6.1.1) developed by [18]. Deepsoil is a well-validated code [6, 10, 11, 19] that includes some of the most advanced models in nonlinear site response analysis, such as the General Quadratic/Hyperbolic model (GQ/H) [20] with strength control and frequency-independent damping formulation, and integrates several models for effective stress analysis. [19] conducted an extensive validation study with various software and found that the results of total stress ground response analyses were highly influenced by the numerical platform. Thus, it was decided to use a single software in order to avoid inducing additional bias in the analyses, despite limiting the number of available effective stress models.

Amongst the existing effective stress constitutive models, five models were used in this study: [21], Green-Mitchell-Polito (GMP) [22], [23], Generalized [24] and [25]. In an attempt to address the limitations of the effective stress models and the limited guidance in the selection of their input parameters, a methodology was developed to calibrate the model based on the available soil properties at each site, recommendations by the effective stress model's authors or general correlation relationships found in the literature. The goal of this approach was to reproduce the procedure that could be used by an engineer in practice, who would have limited information regarding a site's dynamic soil properties.

The effective approach is validated against seven liquefaction case studies, composed of five downhole seismic arrays and two centrifuge experiments. Downhole seismic arrays are composed of at least two seismometers located at the surface and at different depths in a borehole. Thus, in ground response analysis, the downhole recording can be used directly as an input motion and the resulting surface motion can be compared with the surface recordings for validation purposes. In this study, data from the Kiban-Kyoshin network (Kik-net) and the well-documented case studies of Wildlife Liquefaction, Lotung, and Port Island arrays, were used. In addition, data from two centrifuge experiments were used. From all the sites, a total of 98 earthquake recordings were selected with the aim of representing varying levels of ground motion amplitude and pore pressure buildup. Amongst those, 11 motions were identified as having induced liquefaction based on the recordings from pore pressure transducers, and 18 were defined as associated with a high probability of liquefaction based on a simplified liquefaction analysis [26, 27].

1.3 Organization of thesis

This thesis is divided into seven chapters, including this introductory chapter. Chapter 2 provides a review of the literature on the main effective stress model, including their limitations, and gives an overview of the integration of the effective stress approach in 1D ground response analysis. Chapter 3 describes the selected sites and earthquake motions used in this study and their main properties. Chapter 4 details the modeling approach for the total stress equivalent-linear, nonlinear models and the methodology adopted to calibrate the effective stress models based on the available information at each site. In Chapter 5, the results are analyzed by comparing the observed and predicted spectral acceleration and amplification spectra using mixed-effect regression analysis and Pearson's correlation coefficients. The pore pressure response of each model in each simulation is then evaluated as a function of time and shear strain, and compared with general correlations representing the expected behavior of liquefiable soils. Finally, the performance of each model is evaluated against the predictions of

common ground motion parameters, including the Arias intensity (AI), significant duration (D_{5-95} & D_{25-75}), cumulative absolute velocity (CAV & CAV_{STD}), number of equivalent loading cycles (N_{eq}), shaking intensity rate (SIR) and characteristic periods (T_m, T_o and T_p). Chapter 6 presents a discussion of the limitations of the present study. Finally, Chapter 7 summarizes the main findings of this work and recommendations for future research in this area are provided.

CHAPTER 2 EFFECTIVE STRESS ANALYSIS

Effective stress ground response analyses are performed by modeling the generation, dissipation and redistribution of excess pore water pressure during cyclic loading and its effect on the mechanical behavior of a soil. One-dimensional effective stress ground response analyses are usually performed by coupling a pore pressure generation model with degradation index functions that modify the modulus reduction curves [25]. The following section reviews, for both granular and cohesive soils, the pore pressure mechanisms, the implementation of the effective stress approach in the Deepsoil software [18], and some of the existing pore pressure generation models along with their limitations.

2.1 Excess pore water pressure generation and liquefaction

Pore water pressure generation during cyclic loading is induced by the tendency of soils to change volume under the propagation of stress waves, because of the rearrangement of the soil particles. Rapid loading results in undrained conditions, under which loose saturated sands exhibit a contractive tendency which results in normal stresses being transferred from the soil matrix to the pore water, thus generating positive excess pore pressure and a decrease in effective stress. Consequently, the soil's stiffness and strength, which depend on the effective confining stress, decrease. A state of liquefaction is reached when the pore pressure buildup approaches the initial effective stress so that the pore pressure ratio r_u as defined below, approaches 1:

$$r_u = \frac{\Delta u}{\sigma'_{vc}} \tag{2.1}$$

where Δu is the excess pore water pressure and σ'_{vc} is the effective consolidation stress. In practice, liquefaction is defined at lower pore pressure ratios (e.g. when r_u reaches 95%) or when the level of cyclic shear strain exceeds 3% [16, 28]. In fact, for non-plastic fine soils, such as sandy silts, the maximum possible r_u might be 90-95% rather than 100%, while large strains or softening associated with liquefaction might still be observed [28].

The cyclic behavior of cohesive soils differs from sands and is generally associated with lower pore water pressure generation. In fact, in clays, degradation is not only a result of excess pore pressure buildup but also of the deterioration of the clay microstructure due to the breakage of particle bonds [29]. In this material, the significant strength loss and

deformation associated with pore pressure buildup is referred to as "cyclic softening" rather than liquefaction [16].

2.2 Cyclic degradation due to excess pore water pressure generation

The degradation of the soil's stiffness and strength as a result of excess pore water pressure generation is accounted for by the modulus (δ_G) and shear stress (δ_τ) degradation functions developed by [30] for sands and [29] for clays, as presented in Table 2.1.

Table 2.1 Modulus and shear stress degradation index functions

Materials	δ_G	δ_τ
Sands	$(1-u_N^*)^{1/2}$	$(1-u_N^*)^v$
Clays	N^{-t}	

where $u_N^* = u_N/\sigma_v^{'}$ is the normalized residual cyclic pore pressure after N cycles. Since r_u and u_N^* are essentially equivalent, r_u is used throughout this document to refer to u_N^* and simplify the notation. v and t are degradation parameters, where t is taken as 1 in Deepsoil, γ_c is the amplitude of the shear strain, and γ_{tvp} is the volumetric threshold shear strain below which the soil microstructure remains unchanged and no volume or pore water pressure changes are generated ($\approx$ 0.01 and 0.02% for most sands and 0.1% for clays). [31–33] The degradation index functions are incorporated into the formulations of the Modified Kondner-Zelasko (MKZ) model in [25] and the Generalized Quadratic/Hyperbolic (GQ/H) model presented in Equation 2.2 and fully described in [20].

$$\delta_G \cdot \theta_\tau \left(\frac{\tau}{\delta_\tau \cdot \tau_{max}}\right)^2 - \left[1 + \left(\frac{\delta_G}{\delta_\tau} \cdot \frac{\gamma}{\gamma_r}\right)\right]\left(\frac{\tau}{\delta_\tau \cdot \tau_{max}}\right) + \left(\frac{\delta_G}{\delta_\tau} \cdot \frac{\gamma}{\gamma_r}\right) = 0 \tag{2.2}$$

where τ is the shear stress, γ the shear strain, θ_τ is a model-fitting function, and τ_{max} is the large-strain maximum shear stress (i.e. the shear strength).

2.3 Dissipation and redistribution

The dissipation and redistribution of pore water pressures are evaluated based on Terzaghi's 1D theory of consolidation:

$$\frac{\delta_u}{\delta_t} = c_v \frac{\delta_u^2}{\delta_z^2} \tag{2.3}$$

where c_v is the coefficient of consolidation.

Deepsoil uses a finite difference method to compute the dissipation and redistribution that occur simultaneously with the generation of excess pore water pressures. Note that dissipation happens in the vertical direction only and that the bottom boundary condition can be specified as permeable or impermeable.

2.4 Pore pressure generation models

Pore pressure generation models have been developed based on field measurements and laboratory tests, and can be categorized into stress-based, strain-based and energy-based models. This section presents a review of a few models for both granular and cohesive soils, with a focus on the models used in the present study.

2.4.1 Granular soils

Stress-based models

[34], [35] and [36] first developed empirical models to estimate pore pressure generation based on cyclic stress-controlled testing. The excess pore pressure ratio (r_u) was expressed as a function of the cyclic ratio (N/N_L), where N is the number of equivalent loading cycles and N_L is the number of loading cycles required for the initiation of liquefaction. Although the mathematical form is simple, it is not applicable to non-liquefiable soils and N_L can be difficult to define [37]. In addition, this requires that the input motion be converted into an equivalent number of uniform cycles for a given cyclic stress ratio (CSR). Since these parameters need to be defined prior to the analysis, this method cannot consider the soil's dynamic response and pore pressure buildup. Thus, these models cannot be coupled with a time-domain site response analysis. [23] offer a more comprehensive approach which only requires a $CSR - N$ curve obtained from stress-controlled testing. The model is based on the concept of a damage parameter, as expressed in Equation 2.4

$$r_u = \frac{2}{\pi} \arcsin \left(\frac{D}{D_{r_u=1.0}} \right)^{\left(\frac{1}{2\beta}\right)} \quad \text{where } D_{ru=1.0} = 4N(CSR - CSR_t)^{\alpha} \tag{2.4}$$

where D is the damage parameter, CSR_t is the threshold shear stress ratio below which no pore pressure is generated, and α is a curve fitting parameter.

Recently, [38] proposed a reformulation of the [23] model based on a similar concept of a damage parameter and verified its application for different types of soils. Considering their similarities and the implementation of the [23] model in Deepsoil, the latter was selected for

this study.

Strain-based models

There have been several studies in the literature reporting that pore pressure generation is controlled by cyclic shear strains rather than cyclic shear stresses [33, 39–42]. These studies revealed that below a unique value of shear strain, defined as the volumetric threshold shear strain (γ_{tvp}), no excess pore pressure is generated. From the results reported in these studies, different approaches were proposed. The first models described the relationship between the volumetric strain and excess pore water pressure [43–47] The second method focused on the relationship between cyclic strain and pore pressure. Based on the model of [43] and the concept of γ_{tvp}, [48] developed an empirical model derived from undrained laboratory testing. [49] reformulated this model and introduced the effect of multi-directional shaking, as defined by the following equation:

$$r_u = \frac{p \cdot f \cdot N(\gamma_c - \gamma_{tvp})^s}{1 + f \cdot F \cdot N(\gamma_c - \gamma_{tvp})} \tag{2.5}$$

where p, F, s are curve fitting parameters, f represents the number of dimensions, N is the number of cycles, and γ_c is the cyclic shear strain amplitude. Based on this formulation, no pore pressure is generated when $\gamma_c < \gamma_{tvp}$.

Finally, prior to the [23] model, [50] and [51] have also proposed models based on a similar concept of a damage parameter to represent the pore pressure buildup as a function of accumulated shear strains.

Energy-based models

Energy-based models define the excess pore pressure ratio (r_u) as a function of dissipated energy (W_s) which can be computed from the area bounded by the stress-strain cycles as displayed in the following equation:

$$W_s = \frac{1}{2\sigma_{co}^{'}} \sum_{i=1}^{n} (\tau_{i+1} + \tau_i) \cdot (\gamma_{i+1} - \gamma_i) \tag{2.6}$$

where $\sigma_{co}^{'}$ is the initial confining effective stress.

[24] originally developed a model presented in Equation 2.7, where α and β are fitting parameters.

$$r_u = \alpha \cdot W_s^{\beta} \tag{2.7}$$

The Green-Mitchell-Polito (GMP) model [22] introduced a parameter PEC, the "Pseudo-Energy Capacity", and defined the general form of their model as follows:

$$r_u = \alpha \sqrt{\frac{W_s}{PEC}} \tag{2.8}$$

2.4.2 Cohesive soils

Pore pressure generation models for cohesive soils have received less attention since they are associated with lower pore pressure generation and damages than granular soils. Degradation in clay is the result of simultaneous pore pressure generation and microstructure deterioration. Therefore, following the degradation functions presented in Section 2.2., the pore water pressure is estimated after the computation of degradation. Note that this approach is opposed to the one for sands, where degradation depends on the previous estimation of pore pressure. The pore pressure buildup is also characterized by a higher volumetric threshold shear strain due to flexible electrical links between the particles [29]. Moreover, for overconsolidated (OC) clays, negative pore water pressures may occur at the beginning of cyclic loading [29]. [29] proposed the following strain-controlled model which considers the dilatation behavior of OC clays:

$$r_u = AN^{-3t} + BN^{-2t} + CN^{-t} + D \tag{2.9}$$

where N is the number of cycles, $t = s(\gamma_c - \gamma_{tvp})^r$, and A, B, C, D, r, and s are fitting parameters.

2.4.3 Limitations

The following section reviews the limitations regarding the predictive capabilities of the pore pressure generation models, along with the main issues related to their use in effective stress ground response analysis.

In general, the proposed models rely on curve fitting procedures based on laboratory test data, and the application and accuracy of such models in effective stress ground response analysis have not been well documented and validated. The main limitation involves the fact that previous work has been limited to the validation of the models against liquefaction case studies. Thus, the performance of the models against other conditions of pore pressure

buildup and non-liquefiable soils has not been investigated in depth.

Besides, the calibration of input parameters is a tedious task, and a source of error. For instance, the models involve a large number of parameters, and their selection can be challenging since limited guidance exists in the literature. While correlations have been developed for some of the parameters, which will be discussed in more detail in Section 4.2, other models involve scaling parameters to match laboratory test data. When such data is unavailable, their determination can be difficult and relies on the judgment of the user.

Furthermore, pore pressure generation and liquefaction triggering involve complex mechanisms that depend on internal factors (i.e. soil properties), such as relative density, aging, cementation, saturation, fines content [16], and external factors such as the confining pressure, the amplitude of cyclic shear strains, initial static stresses, multidirectional loading, number of loading cycles, upward seepage (void redistribution), stratified soil effects and alternation of ground motion [17]. To account for these factors, some studies have developed relationships for the determination of the models' parameters. For example, [52], [53], [54], and [54] proposed correlations to consider the effect of the relative density, fines content, granulometry, and OCR. However, the other listed parameters are not directly included and may influence the pore pressure response. Therefore, the applicability of such methods in practice on soils with a wide range of properties and in-situ conditions not associated with the tested soils used in the empirical models requires further investigation.

Moreover, all the models for cohesionless soils poorly capture the dilative behavior that can occur during cyclic loading. For sands, depending on the relative density and confining stresses, both loose and dense sands may exhibit a dilative tendency at some shear strain levels [28]. This dilative tendency results in a strain-hardening response and an increase in the soil's stiffness. Therefore, a significant proportion of the ground motion can be propagated and sometimes result in high amplitude high frequency acceleration pulses [55] that would not be captured with a model neglecting dilation.

2.5 Past validation studies

This section presents a review of previous validation studies of effective stress models in 1D ground response analysis and their main results.

[55] performed total stress equivalent linear and effective stress nonlinear analyses using centrifuge data from [56]. They used the pore pressure generation models of [49] and [22] in the Deepsoil software. The results showed that while liquefaction triggering was accurately captured, it was concluded that the studied models generally failed to reproduce acceleration

pulses linked to dilatancy in liquefiable soils. In addition, a "base isolator" effect associated with the liquefiable layer led to the deamplification of surface motions. In fact, EQL linear were found to more accurately capture the observed motion than effective stress analyses.

In [57], Deepsoil was used to simulate the response from six ground motion events during the 2010-2011 Canterbury Earthquake using 1D nonlinear effective stress ground response analysis. The effective stress constitutive model studied was the [49] model. In general, excess pore pressure buildup was reasonably captured and showed good agreement to CPT results. Total stress and effective stress nonlinear results were shown to be similar in terms of shear strain, maximum pore pressure ratio, maximum PGA profiles with depth and response spectras.

[58] validated the predictions of the [49] model using the GQ/H model in the Deepsoil software against undrained cyclic direct shear tests and centrifuge experiments including [56], [59] and [60]. The results showed the ability of this model in capturing stress-strain and porewater pressure response. The main limitation was found to be associated with the inability of the model in capturing dilatant tendencies for $r_u > 0.8$ and when the maximum computed shear strain (γ_{max}) exceeded the limit shear strain (γ_{limit}). γ_{limit} is defined as the shear strain related to the identification of dilatancy in laboratory tests. For these conditions, the comparison of observed and predicted response spectras showed the occurrence of a potential bias at both low and high frequencies.

[61] proposed a procedure for liquefaction triggering based on nonlinear effective stress site response analysis. The procedure was validated using 14 ground motions events from three centrifuge tests [56, 59, 60] and case histories, including the Wildlife Liquefaction Array, Port Island Array and Treasure Island. The [29] and [49] pore pressure generation models were used to represent clay and sand behavior, respectively. The results demonstrated that the pore pressures were predicted accurately and were found to be consistent with the CRR curves obtained from field observations.

CHAPTER 3 SITE SELECTION

The main objective was to select sites where at least one ground motion generated high pore water pressure or triggered liquefaction. For this purpose, five seismic downhole arrays (KiK-net KSRH07 & TCGH16, Wildlife Liquefaction Array (WLA), Lotung Array (LSST), and Port-Island Array (PIDA)) and two centrifuge experiments (from [56] (CSP3) and [1] (CFF2)) were selected. The shear-wave velocity profiles (V_S) and average shear wave velocity in the upper 30 meters (V_{S30}) of all the sites are presented in Fig. 3.1. Note that the velocity profiles for the centrifuge sites were determined based on the [62] correlation (see Section 4.1.5 for more details). Also, since the height of the model is lower than 30 m for these sites, V_{S30} was taken as the average velocity in the soil profile for the modeled depth. Based on the shear wave velocity profiles, most sites are characterized as seismic site class D (NEHRP 1993).

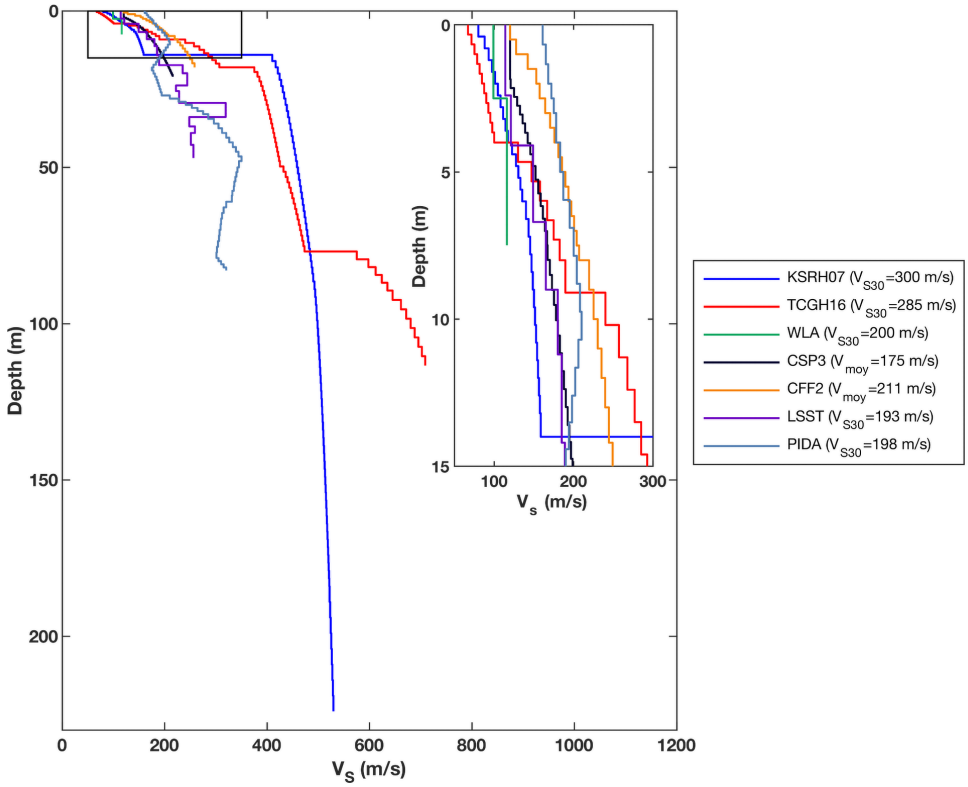


Figure 3.1 Shear wave velocity profiles of the 7 selected sites

Across the seven sites, 98 recordings were used with moment magnitudes (M_w) ranging from 3.4 to 9 and peak ground surface accelerations (PGA) from 0.004 to 1.67 g. The distribution of M_w and PGA distribution is displayed in Fig.3.2a and Fig.3.2b as a function of PGA and

V_{S30}, respectively. A detailed list of the input motions is provided in Table S1 in Appendix A.

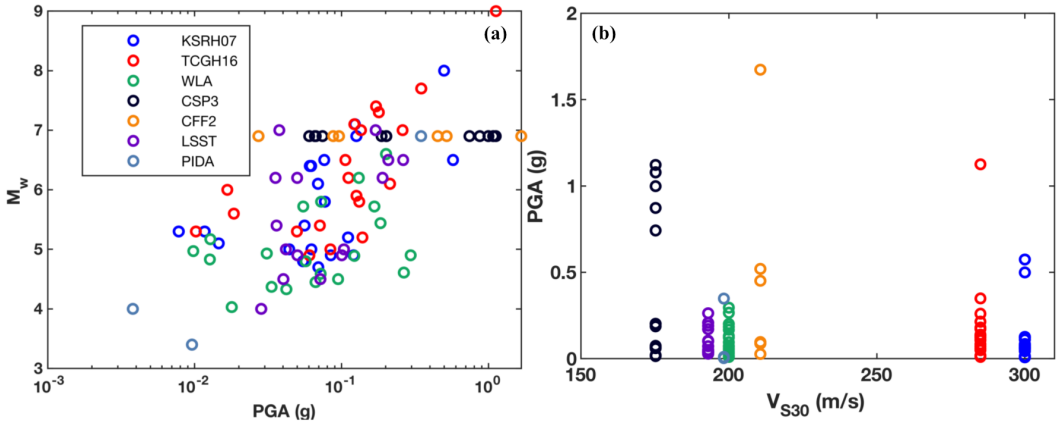


Figure 3.2 Distribution of the magnitude and surface PGA versus the observed surface PGA and V_{S30} (respectively) for the 98 ground motions

From the seven sites, WLA, CSP3, CFF2, and LSST were instrumented with pore pressure transducers and clear evidence of liquefaction was observed at the PIDA site. From this data, 11 of the 98 selected motions were considered to have triggered liquefaction based on the pore pressure records. Since site KSRH07 and TCGH16 did not have any pore pressure recordings, time-frequency analysis and simplified liquefaction evaluation procedures were used to assess if liquefaction was triggered, as explained in the next section. Note that these analyses were performed for the other sites as well to verify the application of the procedures. The results of these procedures for each ground motion are included in Table S1, along with the measured pore pressure ratios. Finally, a description of the selected site profiles, available soil properties, instrumentation and ground motion recordings is provided.

3.1 Time-frequency analysis

[63] performed time-frequency analysis on surface records from liquefaction case studies using Stockwell transforms, or S-Transforms [64], and reported that an abrupt change in the frequency content suggests the triggering of liquefaction. Thus, time-frequency analysis was applied to the observed surface motions. The computed spectral amplitudes were smoothed and normalized by the peak amplitude of each time step based on the procedure described in [63,65,66]. Note that Stockwell transforms were used since they provide the best time and frequency resolution over other methods, such as Short-Time Fourier or Wavelet Transforms.

The time-frequency analysis was applied to each site where no pore pressure measurements were available. The results revealed that site KSRH07 did not exhibit any change in the frequency content over time. In opposition, motion #EQ1 for site TCGH16, representing the 2011 Tohoku earthquake ($M_w = 9$ and $PGA = 1.13\ g$), was found to be associated with a clear change in the frequency content. The normalized Stockwell transform for the North-South component ($PGA_{NS} = 0.81\ g$) of said earthquake is provided in Fig. 3.3.

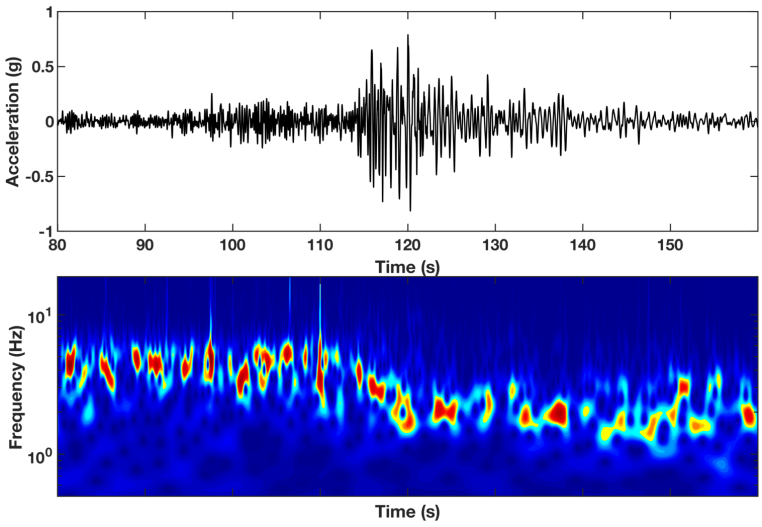


Figure 3.3 Normalized Stockwell Transform of the 2011 Tohoku Earthquake (NS component) at site TCGH16

The results show that a change in the frequency content over time was observed at approximately 110 seconds. Thus, liquefaction was assumed to have occurred during this earthquake event. For the other sites, the application of the time-frequency analysis was found to be overall consistent with the pore pressure measurements or observations. Further detail is provided in the respective descriptions of the sites in Section 3.3.

3.2 Simplified liquefaction analysis

For all the input motions selected in this study, a simplified liquefaction analysis was applied to evaluate the probability of liquefaction for every motion (P_L). For sites KSRH07, TCGH16, CSP3 and CFF2, the V_S-based procedure of [26] was used. At site WLA, CPT test measurements were available and the procedure of [27] was used. Finally, sites LSST and PIDA both had SPT test data and [27] was used. The estimated values of P_L as a function of $PGA_{obs-surf}$ are presented in Fig. 3.4 and are grouped by site. From the 98 records, it

was estimated that 18 motions yielded a probability of liquefaction of almost one and 5 other motions had P_L that were higher than 60%.

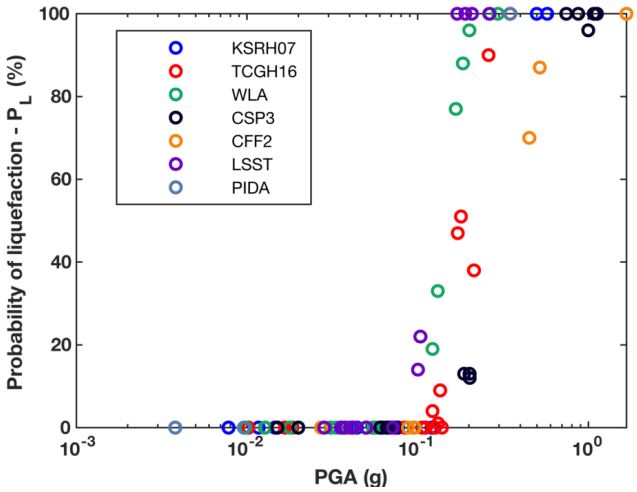


Figure 3.4 Probability of liquefaction versus the observed PGA at the ground surface

3.3 Description of the case studies

Downhole seismic arrays

The Kiban-Kyoshin (KiK-net) strong motion network of vertical high sensitivity seismographs (Hi-net) arrays located in Japan is a source used by many researchers for ground response validation studies [7]. In a prior study by [67], a classification scheme was developed for 100 arrays from the KiK-net database to identify the sites where the 1D wave propagation assumption, referred to as the SH1D model, was the most accurate and that were the most appropriate to validate ground response analysis. Amongst those sites, two sites were identified as being susceptible to liquefaction and with both strong and weak motions recordings available: 1-KSRH07 and 2-TCGH16. From the [67] classification, site KSRH07 was defined as an LG site, which has low inter-event variability in terms of amplification and a good fit to SH1D. Site TCGH16 was classified as LP, meaning that it has a low inter-event variability and is deemed appropriate for nonlinear modeling, but it has a poor fit to SH1D. While the class LG is the ideal category for calibration and validation of 1D site response analysis, the category LP can still be used with caution.

3.3.1 KSRH07

The first site KSRH07 (KiK-net11B) is located in the Tsurui village on the Hokkaido island in the northern part of Japan at latitude 43.136°N, longitude 144.327°E and an altitude of

38 m. The depth of the borehole and location of the downhole seismometer is 224 m. Station KSRH07 is composed of interbedded layers of sand, sandy gravel, pumice and volcanic ash sand over rock layers of sandstone and conglomerate. The average shear wave velocity in the upper 30 meters (V_{S30}) is 300 m/s. The water table is assumed at a depth of 6 m (see Section 4.1.5) based on the compression wave velocity evaluation. A total of 20 earthquake motions were selected from this array with surface PGA varying from 0.008 to 0.57 g. From those, the time frequency analysis did not reveal any abrupt change in the frequency content of the motion. The simplified liquefaction evaluation revealed that two of the input motions yielded a probability of liquefaction of almost one. The geological and velocity profiles, geological age and location of water table of station KSRH07 are represented in Fig. 3.5.

3.3.2 TCGH16

The site TCGH16 (KiK-net11A), displayed in Fig. 3.6, is located in the town of Haga in the Tochigi prefecture. It is located at latitude 36.548°N, longitude 140.075°E and at an altitude of 105 m. The total depth of the borehole is 112 m. Station TCGH16 consists of interbedded layers of sand, clay, gravel and sandy gravel over sandstone and mudstone. The V_{S30} is 285 m/s and the water table is assumed at a depth of 4 m (see Section 4.1.5). Twenty input motions were selected with PGA_{surf} from 0.01 to 1.13 g. The highest PGA_{surf} recorded was during the $M_w = 9$ 2011 Tohoku earthquake. Through time-frequency analysis, this motion was found to show a significant change in its frequency content, as shown in Fig.3.3. In addition, three other motions have a probability of liquefaction of almost one.

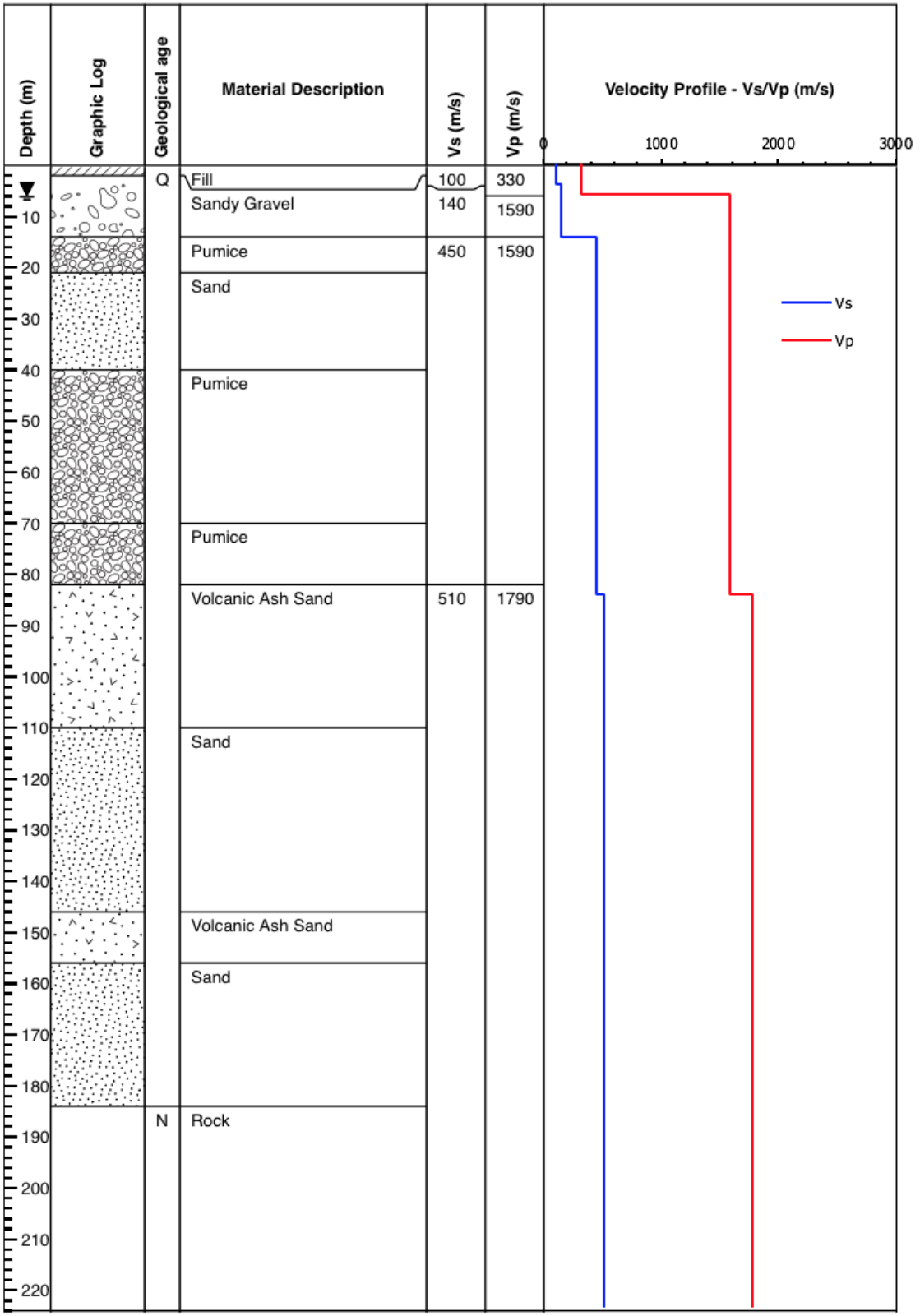


Figure 3.5 Station KSRH07 - Geological and velocity profiles description (Adapted from National Research Institute for Earth Science and Disaster Prevention (NIED))

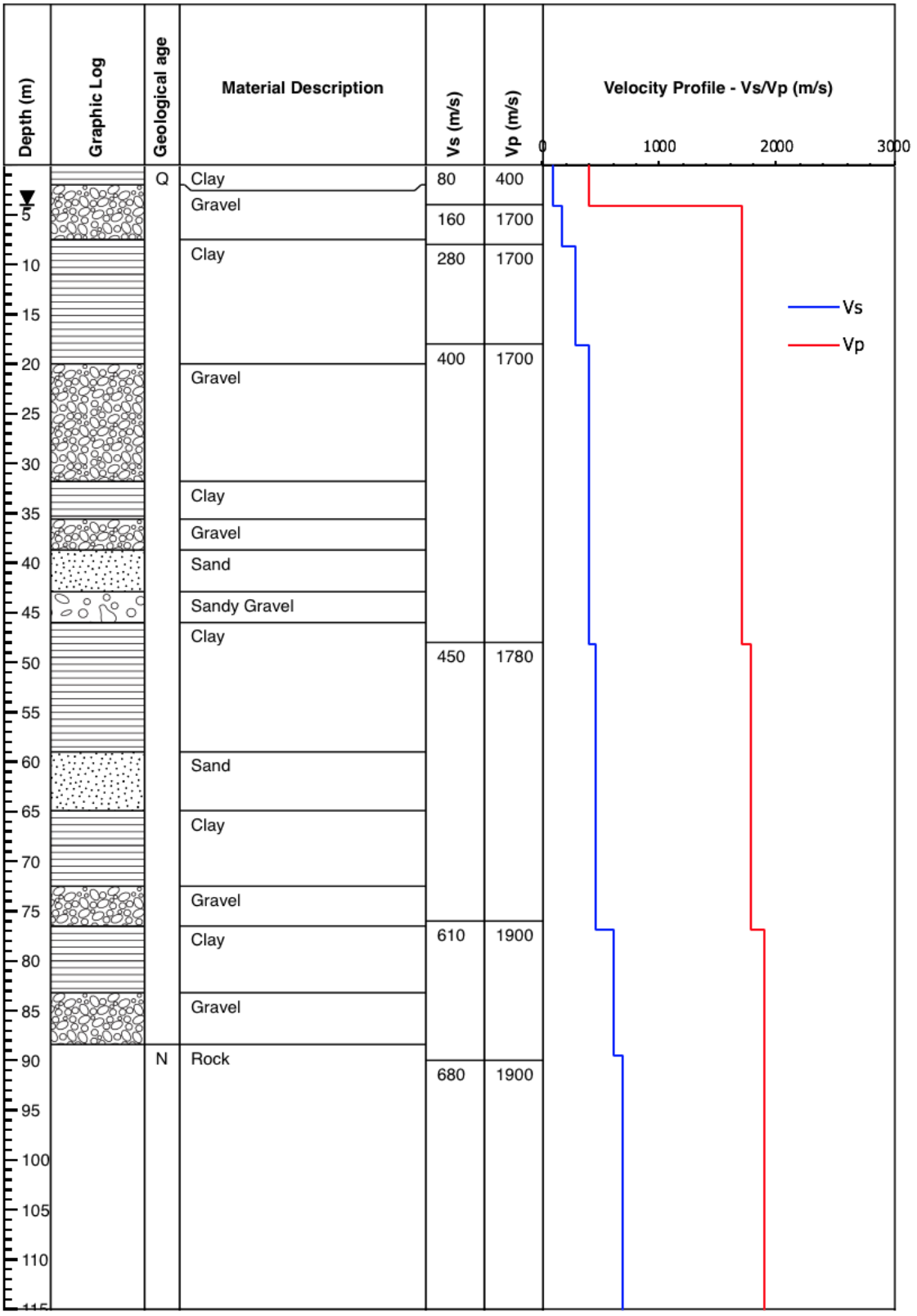


Figure 3.6 Station TCGH16 - Geological and velocity profiles description (Adapted from National Research Institute for Earth Science and Disaster Prevention (NIED))

3.3.3 Wildlife Liquefaction Array

he Wildlife Liquefaction Array (WLA) is located in California's Imperial Valley on the West bank of the Alamo River, 13 km north of Brawley, California at latitude 33.098°N, longitude 115.531°E. It is located in a highly seismic area close to the San Andreas Fault system. The site is composed of a 4.3 m thick liquefiable layer of silty sand bounded by a silt and a clay to silt layer on top and bottom. The total depth of the borehole is 7.5 m, the water table is located at a depth of 1.2 m, and V_{S30} was evaluated as 200 m/s. The available site properties, including the geological profile description, ground water level, fines content, liquid limit, plasticity index, coefficient of uniformity, velocity profile and CPT tip resistance (mean of data from tests Cg#1@3 in [68]), are presented in Fig. 3.7. The site was strategically

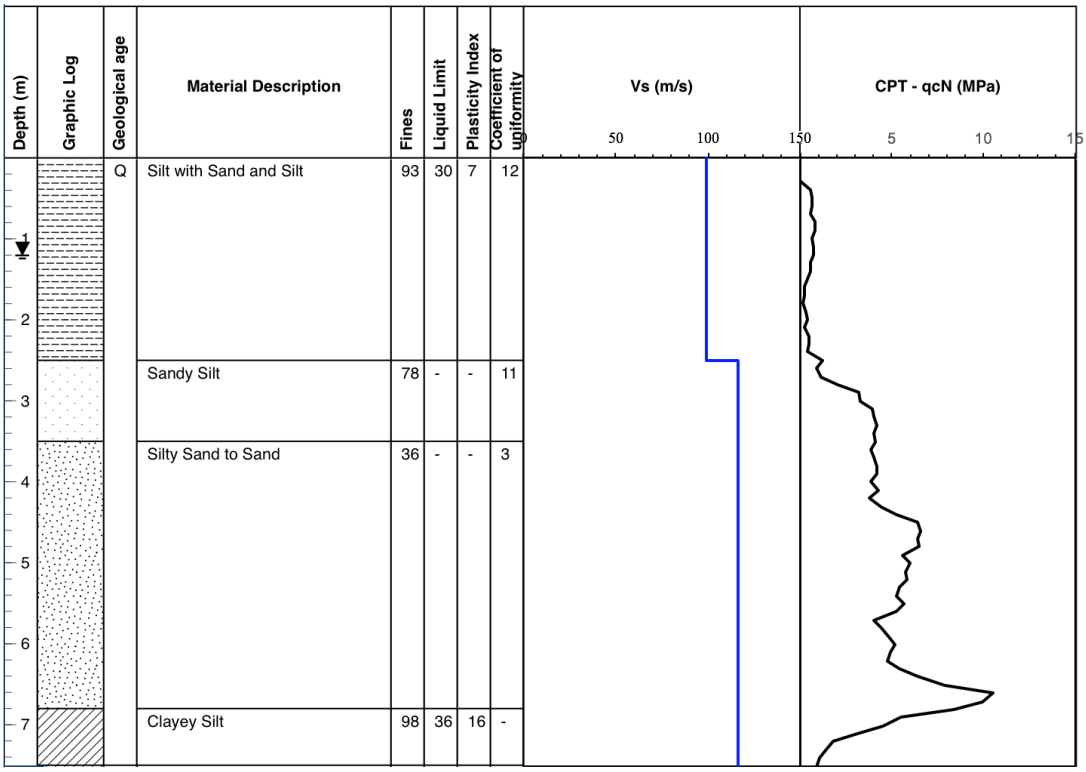


Figure 3.7 Wildlife Liquefaction Array (WLA) profile description (Adapted from [68] and [69])

chosen as a liquefaction research and ground motion monitoring center in an area where multiple evidences of liquefaction were observed. The USGS first instrumented the site in 1982 and equipped it with surface and downhole force-balance accelerometers (FBA) and six piezometers. In 2004, the site was re-instrumented 65 m away from the original site as part of the NEES program (UCSB, 2007). The new instrumentation consists of 6 downhole accelerometers, 3 surface accelerometers and 8 piezometers. Thus, two models were used

in the ground response analyses to represent each instrumentation. Fig. 3.8 displays the instrumentation of the profile with the details regarding the location of the accelerometers and the pore pressure transducers.

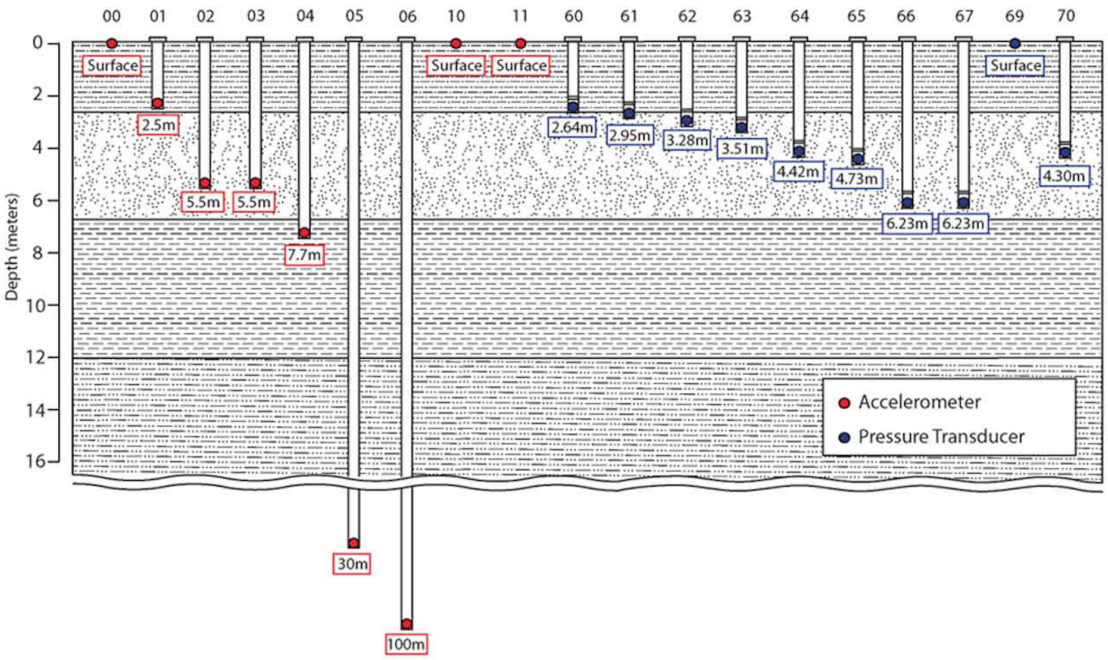


Figure 3.8 Wildlife Liqufaction Array - Instrumentation (from [70])

The WLA site is a key site for this study since it is one of the most well-documented case study of liquefaction. Multiple geotechnical investigations have characterized the geotechnical properties of the soil and the effect of liquefaction on the soil behavior [68, 70, 71]. Amongst the testing program, multiple CPT and SPT tests were conducted and an OYO suspension logger [69] was used to determine the velocity profiles. The investigation also included the determination of Atterberg limits, mass density, permeability, consolidation tests, and granulometry. In November 1987, the station recorded two major earthquakes: the Elmore Ranch ($M_w = 6.2$ and $PGA_{surf} = 0.13\ g$), and the Superstition Hills event ($M_w = 6.6$ and $PGA_{surf} = 0.20\ g$). A pore pressure ratio of 100% was recorded by the piezometers for the Superstition Hills event. During this earthquake, sand boils [71, 72] and lateral displacements of approximately 300 mm [31] were observed. The records of these two events were obtained from the Center for Engineering Strong Motion Data (CESMD). Eighteen other input motions were selected for the second instrumentation from the NEES@UCSB public data portal [73] (http://www.nees.ucsb.edu/data-portal, last accessed on August 7th 2019) with M_w from 4.0 to 5.7 and PGA_{surf} from 0.01 to 0.30 g. In total, 3 motions have

recorded pore pressure ratios higher than 60% but only one triggered liquefaction. Finally, both the simplified liquefaction and time-frequency analyses revealed a possibility of high pore pressure generation for at least 4 events (see Table S1).

3.3.4 Lotung (LSST)

The Lotung site or Large-Scale Seismic Test (LSST) is located in Lotung, in the northeastern part of Taiwan at latitude 33.098°N and longitude 115.531°E. The soil profile is composed of alternating layers of silty sand, clayey silt, gravel and organic matter. The shear-wave velocity profile is obtained from [74] and V_{S30} is 193 m/s. The profile depth is 47 m and the water table is located at a depth of 1 m [75]. Multiple investigations have been conducted at this site and are summarized in [75] and [76]. From these references, the profile geology, V_P, and SPT test data were used. The detailed profile of LSST is presented in Fig. 3.9.

This array was originally built for soil-structure interaction (SSI) research by the Taiwan Power Company (TPC) and the Electrical Power Research Institute (EPRI). The instrumentation consists of a 1/4 scale model structure and two downhole arrays, named DHA and DHB. The arrays are located at a distance of 3 m and 49 m away from the structure, respectively. For this study, the data from the DHB station was used as the input motion. This station was considered as being representative of the free-field response since it was not affected by SSI effects [77]. Regarding the instrumentation of DHB, five triaxial accelerometers were located at depths of 0, 6, 11, 17 and 47 m. Note that the accelerometer FA1-5 was used for the surface motion. Moreover, a series of pore pressure transducers were installed from depths 3 to 16 m [78] in layers composed of silty sand identified as being susceptible to liquefaction.

In total, fifteen motions were selected in this study (LSST#4 to 18 from the original notation). To list, events 1, 4, 8, 9, 12, and 13 (or LSST#4, 7, 11, 12, 15 and 16 from the original notation) had PGA $>$ 0.1g and events 9 and 13 (LSST#12 and 16) recorded pore pressure ratios of 27% [78, 79]. For six of the input motions (EQ10-15, see Table S1), the records of the DHB-47 accelerometer were unavailable. Therefore, based on [77], the motions from station DHA-47 were used, located below the model structure, assuming that the records were located at a sufficient depth not to be affected by the presence of the model structure. In total, four ground motions were found to have a probability of liquefaction of almost 1 and presented an abrupt change in the frequency content using time-frequency analysis.

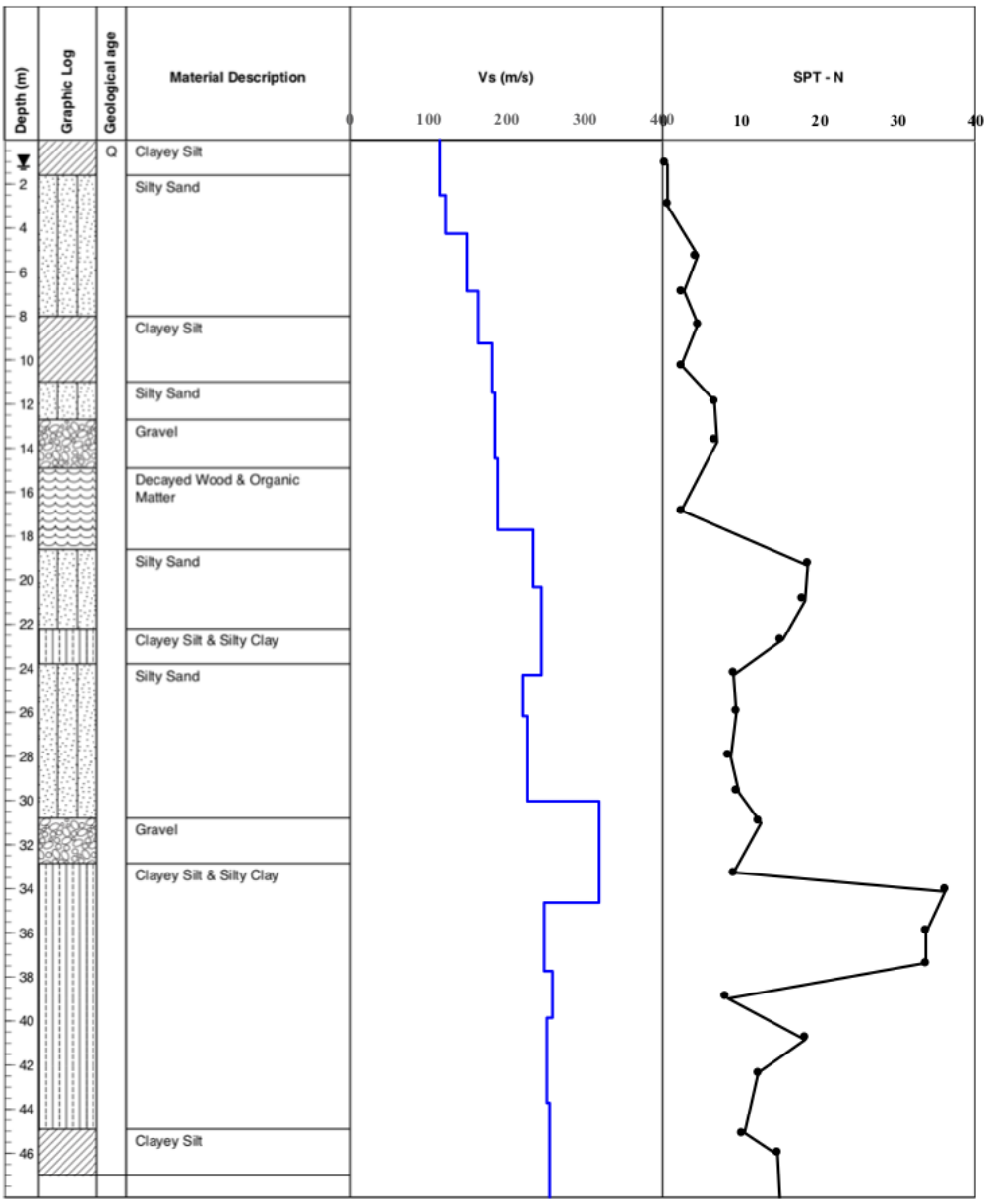


Figure 3.9 Lotung Array - Geological and velocity profile description (Adapted from [75] and [76])

3.3.5 Port-Island Downhole Array (PIDA)

The final downhole array site is the Port-Island Downhole Array (PIDA) located on a reclaimed island in Kobe Port, Japan, instrumented by the Development Bureau of Kobe City at latitude 34.670°N, longitude 135.208°E and altitude 4 m. This site consists of a 19 m thick surficial fill composed of sand, gravel and decomposed granite on top of layers of sand, gravel and alluvial or diluvial clay. The total depth of the profile is 83 m with four accelerometers

located at depths of 0, 16, 32 and 83 m. The velocity profile was obtained from suspension P-S velocity logging (V_S and V_P) from [80] and V_{S30} was evaluated as 198 m/s. The soil properties, such as the geological classification, water table, and SPT test data, were taken from [81] and are presented in Fig. 3.10. On January 17th, 1995, the Hyogo-ken Nanbu, or Kobe, Earthquake (M_w = 7.2 and PGA_{surf} = 0.35 g) occurred. Following this earthquake, evidences of liquefaction in the surficial fill, such as sand boils were observed [82]. Besides the main earthquake, a foreshock (M_w = 4 and PGA_{surf} = 0.004 g) and an aftershock (M_w = 3.4 and PGA_{surf} = 0.01 g) of this motion were included in this study. While the simplified liquefaction analysis and time-frequency analysis confirmed the triggering of liquefaction during the mainshock, no evidence of liquefaction was found for the other motions.

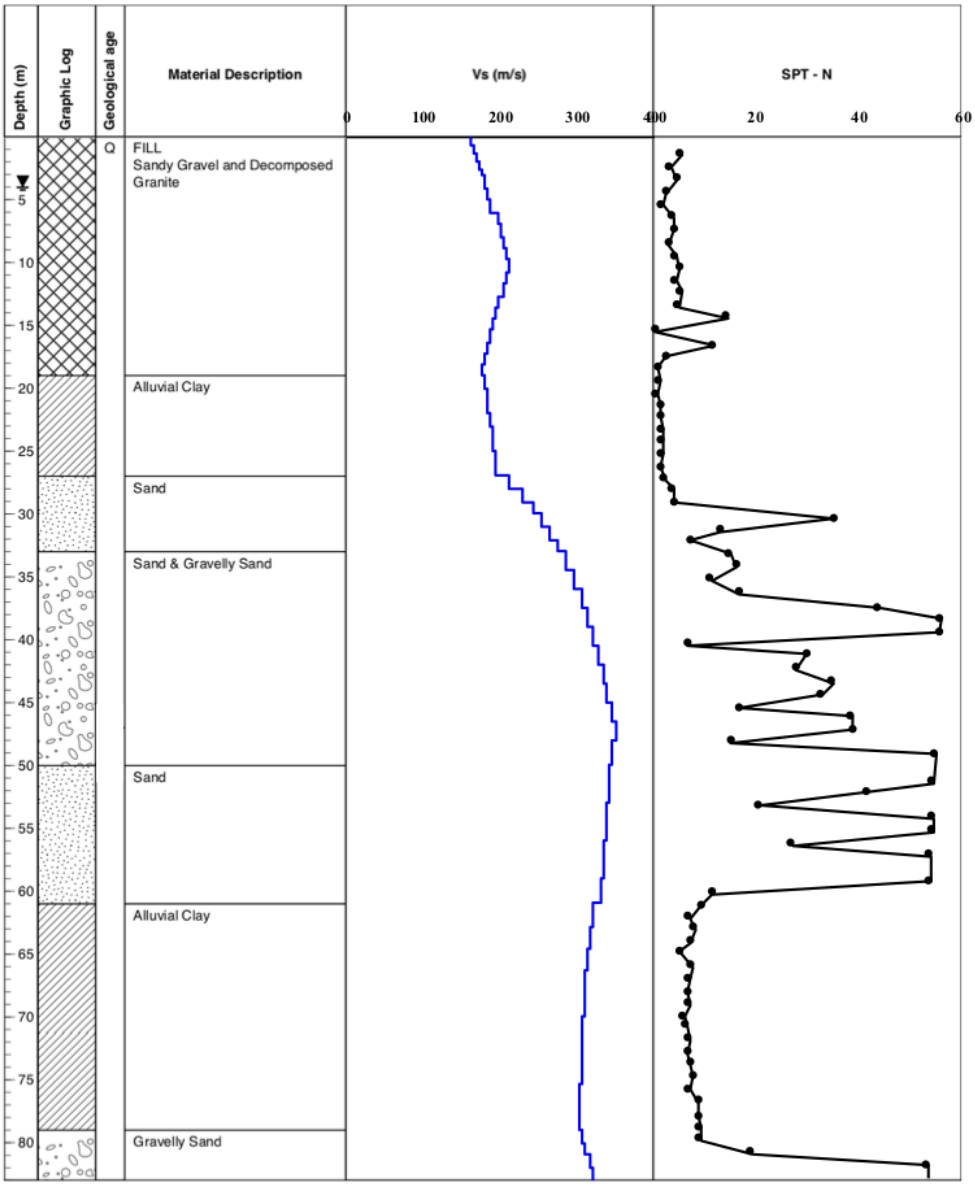


Figure 3.10 Port Island Downhole Array (PIDA) - Geological and velocity profile description (Adapted from [80] and [81])

Centrifuge experiments

In this study, free-field data from two centrifuge experiments which were considered as being representative of a 1D ground motion propagation problem and where liquefaction was observed, were selected. These centrifuge experiments are instrumented with multiple pore pressure transducers and accelerometers, allowing the extraction of the soil's dynamic behavior at various depths. The testing sequence involved the successive application of ground

motions of increasing intensities where sufficient time is allowed in between each event for the dissipation of the excess pore water pressure. The models are composed of layers of clean sands, and described in more detail in the following sections. Finally, for both tests, the time-frequency analyses and simplified liquefaction procedures were found to be consistent with the pore pressure measurements. Unless otherwise specified, all the data presented in this study are in prototype scale.

3.3.6 CSP3

The first centrifuge test is referred to as CSP3 and was presented in [56]. The data from seven accelerometers and four pore pressure transducers were used in this study. The soil model combines two horizontal saturated layers of uniformly graded Nevada sand with the water table located at the surface which is represented in Fig. 3.11. The two layers have thicknesses of 9.3 and 11.4 m (prototype scale) and relative densities D_R of 55% and 80% respectively. The soil properties (unit weight, granulometry, permeability, etc.) of each layer were provided in [56]. All tests were performed at a nominal centrifugal acceleration of 30 g and a series of 14 earthquakes from the testing sequence was selected. The input motions #5, 9, 12, 13, and 14 are based on the scaled versions of the 1995 Kobe earthquake recorded at the Port Island array. The other motions used the 1989 Loma Prieta earthquake recorded at University of California Santa Cruz. In total, five motions triggered the liquefaction of the top medium dense layer.

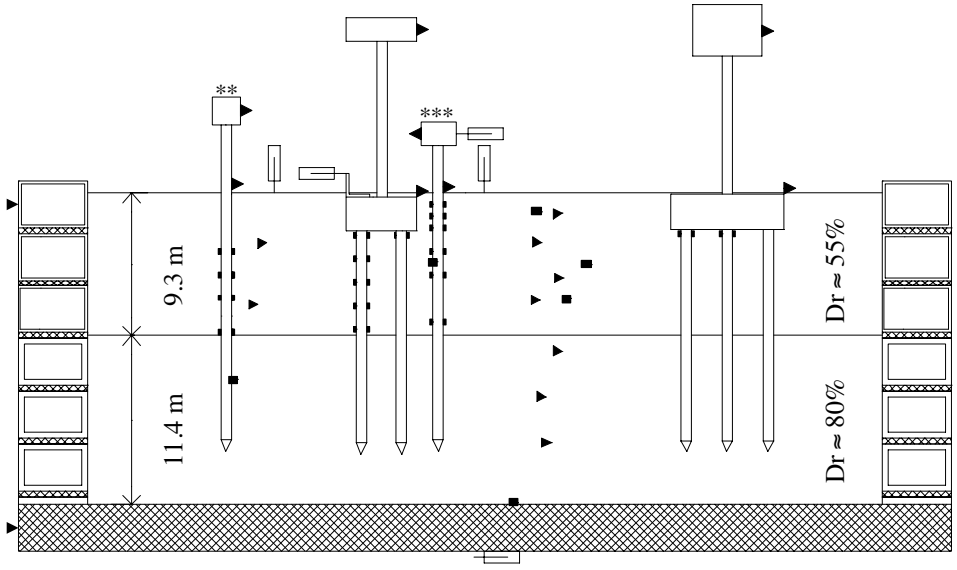


Figure 3.11 Centrifuge test CSP3 model layout (from [56])

3.3.7 CFF2

The second centrifuge test data will be referred to as "CFF2" in the following study. The data uses the free-field array of the centrifuge experiments presented in [1] and [83]. This center array was instrumented with 6 accelerometers, 5 pore pressure transducers and one vertical linear variable displacement transformer (LVDT). The model is composed of a 6 m thick (prototype scale) liquefiable layer of loose Ottawa sand F65, with a relative density D_R of 40%, bounded at the bottom by a 10 m thick layer of the same sand at $D_R = 40\%$ and at the top by a 2 m thick layer of Monterrey sand 0/30 at $D_R = 90\%$. The model layout and instrumentation are presented in Fig. 3.12. The water table is located at the surface of the model. The soil properties were taken from [83], and [84]. Moreover, the tests were conducted at a centrifugal acceleration of 70 g, and six input motions were used. To enumerate, input motions #1 and 3 are based on the scaled versions of low and high intensities of the 1992 Landers earthquake recorded at the Joshua tree station. Events #2 (low intensity), 5 (high), and 6 (high) are based on the 1995 Kobe earthquake at Takatori and event #4 represents the 1994 Northridge earthquake recorded at Newhall-WPC station. In total, five motions triggered liquefaction in the two bottom layers composed of Ottawa sand.

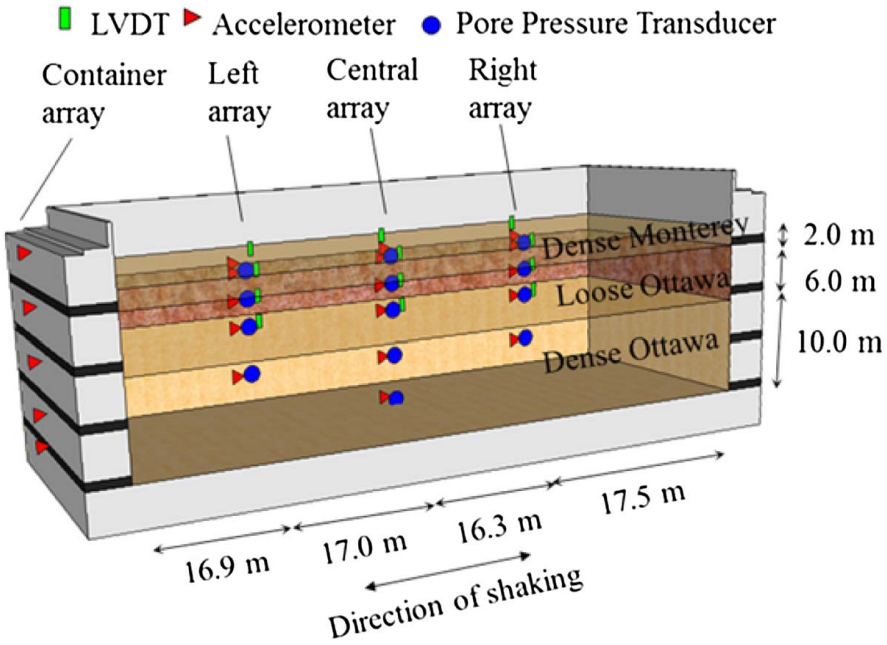


Figure 3.12 Centrifuge test CFF2 model layout (from [83])

CHAPTER 4 METHODS

The following describes the procedure used to perform each ground response analysis. For the effective stress analyses, a calibration scheme of the input parameters is introduced.

4.1 Site response analysis parameters

The selection of the input parameters and other control parameters required to calibrate each model for the total stress ground response analyses is presented in this section. Finally, additional details for the calibration of the KiK-net sites (KSRH07 & TCGH16) and centrifuge experiments (CSP3 & CFF2) are provided.

4.1.1 Layer thickness

The thickness of the layers (H) was selected based on the fundamental frequency of each element determined with the following equation.

$$f_{max} = \frac{V_S}{4H} \tag{4.1}$$

[18] recommends that the frequency of the shortest wave to be propagated should be of a minimum of 30 Hz. In this study, f_{max} was selected as 50 Hz to ensure that all significant frequency content would propagate in the ground response analyses.

4.1.2 Modulus reduction and damping curves

Modulus reduction and damping curves were computed using the [85] empirical model rather than the widely used [86] model. [7] performed ground response analysis on 6 KiK-net sites and compared the curves with commonly used [86] curves. They found that the [86] curves overdamp the response at strains higher than 0.01%. The input parameters for the [85] empirical relationships are the mean effective confining stress ($\overline{\sigma_m}$), the plasticity index PI and geological age. In this study, $\overline{\sigma_m}$ was computed either with $K_0 = 0.5$, or, for sites KSRH07 and TCGH16, where both shear and compressional wave velocities were available, K_0 was determined using Equation 4.2 presented below.

$$K_0 = \frac{v}{1-v} \text{ where } v = \frac{V_P^2 - 2V_S^2}{2V_P^2 - 2V_S^2} \tag{4.2}$$

[85] curves were developed for PI = 0, 15, 30, 50, 100 and 150. Since limited information was available on the plasticity of the soil layers in the profiles, average values for each soil type were chosen. Thus, following [87]'s classification chart, PI was taken as 0 for sands or gravels, 15 for silts and 30 for clays. For all the sites, including the centrifuge tests, the geological age was taken as the quaternary period. For the sites KSRH07 and TCGH16, the downhole accelerometers were located within a rock layer, and the modulus reduction and damping curves of [88] were used for these layers.

4.1.3 Nonlinear soil constitutive model

For the nonlinear (NL-TS and NL-ES) analyses, the selected soil constitutive model was the General Quadratic/Hyperbolic model (GQ/H) which includes strength control [20] along with the MRDF-UIUC unloading-reloading rules [89]. The implied shear strength for cohesionless soils was defined by the Mohr-Coulomb failure criteria considering a friction angle (ϕ) of 30° for sands and 35° for gravels (after [90]). For clays, the relationship of [91] was used.

$$\frac{S_u}{\sigma_0^{'}} = S \cdot OCR^m \tag{4.3}$$

where $S_u/\sigma_0^{'}$ is the undrained shear strength ratio, S is the shear strength ratio taken as 0.20 and $m = 0.8$ based on reported values in [92].

Small-strain damping formulation was selected as frequency independent, following the formulation of [89], in order to remove the limitation of Rayleigh damping as recommended by [18]. Note that the analyses were conducted with the damping matrix update option which updates the matrix at each time step to integrate the change in stiffness in the computation of the damping matrix.

4.1.4 Input earthquake motions and boundary condition

A rigid half-space was selected for all the sites following the recommendation of [6], [18], and [93], since the input motions retrieved from downhole arrays or centrifuge experiments are "within" motions. Ground motion processing included the application of zero-padding and a 5% cosine taper on the signal before filtering. An acausal bandpass Butterworth filter of order $n = 4$ was applied in the frequency domain to remove both the high (low-pass filter) and low (high-pass filter) frequency noise. The acausal formulation applies the filter in two passes in both directions in order to avoid phase distortion or shift of the signal [94]. In general, the low and high cut-off frequencies were set to 0.01 and 20 Hz, respectively. In some cases, for

example, when a motion had a Nyquist frequency ($f_N = \frac{1}{2}dt$) smaller than 20 Hz, the corner frequencies were modified based on the visual inspection of the Fourier acceleration spectrum. Finally, all motions were baseline corrected and subsampled to 50 Hz, to reduce the time of the analyses. For sites KSRH07, TCGH16, WLA, and LSST, the accelerometers recorded two orthogonal components of the motion (North-South – NS and East-West – EW), thus, separate ground response analyses were conducted for each individual component and the results were then combined in a single response spectrum using the geometric mean of the components.

4.1.5 Additional notes

KiK-net sites (KSRH07 & TCGH16)

For the KiK-net sites, the only data available was the stratigraphic soil/rock description, geological age, and velocity profiles. Therefore, additional hypotheses were drawn to define other parameters necessary for the analysis. The mass density ρ was determined using the procedure recommended by [95] based on V_S and V_P. For the location of the groundwater level, multiple studies [96–98] have found that a compression wave velocity V_P = 1500 - 1600 m/s is associated with a saturated soil. Thus, based on the available velocity profiles, the groundwater level was assumed to be located at the depth where $V_P > 1500$ m/s.

Moreover, preliminary ground response analyses on low amplitude motions revealed a bias for the estimation of the response spectra at high frequencies when compared to the observed surface motions. [14] conducted ground response analyses on 100 KiK-net sites which revealed a similar bias in the response at high frequencies. They hypothesized that a possible explanation is the oversimplification and coarseness of the velocity profiles, which sometimes exhibit large impedance contrasts, such as the one observed for site KSRH07 at a depth of 14 m, with V_S abruptly varying from 140 to 450 m/s. This can lead to strain localization and excess dissipation of high-frequency energy. They found that a modification of the velocity profiles with an exponential depth-dependent gradient provided a more realistic profile and reduced the bias. Thus, this modification was applied and revealed an improvement in the accuracy of the analyses of low amplitude motions in which propagation would be controlled by elastic properties.

Lotung Array (LSST)

[99], [74] and [100] developed modulus and damping curves based on the interpretation of laboratory data or acceleration time histories. However, because the curves were not hyperbolic, the fitting procedure of the GQ/H model in DEEPSOIL was imperfect, and their accurate implementation in the software was difficult. As a result, the comparison between

the computed and predicted surface motion showed an important bias for low-level ground motions. Thus, the curves of [85] were used, which was consistent with the procedure of the other sites. Note that the mass density was determined following the procedure described in Boore (2007) from the V_S and V_P measurements reported in [74] and [75].

Port-Island Downhole Array (PIDA)

The mass density ρ was determined using the procedure recommended by [95] based on V_S and V_P.

Centrifuge experiments (CSP3 & CFF2)

For the centrifuge tests, the experiments involve applying each ground motion sequentially to the same model. In centrifuge experiments, soils tend to densify due to induced stresses or liquefaction [101]. Thus, the changes in density in the liquefiable layers were computed based on the settlement's measurements obtained from vertical LVDTs and corresponding volumetric strains. Over the course of the testing sequence, a change of density of a maximum of 6% was calculated for test CSP3 in the upper layer. For test CFF2, the variation of density of the two layers that liquefied was evaluated as 6% for Monterey sand and 11% for the Ottawa sand by [83]. Thus, considering that the variation in density between each event was small, the mass density was considered constant.

Since no shear wave velocity profile was provided for these tests, the empirical correlation of [62] was used and with a set minimum of 120 m/s for shallow depths. In centrifuge experiments, the strain rate is higher than in normal seismic loading conditions due to centrifuge time scaling [102]. Since the shear modulus, related to V_S by $G = \rho \cdot V_S^2$, is known to increase with an increasing shear strain rate [103,104], additional adjustments were performed for the V_S profile based on the results of total stress equivalent-linear and nonlinear analyses for the small amplitude motions. These motions were used because they induce low shear strain levels, and their propagation is controlled by the elastic behavior defined by the velocity profile. Hence, the computed motion was compared with the observed response spectrum for multiple velocity profiles by a trial and error process until the best fit was reached. For all the sites, the adjustments were minor but improved the match to the observed low amplitude motion. Finally, for the two centrifuge tests, the data from the top accelerometer was considered as the observed surface motion in all the subsequent analyses.

4.2 Effective stress analysis - Calibration of the input parameters

In this section, the calibration of the input parameters of the effective stress models identified in Section 2.4 is presented. The following table presents these models and identifies their

input parameters. From the five models selected, the first four models are applicable to granular soils and the [29] is the only one representative of the clay behavior.

Table 4.1 Pore pressure generation models and input parameters (adapted from [18])

			Input parameters						
Model	Material	Eq.	1	2	3	4	5	6	7
Dobry & Matasovic (1988)	Sand	2.5	f	p	F	s	γ_{tvp}	v	-
Green-Mitchell-Polito (2000)	Cohesionless	2.8	α	D_R	FC	-	-	v	-
Park & Ahn (2013)	Sand	2.4	α	β	$D_{ru=1}$	CSR_t	-	v	-
Generalized (1985)	Cohesionless/Clay	2.7	α	β	-	-	-	v	-
Matasovic & Vucetic (1995)	Clay	2.9	s	r	A	B	C	D	γ_{tvp}

The discussion of Section 2.4.3 highlighted the limitations of the models and the uncertainty regarding the selection of the input parameters for these models. Thus, each model was calibrated several times with different approaches, to account for this uncertainty. The input parameters were selected based on the data available for each site, the recommendations included in the model's original publication by the authors or in the Deepsoil's user manual, and general correlations found in the literature. Where information was lacking and no well-validated correlation existed, realistic hypotheses were made as explained in Section 4.1. This section provides detailed information on the selection of the input parameters for each model. A summary of the calibrations that were established for all models and sites is presented in Table S2 in Appendix A.

4.2.1 Dobry & Matasovic (1988)

The Dobry & Matasovic model, which the general equation was presented in Section 2.4.1, is defined by 5 input parameters: γ_{tvp}, f, p, F, and s, where the latter two were the parameters subjected to different calibrations. [25] provided values for the parameters for 10 soils consisting of sand or silt, including the material at the WLA site ($f = 2$, $p = 1.04$, $F = 2.6$, $s = 1.7$, $\gamma_{tvp} = 0.02\%$, and $v = 1$). That study indicated that p varies within $\pm 7.1\%$ of 1, therefore a value of 1 was assumed. Parameter f was set to a value of 1 considering the unidimensional application. The parameters s and F were selected based on the correlations of [53] presented below.

$$F = 3810 \times V_S^{-1.55} \tag{4.4}$$

$$s = (FC + 1)^{0.1252} \tag{4.5}$$

For sites KSRH07 and TCGH16, no fines content values were available. In the investigation of [105], FC is typically between 0 to 20% for sands located in Japan. Thus, two calibrations with 1) $FC > 5\%$ and 2) $FC = 15\%$ were considered. For other sites and soil types, the fines content was determined based on average values from the Unified Soil Classification System (USCS), where $FC > 5\%$ for clean sands or gravelly soils, FC = 5-12% for sand with silt, FC = 12-50% for silty sand, and $FC > 50\%$ for silt or clay. Moreover, a recent study by [106] developed empirical correlations to estimate the parameter F based on the relative density D_R and the coefficient of uniformity c_u. When no data was available for c_u, two calibrations were considered, one with the upper ($c_u = 1.4$) boundary and the second one with the lower boundary ($c_u = 3.8$) of the [106] correlation. When not available, D_R was established from the correlations of [107], based on SPT test data for sites LSST and PIDA, or from [108] for sites KSRH07 and TCGH16.

For parameter γ_{tvp}, [31] found that γ_{tvp} = 0.01-0.02% for sand. Thus, one calibration with a constant value of $\gamma_{tvp} = 0.01\%$ for all layers was considered. In order to be consistent with the implementation of the clay model, a second calibration was considered using γ_{tvp} as the strain where $G/G_{max} = 0.65$. This followed the recommendations of [33] and [109] described in Section 4.2.5. For this calibration, the computed γ_{tvp} were found to be consistent with the values reported in [25]'s investigation.

4.2.2 Green-Mitchell-Polito - GMP (2000)

The Green-Mitchell-Polito (GMP) requires the following input parameters: α, D_R, and FC, and α was the only parameter that varied in the calibrations. α is a scale parameter introduced by Deepsoil and taken as 1 or 2 to match the laboratory data. For parameter PEC, [22] first introduced a graphical procedure to determine this value, which could not be integrated into the site response analyses. Thus, [52] developed the following correlation based on 145 cyclic triaxial tests.

$$ln(PEC) = \begin{cases} e^{0.0139} \cdot D_R - 1.021 & \text{for } FC < 35\% \\ -0.597 \cdot FC^{0.312} + e^{0.0139 \cdot D_R} - 1.021 & \text{for } FC \geq 35\% \end{cases} \tag{4.6}$$

4.2.3 Park and Ahn (2013)

For the Park and Ahn model, the following parameters are needed: α, β, $D_{r_u=1.0}$, and CSR_t, where parameter β was varied throughout the calibrations. The procedure for the selection of the parameters was based on the recommendations of [23] and [110]. These parameters

are calibrated from the cyclic stress ratio (CSR) vs the number of uniform stress cycles (N) curve obtained from stress-controlled testing, which is defined by:

$$CSR = \alpha \cdot N^{-b} \tag{4.7}$$

where a value of $b = 0.34$ is recommended for clean sands [16] and selected for all cohesionless soils for simplicity.

Since this curve is unavailable for all the sites in this study, the first step was to apply an empirical procedure to construct these curves. Preliminary work by [111] reported that the equivalent number of cycles (N) for a magnitude 7.5 earthquake is typically 15. Thus, the simplified liquefaction evaluation procedures described in Section 3.2 were used to evaluate the cyclic stress ratio for a magnitude 7.5 earthquake ($CSR_{M_w=7.5}$), and the value of a was estimated for each soil layer based on Equation 4.7 and considering $N = 15$ and $b = 0.34$.

Subsequently, a trial-and-error process was used to select the optimum values of CSR_t and α. The goal was to reduce the scatter of $D_{r_u=1.0}$, between adjacent data points of the curve (defined below) and provide the best match with the empirical CSR-N curve. The procedure consists in assuming a value for CSR_t and then calculating the parameter α based on the following equation.

$$\alpha_{avg.} = \frac{1}{M} \sum_{i=1}^{M-1} \left(\frac{log(\frac{N_i}{N_{i+1}})}{log(CSR_{i+1} - CSR_t) - log(CSR_i - CSR_t)} \right) \tag{4.8}$$

where M is the total number of data points of the reference $CSR - N$ curve and i refers to each data point. In this case, since the reference curve is empirical rather than obtained from laboratory data, 20 control points logarithmically space from $N = 1$ to 1000 cycles were selected.

The process was repeated until the coefficient of variation (COV) for α between adjacent data points was the lowest. Note that $D_{r_u=1.0}$ is defined by:

$$D_{r_u=1.0} = 4N(CSR - CSR_t)^{\alpha} \tag{4.9}$$

An example of the calibration of the parameters to the empirical curve is presented in Fig. 4.1 for a layer located at a depth of 3.9 m at site WLA. This layer is liquefiable and is composed of silty sand to sand. From the simplified liquefaction analysis, $CSR_{M_w=7.5}$ for $N = 15$ cycles was evaluated as 0.191, as indicated in Fig. 4.1, and $a = 0.480$ from Equation 4.7. Following the procedure described previously, the best fit between the empirical and the

calibrated curve was obtained when $\alpha_{avg.} = 2.938$, CSR_t = 1e-4, and $D_{r_u=1.0} = 0.463$.

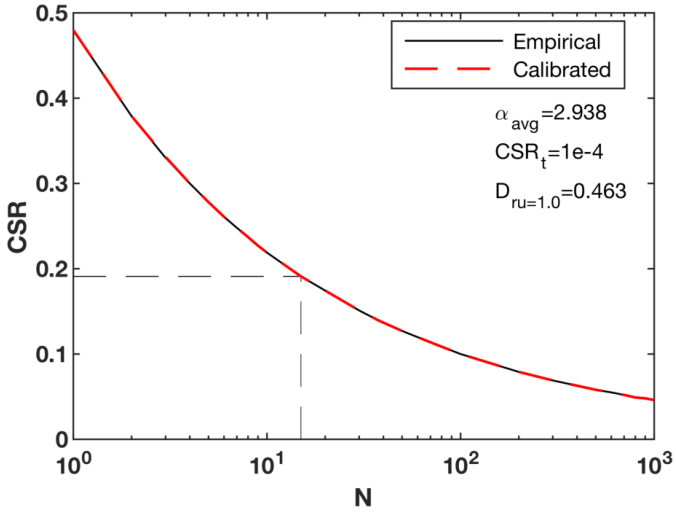


Figure 4.1 Example of the Park and Ahn calibration at the WLA site

Based on the recommendations of [110] and the experimental results reported in [36], [34], and [35] for clean sands, two calibrations were established with the upper and lower boundaries of 0.7 and 1.4 for the fitting parameter β. An additional calibration followed the correlation developed by [52] defined below.

$$\beta = c_1 FC + c_2 D_R + c_3 CSR + c_4 \tag{4.10}$$

where for $FC < 35\%$: $c_1 = 0.01166$, $c_2 = 0.007397$, $c_3 = 0.01034$, $c_4 = 0.05058$, and for $FC \geq 35\%$: $c_1 = 0.002149$, $c_2 = -0.0009398$, $c_3 = 1.667$, and $c_4 = 0.4285$.

4.2.4 Generalized (1985)

Only two input parameters are necessary to apply this model: α and β. Based on the recommendations of the authors [24], β was selected as 0.5. An additional calibration for β = 1.4 was added following the results previously discussed in Section 4.2.3. The parameter α was either defined similarly to the GMP model, considering the PEC calibration factor, or by a value of 1. In the calibration "M5", the Generalized model was applied to all soil types, not only granular soils. When applying this model to clay layers, the induced pore water pressures were overestimated compared to the expected behavior of cohesive soils, which typically have lower levels of pore pressures than in sands. Thus, by comparing with the data recorded by the pore pressure transducers in clayey soils for site WLA, a value of 0.15

for the parameter α was found to provide the best match to the measurements. This value was used for the other sites as well, and was found to be associated with the most realistic behavior for clays.

4.2.5 Matasovic & Vucetic (1995)

The [29] was applied only to the clay layers. The authors proposed the values for the required parameters for five clays based on strain-controlled testing. Prior work by [32] revealed that the plasticity index (PI) and overconsolidation ratio (OCR) influenced the cyclic degradation and pore pressure generation of cohesive soils. Thus, [53] developed correlations to account for the effect of these parameters on t which are presented below.

$$s = 1.6374 \times PI^{-0.802} \times OCR^{-0.417} \tag{4.11}$$

$$r = 0.7911 \times PI^{-0.113} \times OCR^{-0.147} \tag{4.12}$$

$$A = \begin{cases} 7.6451 & \text{for } OCR < 1.1 \\ 15.641 \times OCR^{-0.242} & \text{for } OCR \geq 1.1 \end{cases} \tag{4.13}$$

$$B = \begin{cases} -14.714 & \text{for } OCR < 1.1 \\ -33.691 \times OCR^{-0.33} & \text{for } OCR \geq 1.1 \end{cases} \tag{4.14}$$

$$C = \begin{cases} 6.38 & \text{for } OCR < 1.1 \\ 21.45 \times OCR^{-0.468} & \text{for } OCR \geq 1.1 \end{cases} \tag{4.15}$$

$$D = \begin{cases} 0.6922 & \text{for } OCR < 1.1 \\ -3.4708 \times OCR^{-0.857} & \text{for } OCR \geq 1.1 \end{cases} \tag{4.16}$$

where PI was defined in Section 4.1.2 and OCR was taken from 1 to 4 based on the geological descriptions of the soil layers and common values found in the literature. Finally, γ_{tvp} is selected as the strain where $G/G_{max} = 0.65$ from the modulus reduction curve, following the recommendations of [33] and [109].

4.2.6 Degradation parameter

The degradation parameter v varies from 1 to 5 based on prior work by [25]. Thus, values of 1, 2.5 and 5 were considered for all models in different calibrations.

Recently, [58] proposed the correlation described in Equation 4.17 for parameter v. However,

this was not used in the present study since the selected values of v mentionned above cover the range proposed in this calibration.

$$v = 1 < 0.078 \cdot D_R < 3.8 \tag{4.17}$$

4.2.7 Dissipation and redistribution parameters

In this work, the dissipation of pore water pressures was considered for all analyses. Since rapid loading results in undrained conditions, this factor was expected to have limited impact on the results. For the centrifuge experiments (CSP3 and CSP2) and sites KSRH07 and TCGH16, for which the downhole accelerometer is located in a rock layer, the bottom boundary condition was considered as impermeable. For the other sites (WLA, LSST, and PIDA), the bottom layer consists of clayey silt or clay. Since the permeability of these layers was unknown, the analyses were conducted considering both permeable and impermeable boundary conditions at the bottom of the soil profile. However, the comparison with the ground response analyses confirmed that the specification of the permeability of the boundary condition had limited impact on the accuracy of the predictions for these sites. For clays, similarly to [53], c_v was defined based on the following correlation from [112]:

$$c_v = 0.79861 \times LL^{-2.7905} \tag{4.18}$$

where LL is the liquid limit estimated from the geological soil layer descriptions and common values based on [87]. For cohesionless soils, the consolidation coefficient c_v was defined by the following correlation:

$$c_v = \frac{k}{m_w \gamma_w} \tag{4.19}$$

where k is the permeability, m_v is the coefficient of volume compressibility and γ_w is the unit weight of water. The coefficient k was selected based on the soil description and the proposed classification of [113] and [90]. Thus, k = 5e-3 m/s was selected for gravels, k = 5e-4 m/s for sands, and k = 5e-6 m/s for silty sands. The coefficient m_v was determined depending on the soil type from reported values of [114] and [115]. An average value of m_v = 4e-5 kPa^{-1} was considered for sands and m_v = 5e-6 kPa^{-1} for gravels.

CHAPTER 5 RESULTS AND DISCUSSION

This chapter begins by comparing the predictions of the site response models with the detailed case study of the Wildlife Liquefaction Array [68, 70]. The results of the predictions for all sites and ground motions are then studied by grouping the effective stress analysis by models. Observed and predicted spectral accelerations, amplification spectra, ground motion intensity parameters and pore pressure response are compared, and the uncertainty of the predictions are quantified.

5.1 Wildlife Liquefaction Array (WLA) case study

The results are first presented for the case study of the 1987 Superstition Hills Earthquake ($M_w = 6.6$ & $PGA_{obs-surf} = 0.19$ g) recorded at the Wildlife Liquefaction Array site (WLA). The goal of this section is to provide a detailed example of an analysis and how the predictions of EQL, NL-TS and NL-ES are compared with a recording, and to demonstrate the influence of liquefaction on the seismic response at a site.

EQL, NL-TS and NL-ES ground response analyses were conducted with input parameters calibrated based on the available soil properties, which were presented in Section 3.3.3, and following the procedure presented in Section 4.2. Note that the available site properties, including the geological profile description, ground water level, fines content, liquid limit, plasticity index, coefficient of uniformity, velocity profile and CPT tip resistance (mean of data from tests Cg#1@3 in [68], are presented in Fig. 3.7. For the effective stress model, the GMP model with calibration M2.1 is considered herein with the input parameters $\alpha = 1$ and $v = 1$.

The results presented in Fig. 5.1 show that the effective stress analysis predicts the triggering of liquefaction in the liquefiable layer from 2.5 to 6.8 m, as shown in the pore pressure response expressed as a function of time and depth in Fig. 5.1d and 5.1h, respectively. Liquefaction leads to a significant loss of the soil's stiffness and strength which is associated with large shear strains, reaching a maximum value of 13% in this case, as presented in Fig. 5.1f. Overall, this behavior leads to a lower predicted PGA values (Fig. 5.1e), when compared to the total stress analyses, particularly in the layer overlaying the liquefiable layer. Lower stress ratios are obtained in Fig. 5.1g, defined as the ratio of the shear stress over the effective vertical confining stress, are compared with the total stress analyses.

Regarding the pseudo-acceleration response spectrum, as shown in Fig. 5.1a, all analyses

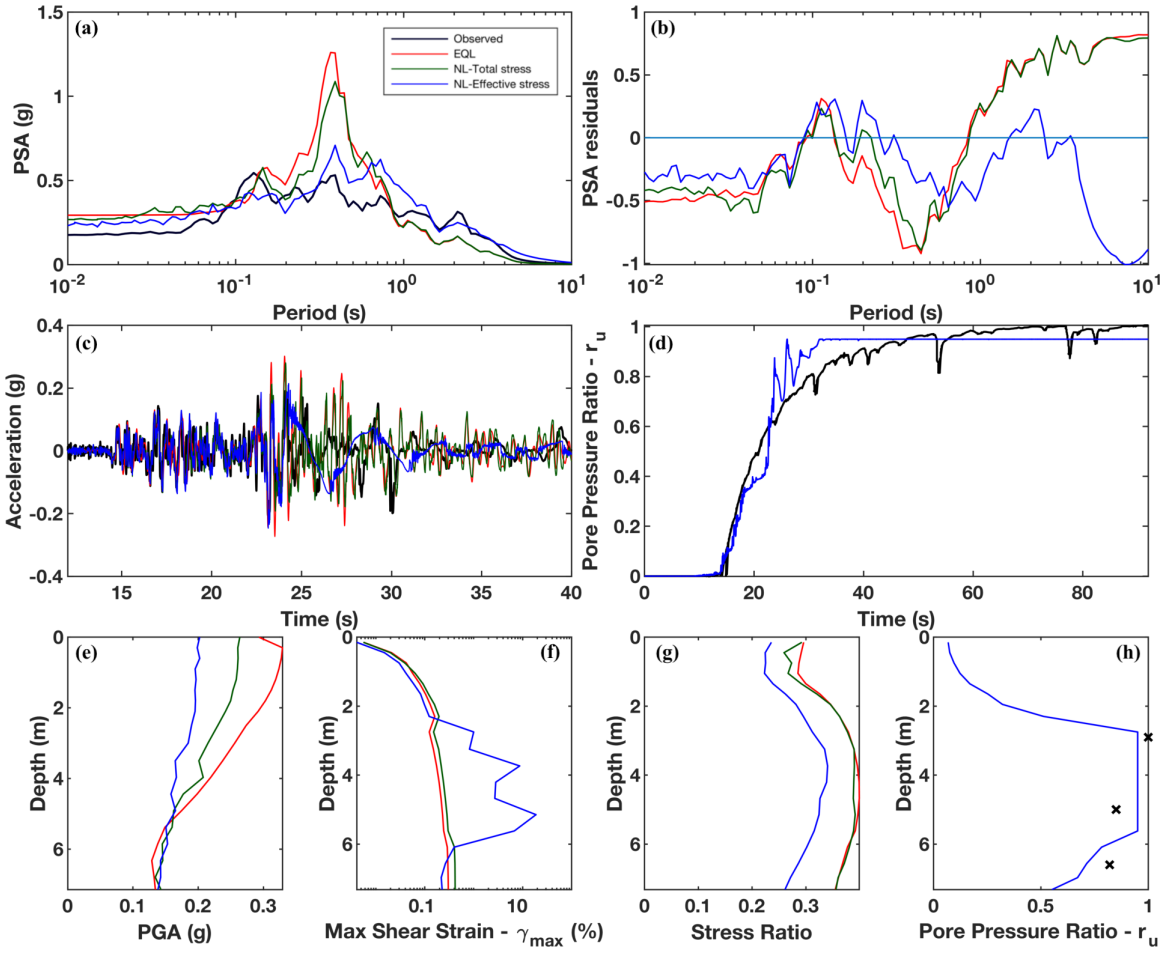


Figure 5.1 Wildlife liquefaction case study for the Superstition Hills Earthquake. Results from total stress equivalent-linear (EQL), total stress nonlinear (NL-TS) and effective stress nonlinear (NL-ES) analysis with GMP model (M2) and calibration M2.1: (a) Pseudo-acceleration surface response spectra, (b) Response spectra residuals, (c) Surface acceleration time histories for NS direction, (d) Pore pressure response at 2.95 m depth, (e) Peak ground acceleration profile, (f) Maximum shear strain profile, (g) Stress ratio profile and (h) Pore pressure ratio profile for the NL-ES analysis.

under-predict the motion at periods shorter than 0.05 s. Several observations of past earthquakes have reported that lower frequencies are typically amplified following liquefaction [65], and this is reflected in the predictions of the total stress analyses which neglect liquefaction effects and under-predict the motion for periods longer than 0.8s. Conversely, the NL-ES analysis shows the ability to capture some of the low frequency content induced by liquefaction effects from 0.8 to 3 s. However, the response at longer periods ($T > 3$ s) and the change in the frequency content of the acceleration time series, presented in Fig. 5.1c, are overpredicted. This can be attributed to the overestimation of soil softening and degradation

by the pore pressure generation model for this specific calibration.

Finally, regarding the pore pressure response as a function of time presented in Fig. 5.1d, shows that the model captures the offset of pore pressure generation, at approximately 13 seconds, which compares well with the observed records obtained from [72]. However, the triggering of liquefaction was predicted to occur more rapidly than what was recorded. The comparison may, however, be misleading since previous research has challenged the accuracy of the pore pressure recordings [71,116,117]. It is also noticed that after reaching liquefaction, constant pore pressures are obtained, while the expected behavior would normally show some variations. This predicted behavior could be a consequence of the difficulty of the models in modeling dilatancy.

5.2 Centrifuge tests

Preliminary results indicated that the predictions of the centrifuge tests (CSP3 and CFF2) differed significantly from the observations, even for low amplitude motions. The first blind predictions exhibited a higher error compared to what was obtained for the downhole seismic array sites. Therefore, an attempt was made to modify the dynamic properties in order to correct this bias. The following section discusses the observed and modeled initial and modified responses, and the factors affecting the computed error.

5.2.1 CSP3

In Fig. 5.2 are presented the results of EQL, NL-TS and NL-ES ground response analyses for the test CSP3 for motion EQ4. The pore pressure generation model used in the NL-ES analysis is Dobry and Matasovic with calibration M1.1 (Table S2). The recorded pore pressure response is obtained from the pore pressure transducer #52 located near the surface at a depth of 1m in prototype scale. The results presented in Fig. 5.2a-b reveal an underestimation of the response at short periods from all the models. The observed records show that the acceleration time series exhibit high amplitude-high frequency acceleration pulses. These large spikes appear to be a consequence of the soil's dilative response following the generation of excess pore water pressure, which was detailed in Section 2.4.3. At the time of occurrence of those spikes, the dilative response is also expressed by the sudden decrease in excess pore pressure which increases effective stresses and consequently induces a stiffening of the soil and, which allows the amplification of a portion of the motion. The results demonstrate that effective stress models fail to properly account for this dilative behavior and underestimate the high frequency component of the motion. This confirms the findings of [58], who showed

that the GQ/H+u model, which considers excess pore pressures, leads to less precision for the motions in their data set where $r_u > 0.8$, due to the neglect of difficulty in reproducing the dilative behavior. Note that a similar response to EQ4 was also obtained for the other high amplitude motions used during this test, such as motions 5, 7, 9, and 10, which had pore pressure ratios higher than 0.95.

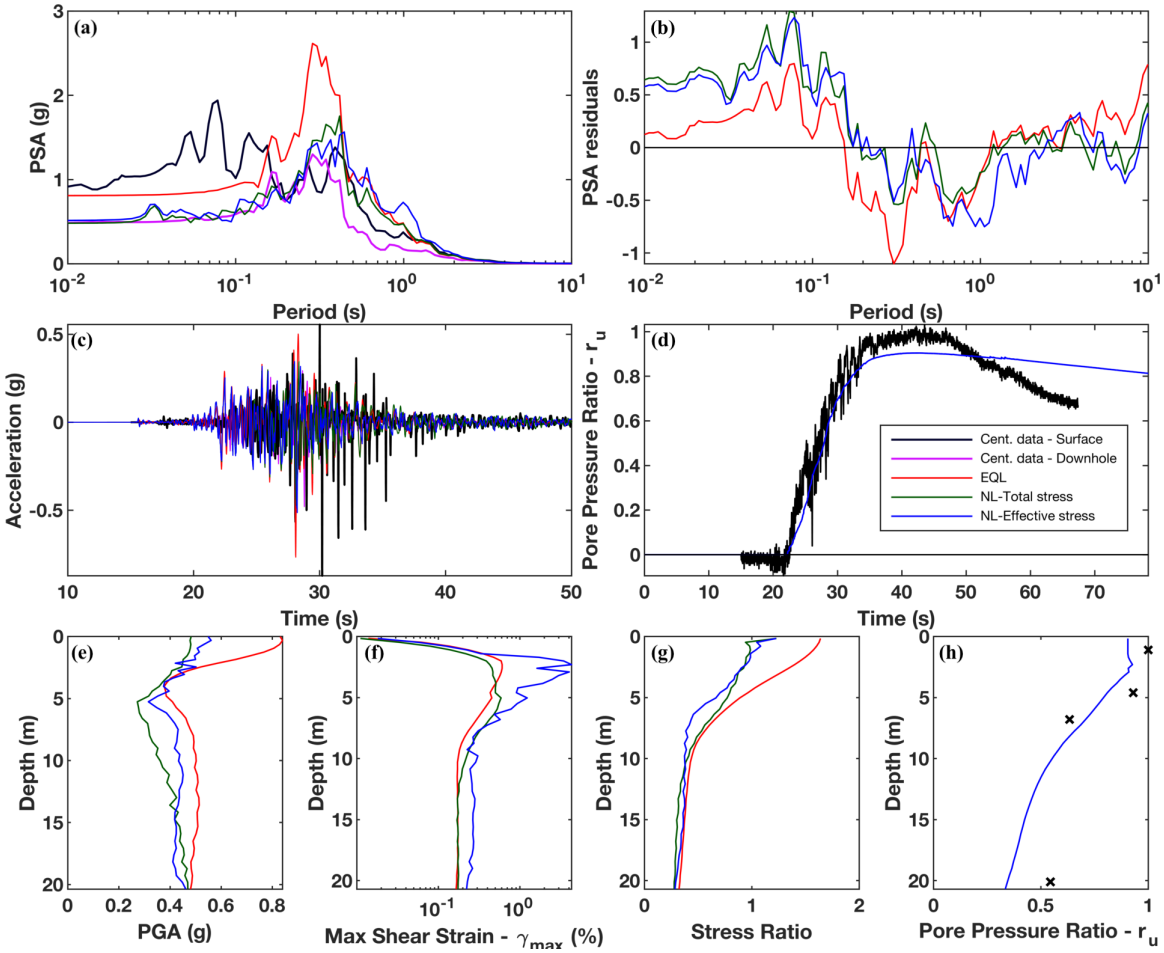


Figure 5.2 Results from total stress equivalent-linear (EQL), total stress nonlinear (NL-TS) and effective stress nonlinear (NL-ES) analysis with the Dobry and Matasovic model (M1) and calibration M1.1 for EQ#4 of centrifuge test CSP3: (a) Pseudo-acceleration surface response spectra, (b) Response spectra residuals, (c) Surface acceleration time histories, (d) Pore pressure response in the middle of the liquefiable layer at 1m depth from #P52, (e) Peak ground acceleration profile, (f) Maximum shear strain profile, (g) Stress ratio profile and (h) Pore pressure ratio profile for the NL-ES analysis

5.2.2 CFF2

For centrifuge test CFF2, the error was found to be more important for the high amplitude motions, which supports previous findings in [84] discussed in more detail later in Section 5.2.3. Also, the computed behavior was found to differ from the response in test CSP3 and the observations, since the amplitude of the computed residuals is more important. Note that for the first motion applied in the centrifuge, representing a low amplitude motion of the 1992 Landers earthquake, recorded at the Joshua Tree station and presented in Fig 5.3, the *PGA* was fairly well captured by the nonlinear models.

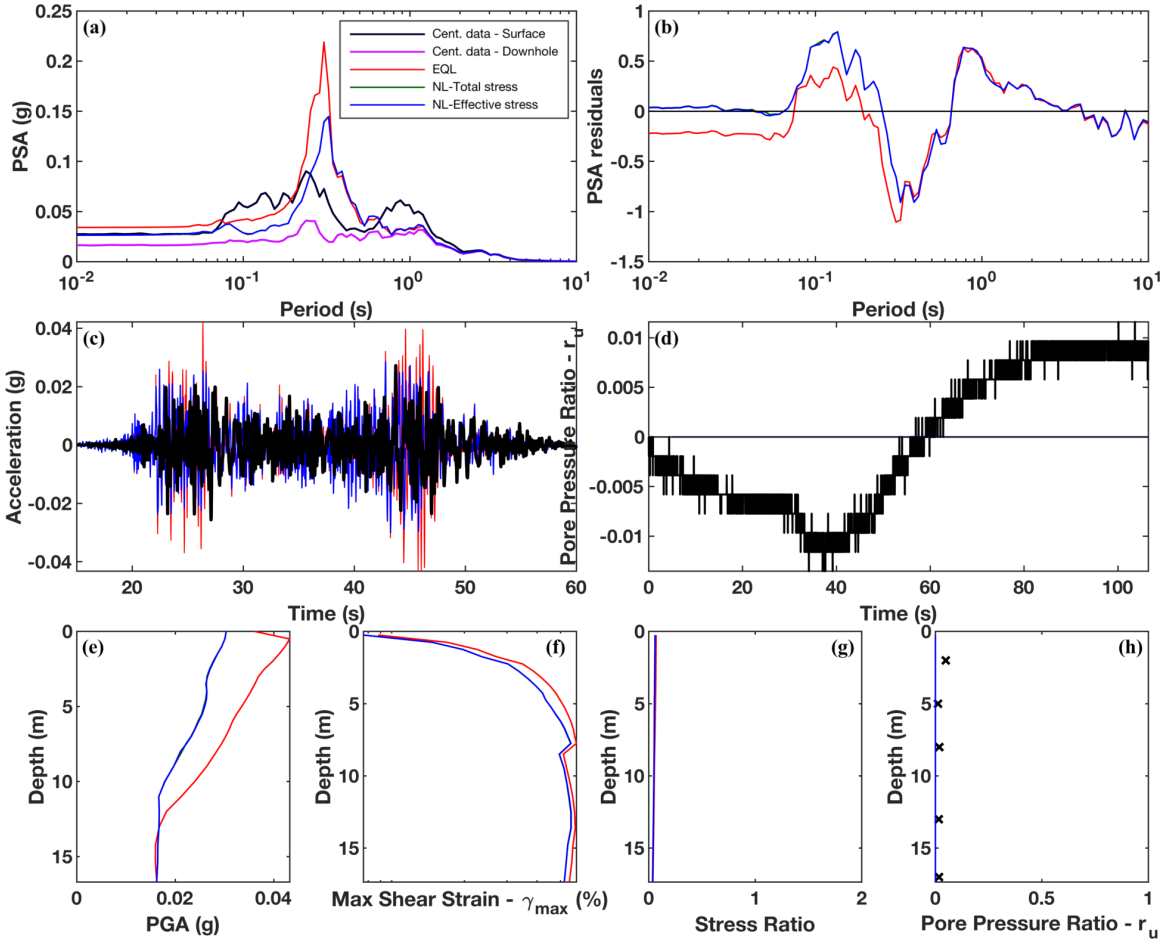


Figure 5.3 Results from total stress equivalent-linear (EQL), total stress nonlinear (NL-TS) and effective stress nonlinear (NL-ES) analysis with the Dobry and Matasovic model (M1) and calibration M1.1 for EQ#1 of centrifuge test CFF2: (a) Pseudo-acceleration surface response spectra, (b) Response spectra residuals, (c) Surface acceleration time histories for NS direction, (d) Pore pressure response at 5 m depth, (e) Peak ground acceleration profile, (f) Maximum shear strain profile, (g) Stress ratio profile and (h) Pore pressure ratio profile for the NL-ES analysis.

However, for the other motions with high pore pressure generation, the predictions of the response spectrum of the total stress model were an order of magnitude different from the observations at short periods. The comparison between the site response analyses and the records for motion EQ#2, a recording from the 1994 Northridge earthquake at Newhall-WPC station, is provided in Fig. 5.4 for the calibration M1.1 of the Dobry and Matasovic model. The recorded pore pressure response was obtained from the pore pressure transducer #P8 located in the middle of the loose Nevada sand layer at a depth of 5 m.

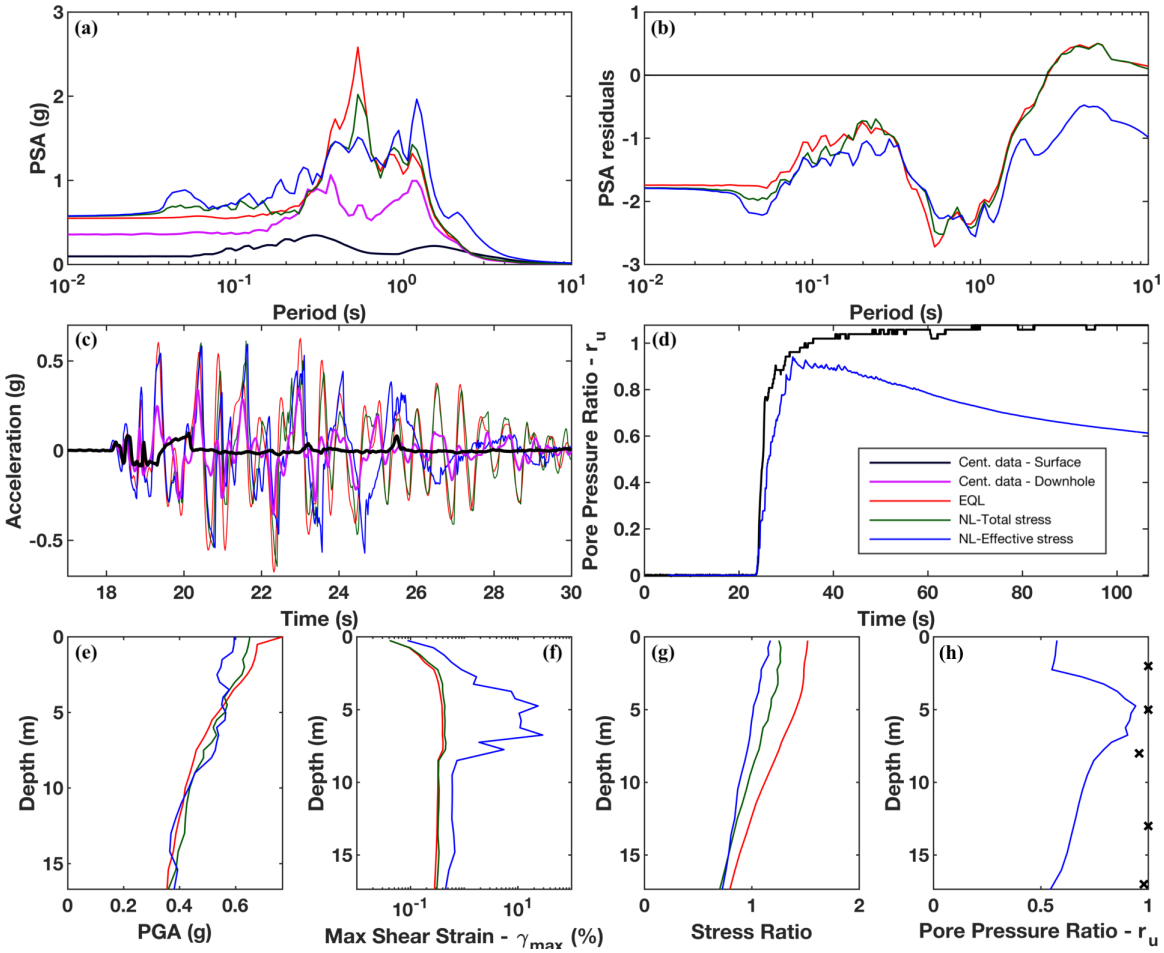


Figure 5.4 Results from total stress equivalent-linear (EQL), total stress nonlinear (NL-TS) and effective stress nonlinear (NL-ES) analysis with the Dobry and Matasovic model (M1) and calibration M1.1 for EQ#2 of centrifuge test CFF2: (a) Pseudo-acceleration surface response spectra, (b) Response spectra residuals, (c) Surface acceleration time histories for NS direction, (d) Pore pressure response at 5m depth, (e) Peak ground acceleration profile, (f) Maximum shear strain profile, (g) Stress ratio profile and (h) Pore pressure ratio profile for the NL-ES analysis.

The results of Fig. 5.4a-c show that the models fail to account for the attenuation of the

motion through the profile and greatly overestimate the response for all periods for the NL-ES analysis and over short to moderate periods for the EQL and NL-TS analyses. Besides, in contrast to the recordings of liquefaction over the entire depth of the profile, liquefaction is only predicted in the middle layer composed of loose Ottawa sand (Fig. 5.4h). A similar response and associated bias were found in motions 3, 5, and 6. The attenuation of the observed response for these motions is due to the increased softening related to the prediction of liquefaction through all the layers in the profile. In opposition, the response of motion EQ4, presented in Fig S1 of Appendix A, differed from these since the bottom denser layer of Ottawa sand did not fully liquefy, although large pore pressure ratios were measured ($r_u > 0.8$). This led to larger dilative tendencies, as observed in the surface acceleration records, and re-stiffening of the soil which allowed the amplification of the motion at the surface [83]. The behavior for this motion is similar to the high amplitude motions of test CSP3, showed in Fig. 5.2, where the models under-predicted high frequencies due to high dilative tendencies.

5.2.3 Modifications to the site properties

For both centrifuge tests, the first blind predictions that were conducted to test the calibrations of the dynamic input parameters showed large computed residuals. While the discussed evidence suggests that this mismatch is a consequence of poorly capturing dilative tendencies, uncertainty remained regarding the selection of the dynamic parameters for centrifuge tests. Therefore, modifications were attempted to adjust the calibrations of the dynamic parameters at these sites in order to provide a better fit to the observed response for low strain motions. First, since no velocity profiles were available, multiple velocity profiles were tested for the small amplitude motions, as was previously discussed in Section 4.1.5. Second, the small-strain damping ratio computed from empirical relationships was increased following previous work [118–120] that suggested that higher viscous damping values were found in centrifuge experiments than in laboratory tests. Following these adjustments, no significant improvements in the predictions were made compared with the original blind predictions. This suggests that other factors, such as strain rate effects or boundary conditions could also potentially influence the results [121].

For test CFF2, the results presented in Fig. 5.4, with regard to the amplitude of the calculated bias, were found to be in accordance with the findings reported in [84], where numerical simulations, using the PDMY02 and SANISAND models in OpenSees, of the same centrifuge tests led to a similar overprediction of the response observed in Fig. 5.4. In this study, advanced constitutive models were calibrated based on the same set of centrifuge test data. A second calibration of the models was introduced to account for the bias which was found to

be associated with excessive dilative tendencies, confirming the above discussion. However, current available 1D effective stress models used in this study do not allow for the proper consideration of dilatation and such modifications are impossible to implement. Therefore, considering the scope of this research, and the desire to avoid overfitting, no further investigation was conducted in the present study to improve the predicted response at those sites.

Considering that dilative tendencies may have a larger influence on the dynamic response of these centrifuge tests than that of the seismic arrays, and are not well captured by the current 1D effective stress models, two different scenarios are investigated in the following sections, as presented in Table 5.1.

Table 5.1 Description of the motions considered at each site for the two analyzed scenarios

Scenario	Seismic arrays	CSP3	CFF2
1- No dilatation pulses	All	1, 2, 3, 6, 8, 11, 12, and 13	1
2-All motions	All	1-14	1-6

The first scenario neglects the motions at the centrifuge tests where evidences of high-amplitude high-frequency pulses associated with increased dilative behavior were observed in the acceleration time histories in order to limit the influence of this component on the results from the other downhole array sites. The second condition considers all 98 motions at the seven sites.

5.3 Validity of 1D assumptions of the sites

In order to verify the validity of the assumption that the selected sites can be modeled accurately by 1D ground response analyses, the procedure proposed by [67] was used herein. This procedure consists in evaluating the inter-event variability and the goodness-of-fit between the empirical (ETF), derived from the data, and theoretical ($SH1D$) transfer functions computed from classic analytical solutions, as described in [37]. First, the inter-event variability is evaluated as the median standard deviation σ_i of the ETF of the linear motions, defined for motions with low PGA ($< 0.1\ g$). Then, the Pearson's correlation coefficient r is computed by comparing the ETF and $SH1D$. Note that these computations are only made at periods between the first and fourth modes of the sites. A recent study conducted by Tao and Rathje (2020) suggests that increasing the value of minimum damping (ξ_{min}) yields higher computed r values. A potential explanation for this is associated with the fact that the r values are

significantly influenced by the amplitude of the peaks, as reported in [122]. Fig. 5.5 presents the median ETF, 95% confidence interval, and $SH1D$ of each site, and $SH1D$ computed for 4 times ξ_{min}. Note that the application of this procedure is found to be less appropriate for sites CFF2 and PIDA, but are showed for consistency. This is due to the fact that only 3 and 2 motions, respectively, are considered for those sites. The computed standard deviations σ_i and correlation coefficients r of each site for each method are summarized in Table 5.2.

Table 5.2 Computed standard deviations and correlation coefficients at each site

Site	Number of motions	Inter-event variability σ_i	Correlation Coef. – r	Correlation Coef. – r Increased ξ_{min}
KSRH07	13	0.51	0.3	0.38
TCGH16	6	0.49	0.23	0.31
WLA	13	0.42	0.29	0.43
CSP3	6	0.44	0.22	0.24
CFF2	3	1.24	0.24	0.3
LSST	9	0.41	-0.004	0.08
PIDA	2	0.46	0.15	0.28

The results show that σ_i ranges from 0.41 to 1.24 and r from -0.0044 to 0.30. [67] originally proposed boundaries of $\sigma = 0.35$ and $r = 0.6$ to distinguish between low inter-event variability and good fit to $SH1D$, respectively. While these are arbitrary, the computed values appear to remain close to these boundaries, in particular in terms of inter-event variability, with the exception of site CFF2, which behavior was previously identified as being problematic as discussed in Section 5.2. The coefficients of correlation are low, but positive, with the exception of site LSST, which was slightly negative since the peaks are not well aligned. In addition, [67] recommend applying such procedure only to sites where at least 10 linear motions are considered. Increasing ξ_{min} reduces the amplitude of the peaks at all sites, as illustrated in Fig 5.5. This leads to slightly higher computed r values, ranging from 0.08 to 0.43, confirming the findings reported in [123]. Thus, considering the scarcity of recorded liquefaction cases in downhole arrays, the selection of sites was rather limited, and on the basis of the results presented in Table 5.2 and these discussed limitations, 1D ground response analyses were deemed appropriate to model the selected sites.

5.4 Quantification of uncertainty

The uncertainty of the predictions for each model was quantified by computing the residual in the logarithmic space between the observed and computed 5%-damped pseudo-acceleration spectra (PSA) of the surface motion, defined by Equation 5.1. For records with both hor-

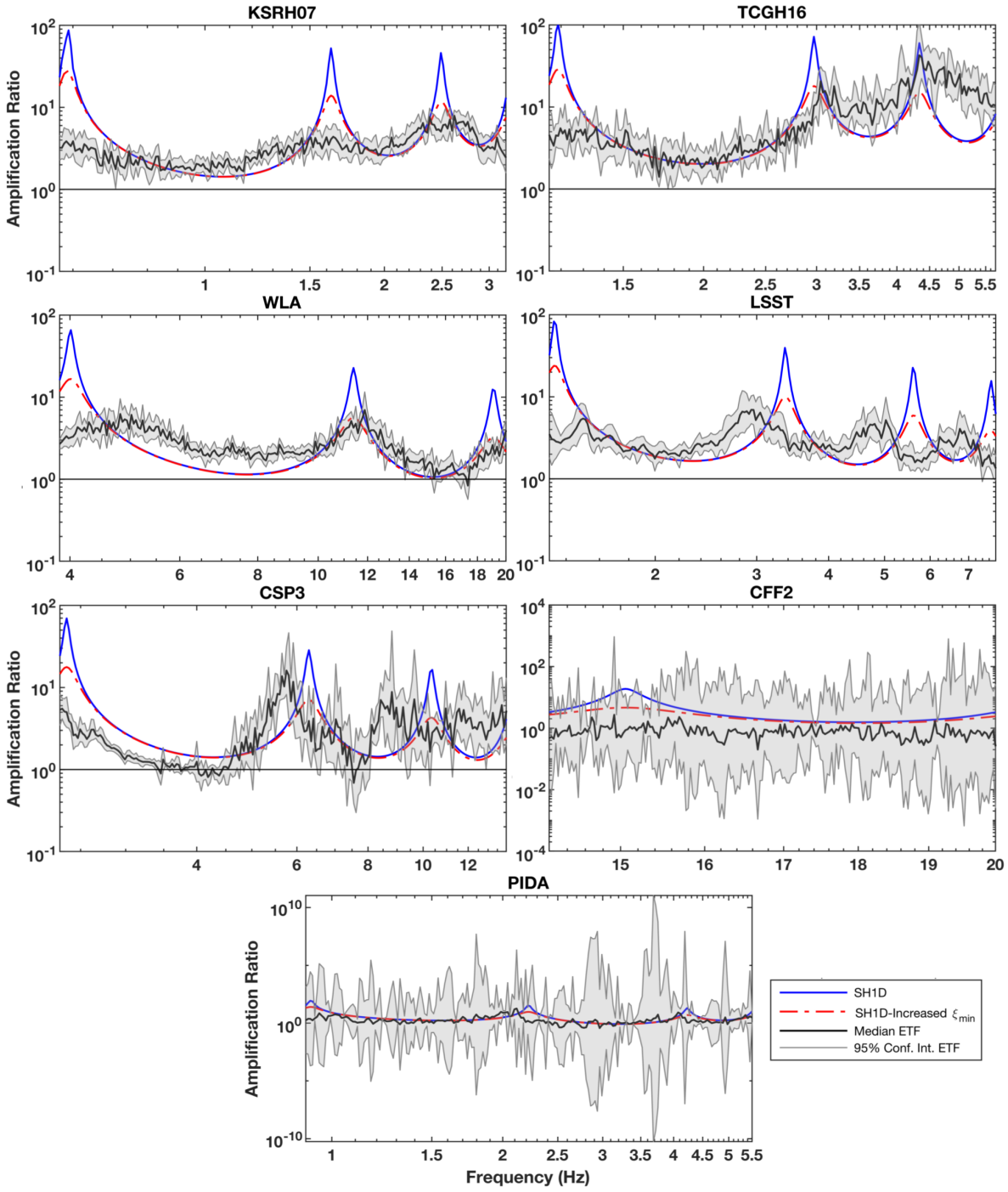


Figure 5.5 Median empirical transfer function (ETF), 95% confidence interval and $SH1D$ at each site.

izontal components of the motion, the geometric mean was used to combine the results. Note that a positive and a negative residual are associated with an under-prediction and an

over-prediction of the motion, respectively.

$$PSA_{res} = ln[PSA_{obs}(T)] - ln[PSA_{pred}(T)] \tag{5.1}$$

In order to estimate the uncertainties of the site response models, a linear mixed-effect regression analysis was performed considering the residuals across all sites and ground motions. This statistical analysis allows for the evaluation of the repeatable model bias and variability of the models. Fixed and random effects are combined to represent the trends when the data is grouped by one or more classification factors. In this context, the ground motion observations are grouped by site. This approach is based on [124] and [7] and the general form of the regression is expressed in Equation 5.2.

$$PSA_{res}(T)_{i,j} = a + \eta_{Si} + \epsilon_{i,j} \tag{5.2}$$

where a is the population mean (fixed-effect), η_{Si} is the inter-site residual (between-site residual), and $\epsilon_{(i,j)}$ is the intra-site residual (within-site residual). In this context, η_{Si} represents the difference between the mean of the residuals at site i and the population mean a. $\epsilon_{(i,j)}$ refers to the variation of the residual for ground motion record j at site i with η_{Si}. Both intra and inter site residuals are normally distributed zero-mean random variables with inter-site standard deviation τ_S, which describes the variability of the residuals between sites, and intra-site standard deviations σ_0, which represents the variability within a single site. The total standard deviation σ_Y of the site response models is defined by Equation 5.3.

$$\sigma_Y = \sqrt{\sigma_0^2 + \tau_S^2} \tag{5.3}$$

The regression parameters a, τ_S, σ_0, and σ_Y were used in the following analyses to quantify the bias and variability across all site response models.

Ground response analyses were conducted for EQL, NL-TS, NL-ES considering all seven sites, 98 ground motions and 34 calibrations for the pore pressure generation models. Since the calibrations are not applied at all sites, depending on the available soil properties, as discussed in Section 4.2, a total of 3020 analyses were conducted. Note that only the calibrations that were applied to all sites are considered in the following analyses considering the mixed-effect regression formulation, as identified in Table S2. Therefore, the following calibrations were not included in this analysis: M1.3, M1.4, M1.6, M1.8, M1.9, M2.4, M2.6, M3.3, M3.4, M3.7, M4.4, M4.7.

First, the calibrations between the individual models are compared in order to provide insight

into the selection of the input parameters as presented in Fig. 5.6. The comparison is made from the results of the mixed-effect regression analysis. In this analysis, only the calibrations that were used for all sites are considered due to the mixed-effect regression formulation. The other calibrations were analyzed separately for each site but were not included in this study for simplicity.

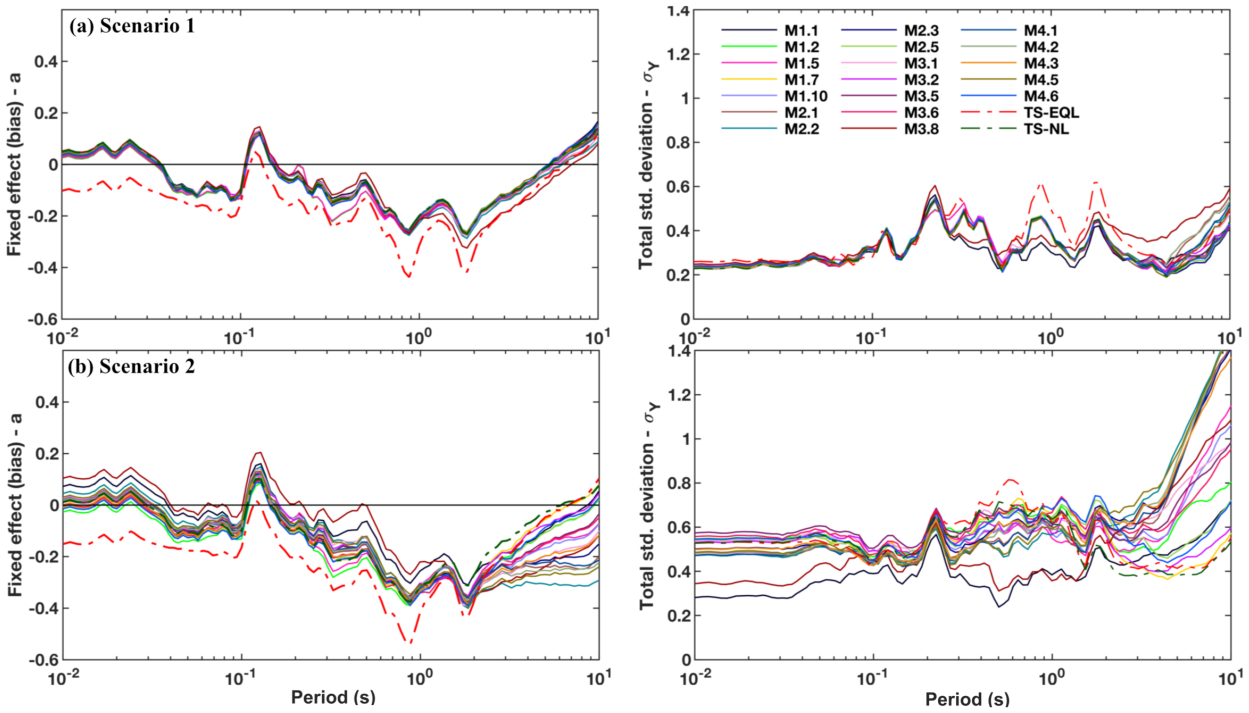


Figure 5.6 Period dependence of the mixed effect regression analysis across all sites and ground motions. Results from NL-ES analysis and calibrations applied at all sites: (a) scenario 1 (b) scenario 2.

In general, for Fig. 5.6a the results show that the comparison between the computed bias and variability from the individual calibrations remain mostly constant through all the spectrum when motions most influenced by dilatation spikes are not considered, with the exception of M3.8 that has an increased total variability at long periods. For all motions, presented in Fig. 5.6b, differences between the individual calibrations are observed through all the periods in terms of both accuracy and variability. In general, none of the calibrations appear to significantly improve the accuracy when compared to the results of the total stress analysis. In particular, in terms of the total variability of the residuals, the results show that the predictions of the calibrations tend to diverge at periods longer than 2 s, although calibrations M1.1 and M3.8 show significantly less variability. When comparing the individual calibrations within each model, the calibrations with an increase in the degradation parameter to $v =$

2.5 or 5, yielded the lowest variability at longer periods (M1.2, M1.7, M2.3, M2.5, M3.5, M4.3, and M4.6). In addition, the calibrations M2.2 with $\alpha = 2$, M3.8 with β obtained from the [52] correlation, M4.2 with $\beta = 1.4$, and M4.5 with $\alpha = 1$, showed the highest computed bias and variability compared to the other calibrations within each model.

The comparison between the individual calibrations for a given model showed low variability. Thus, the effective stress results are separated by the pore pressure generation model employed and all the individual calibrations are averaged per model. Mixed-effect regression analysis was performed and the results are first presented in Fig. 5.7 in terms of bias (a) and variability (b-d) for the scenario 1 as identified in Table 5.1.

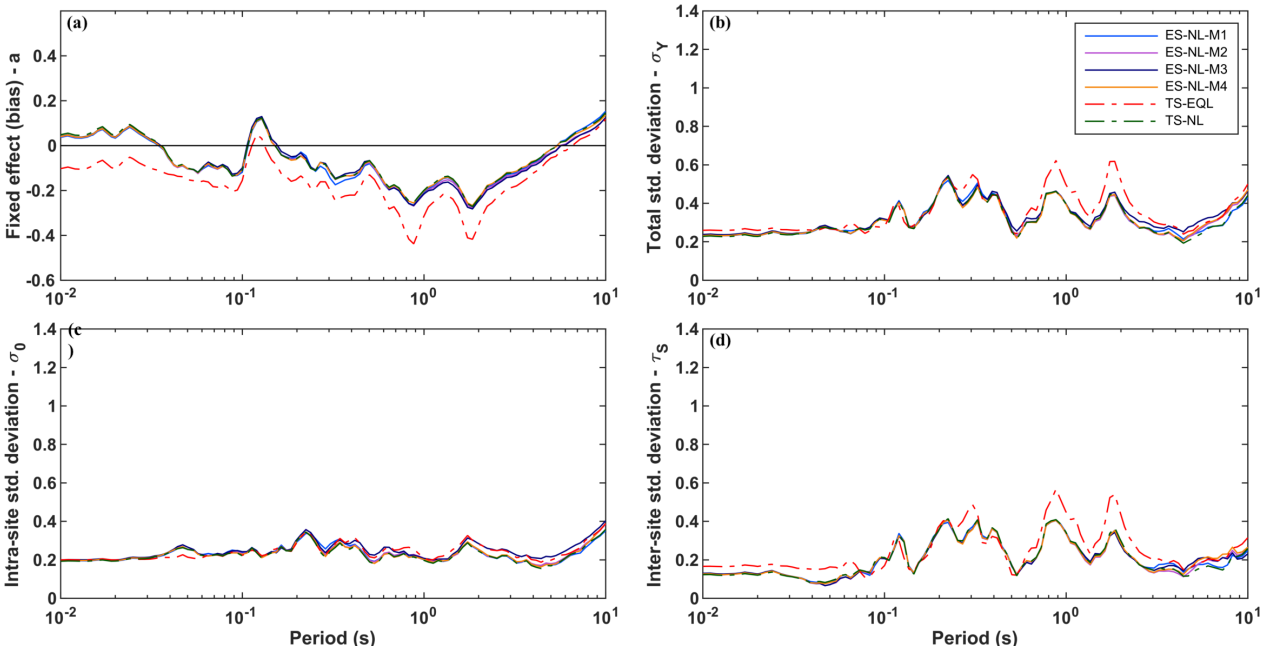


Figure 5.7 Period dependence of the mixed effect regression analysis across all sites and ground motions. Results from EQL, NL-TS and NL-ES analyses for scenario 1: (a) Model bias or fixed effect a, (b) Total standard deviation σ_Y, (c) Intra-site standard deviation σ_0 and (d) Inter-site standard deviation τ_S.

In general, the study of the model bias revealed that NL-TS and NL-ES models provide similar accuracy for all periods. The nonlinear models tend to under-predict the motion at periods shorter than 0.035 s and longer than 6s. In between those values, the bias is negative and indicates an over-prediction of the motion. For the EQL analysis, the results reveal an increased negative bias for most periods, thus clearly indicating the advantages of using NL models. With the exception of the results of EQL, these results tie well with previous studies wherein similar tendencies were found [7–10, 14]. In particular, these studies

suggested that the bias at high frequencies (i.e. short periods) is due to inaccuracies in the modeling assumptions. These include multidimensional site effects, such as 3D site stratigraphy and basin effects, which are not accounted for, due to the limitation of the unidimensional assumption. The selection of dynamic model parameters, such as viscous damping and boundary conditions [10], velocity profiles, and modulus reduction and damping curves might also lead to a similar bias. In terms of the variability of the residuals, the results show nearly constant low intra-site variability across the spectrum ranging from 0.2 to 0.4 and increased variability in the inter-site standard deviation which ranged from 0.2 to 0.6 approximatively. The results from the NL analyses revealed a decrease in the inter-site variability for periods shorter than 4.5 s when compared with the EQL analysis. In general, for these motions, the comparison between the NL-TS analysis and NL-ES were found to show few differences.

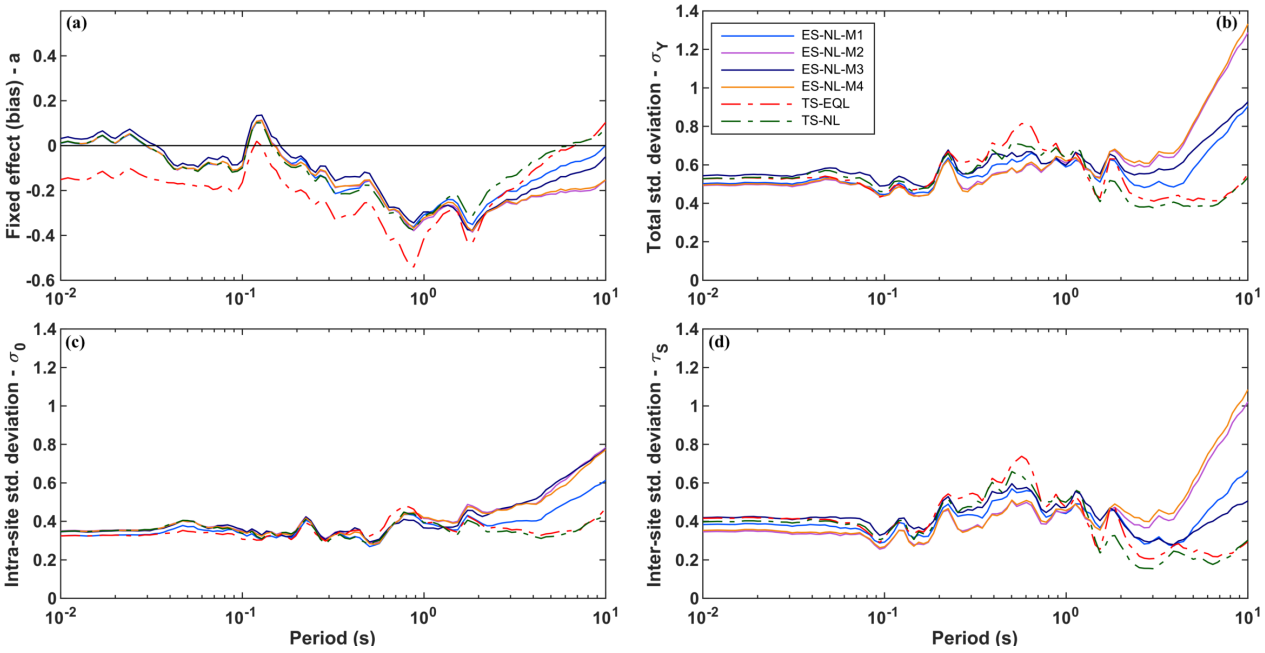


Figure 5.8 Period dependence of the mixed effect regression analysis across all sites and ground motions. Results from EQL, NL-TS and NL-ES analysis for scenario 2: (a) Model bias or fixed effect a, (b) Total standard deviation σ_Y, (c) Intra-site standard deviation σ_0 and (d) Inter-site standard deviation τ_S.

The results of the mixed-effect regression analysis for the second scenario considering all the motions as described in Table 5.1 are presented in Fig. 5.8. Regarding model biases, while the short periods were identified as being problematic in Section 5.2, due to increased softening associated with liquefaction or dilatation, the bias at those periods does not appear to be significantly altered compared with the results reported in Fig. 5.7. However, the results in

Section 5.2 showed that centrifuge test CSP3 underestimated the response at those periods, while test CFF2 led to its over-estimation. Therefore, the application of the mixed-effect regression appears to lead to the cancellation of the respective errors that were found at each site for short periods. By comparing the two conditions presented in the previous figures, the main finding is associated with the significant increase of the amplitude of both intra and inter-site standard variation for all the models. Moreover, the biases and variabilities were found to significantly diverge at long periods, which were identified previously as being the periods that are the most affected by liquefaction effects.

Overall, the comparison between the effective stress models shows similar accuracy and tendencies across all panels with none of them improving the accuracy or precision. In general, the results did not demonstrate a clear improvement in the use of effective stress models over total stress models when considering a database of recordings with varying ground motions amplitudes.

The results presented herein showing increased variability clearly illustrate the limitation of the models in their tendencies of poorly modeling dilatancy when considering the motions of the centrifuge tests that seems to be the most affected by dilatation spikes. Note that the inspection of the time histories of some other motions at the downhole array sites allowed the identification of dilatation spikes as well. However, the response was found to be less affected than in the centrifuge tests and no significant errors were noticed.

5.5 Accuracy of the predictions

In addition, Pearson's correlation coefficients r were used to assess the accuracy of the predictions of each site response models. The coefficient compares the observed and predicted ratio of surface to downhole amplification Fourier amplitude spectra (FA). The procedure used herein was based on [67] and [7]. It consists in selecting 200 logarithmically spaced frequencies between the first and fourth peak of the site's linear 1D transfer function. If the fourth peak is located at a higher frequency than 20 Hz, the frequencies above this value are excluded. The amplitude ratio spectra were smoothed using the Konno-Ohmachi smoothing function [125] with a band width of $b = 30$. Pearson's coefficients vary from -1 to 1, where $r = 0$ indicates that there is no correlation in the data. In addition to the FA, the Pearson's correlation are computed by comparing the observed and predicted surface pseudo-acceleration response spectra (PSA).

The computed coefficients were grouped by site response model and by classification factor, such as the shear strain index (I_γ), site, and computed pore pressure ratio, to evaluate

any potential bias from the method of analysis. The shear strain index I_γ was originally proposed by [126] and is defined as the ratio of the input peak ground velocity (PGV) to V_{S30} as described in Eq. 5.4.

$$I_\gamma = \frac{PGV}{V_{S30}} \tag{5.4}$$

This ratio was used to represent the expected level of nonlinearity rather than the computed shear strains, because it can be defined prior to the analyses, and because it was shown in Fig. 5.1f that shear strains are largely influenced by the degradation occurring due to liquefaction for the effective stress analyses.

5.5.1 Level of nonlinearity

The Pearson's r coefficients are computed from the FA spectrums and are separated based on the shear strain index (I_γ) originally proposed by [126]. The computed coefficients are presented in Fig. 5.9 for the motions less affected by dilatation pulses in their acceleration time histories (scenario scenario 1) and are categorized based on the shear strain index I_γ. The number of motions that were considered in each class are identified in the legend. Note that for the effective stress results, the response is averaged from the calibrations that were applied at all sites, as discussed in Section 5.4.

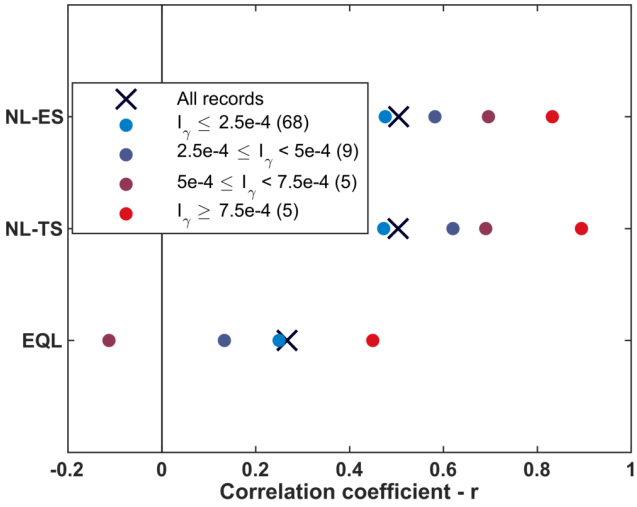


Figure 5.9 Correlation coefficients between the observed and predicted amplification spectra for EQL, NL-TS and NL-ES analyses as a function of the shear strain ratio I_γ computed from the Fourier Amplitude Ratio.

These findings highlight the benefits of more advanced nonlinear models in opposition to commonly used equivalent-linear models. For the EQL analysis, a trend of decreasing accu-

racy with increasing levels of nonlinearities was revealed with computed coefficients smaller than 0.2. For the NL analyses, the highest r coefficients are obtained for $I_\gamma > 7.5\text{e-}4$, or when the behavior is highly nonlinear. These results are in accordance to [7], which reported that the highest r coefficients were obtained at large computed strain levels ($\gamma_{max} > 0.5\%$). This excludes the EQL coefficients which were found to be much lower in the current study compared to these values, particularly for 5e-4$\leq I_\gamma <$7.5e-4. The negative coefficients computed could be interpreted as being a result of the fact that the soils considered in this study are soft and liquefiable. Therefore, these yield high levels of nonlinearities which are hard to capture by the equivalent-linear models when considering only the Fourier spectra. Overall, the NL-TS and NL-ES offer similar accuracy for all levels of nonlinearities. Yet, the computed coefficients for NL-ES exhibit a slight difference for $I_\gamma \geq 7.5\text{e-}4$, suggesting that the NL-TS model is more appropriate for high strain levels. Note that these motions are not always associated with complete liquefaction. Amongst the plausible explanations for this finding, is the overestimation of soil softening related to high pore pressure generation, as previously noted in Fig. 5.1. This would be attributed to the tendency of the models to wrongly predict liquefaction for high strain motions, and will be discussed in more detail in Section 5.6.

The results presented in Fig. 5.9 showed the average error by incorporating a classification based on the nonlinearity levels. Considering that 87 motions were included in these figures, the results could potentially be influenced by the separation scheme. For instance, for the $I_\gamma > 5\text{e-}4$ classes, only 5 motions were considered. Therefore, in order to remove this uncertainty, the r coefficients were computed for each ground motion. Results are presented in Fig. 5.10 as a function of I_γ, and a weighted regression line approximated by a loess function is added to evaluate the trends in the data.

Similarly to Fig. 5.9, the results from NL analyses show a slight tendency of increasing accuracy with increasing I_γ, with a slight decrease for NL-ES at $I_\gamma > 10\text{e-}4$, when comparing to NL-TS analyses results. At these levels, effective stress results are slightly less precise than total stress, as was previously observed. For EQL, the trend is mostly constant until $I_\gamma =$ 3e-4, where negative values are obtained. Thus, this indicates a negative correlation between the predicted and observed amplification spectra which further supports the limitations of using the EQL approach over the NL models. Regarding the coefficients computed from the PSA, the average precision appears to remain constant through all strain levels for the different models.

The Pearson's correlation coefficients are computed for all the 98 motions considered in this study. The motions from the centrifuge tests are isolated from the downhole array sites, and

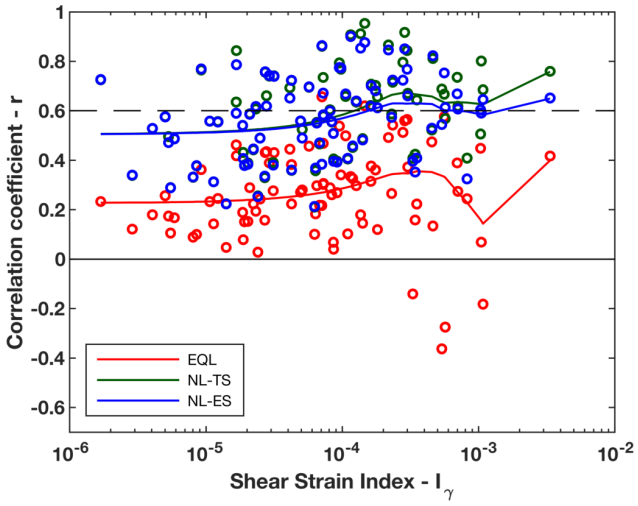


Figure 5.10 Correlation coefficients between the observed and predicted amplification spectra for EQL, NL-TS and NL-ES analyses as a function of the shear strain ratio I_γ for each event computed from the Fourier Amplitude Ratio

are presented in Fig. 5.11 as a function of the shear strain index. Note that only the results from the effective stress analyses, by averaging the response from all models, are presented.

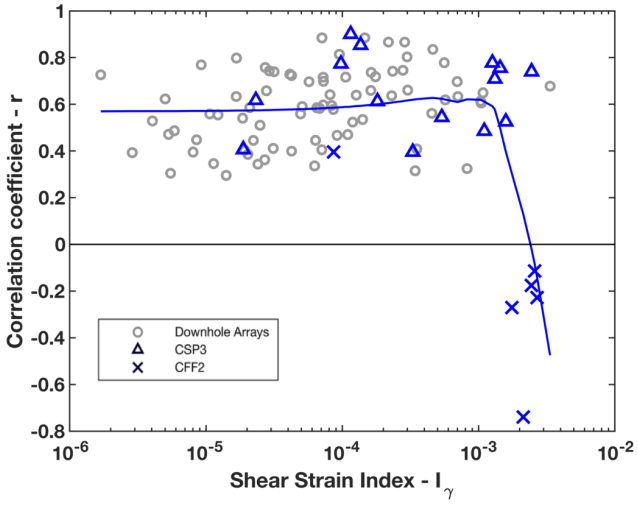


Figure 5.11 Correlation coefficients between the observed and predicted amplification spectra for NL-ES analysis as a function of the shear strain ratio I_γ for each event computed from the Fourier amplitude ratio for the centrifuge tests.

The results reveal that significantly less precision is obtained for the high strain motions that are the most influenced by high-amplitude high-frequency pulses in the centrifuge tests, corresponding to the motions that are associated with high pore pressure generation, strain

softening, and dilatation. However, note that the motions from the other downhole array sites appears to be well captured for these conditions, as mentioned before. The high strain motions of centrifuge test CFF2 are the only ones that present significantly less precision. Therefore, the results presented herein further supports the limitation of the current models in capturing dilative behavior, thus confirming the findings of [58] previously discussed.

5.5.2 Site

In order to evaluate the influence of individual sites on the accuracy of the predictions, the coefficients r are computed for each site and analysis for all motions, and are presented in 5.12.

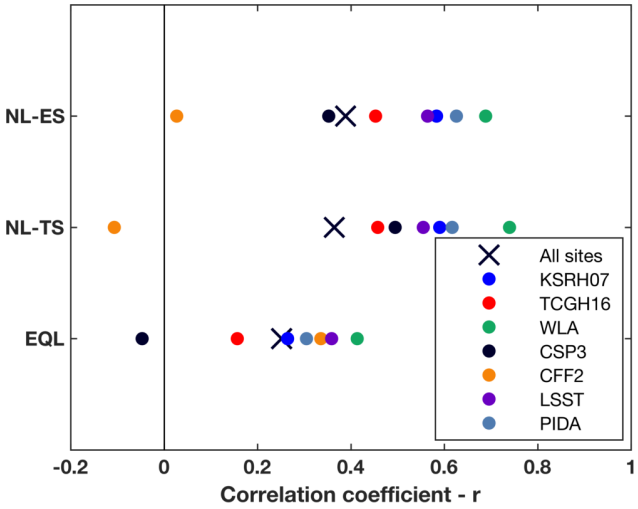


Figure 5.12 Correlation coefficients between the observed and predicted amplification spectra for EQL, NL-TS and NL-ES analyses binned by sites.

The results reveal that a large variability is associated with the individual sites within each model. In fact, the r coefficients for the NL-TS analysis vary from -0.11 for site CFF2 to 0.71 for site WLA. In general, these results appear to be mostly consistent with the procedure applied in Section 5.3 that was used to verify the validation of 1D assumptions at each site. Also, with respect to [67]'s classification, where site KSRH07 is classified as LG and site TCGH16 as LP, the results presented herein reveal that site KSRH07 has higher precision with $r = 0.59$ and site TCGH16 has $r = 0.42$ for the NL-TS analysis, corroborating the findings of [67]. When considering all motions, the computed coefficients for centrifuge test CSP3 is $r = 0.50$ and for CFF2 is $r =$ -0.11. Removing the motions that are associated with observed dilatation yields r coefficients of 0.57 and 0.40, respectively, showing an improvement in the accuracy of the analyses, particularly for site CFF2, as discussed earlier.

5.5.3 Pore pressure ratio

In the following section, the r coefficients were computed with a separation in the computed pore pressure ratio for the effective stress analysis for both scenarios identified in Table 5.1. The results are presented in Fig. 5.13 for the different pore pressure generation models considered.

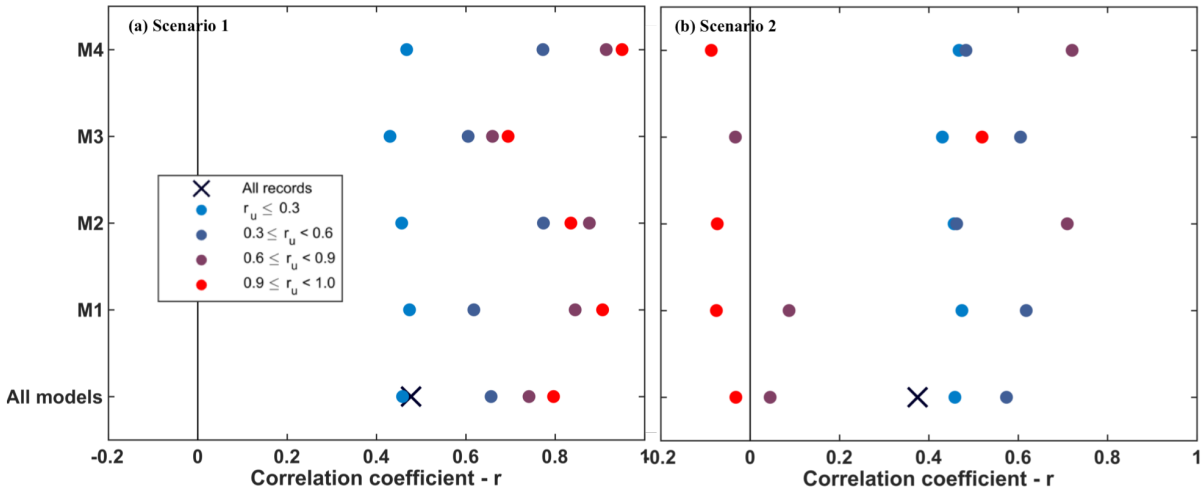


Figure 5.13 Comparison of correlation coefficients between the observed and predicted spectra for NL-ES analysis (M1, M2, M3, M4) based on the estimated pore pressure ratio r_u

For the first scenario showed in Fig. 5.13a, for all models, the results show that the best accuracy is obtained for motions when $r_u > 0.9$ is predicted and liquefaction is assumed to have occurred. For $r_u > 0.9$, all computed ratios are higher than 0.6, with the exception of M3, which was defined earlier as representing a good correlation between the observed and the predicted transfer functions. For lower levels of pore pressure buildup, the computed r coefficients decrease, revealing a lower precision. This follows the tendencies presented in Fig. 5.10 which showed that higher nonlinearity levels, thus showing a potential for pore water pressure generation, yield higher correlation coefficients. Regarding the comparison between the individual models, most of them follow similar tendencies. In general, similar precision is obtained for $r_u < 0.6$ for all models, except for M3, and the highest improvement in the accuracy for $0.6 < r_u < 0.9$ is made with the predictions of models M2 and M4. Including all the motions in Fig. 5.13b decreases the precision of the analyses for all classes with $r_u > 0.3$ compared with Fig. 5.13a, where the most significant decrease is observed for $r_u > 0.9$. The precision of M2 and M4, which are both energy-based, are the highest for class $0.6 < r_u < 0.9$ and of model M3 for class $r_u > 0.9$. In general, model M3 appear to show a slight decrease in the precision compared to the other models.

5.5.4 Comparison of the calibrations of the effective stress models

In this section, the Pearson's r correlation coefficients are computed for each calibration of the effective stress models to compare the observed and predicted ratio of surface to downhole amplification FA. The coefficients are compared in terms of levels of nonlinearity represented by the shear strain index I_γ, defined in Equation 5.4. The results are evaluated for both scenarios identified in Table 5.1.

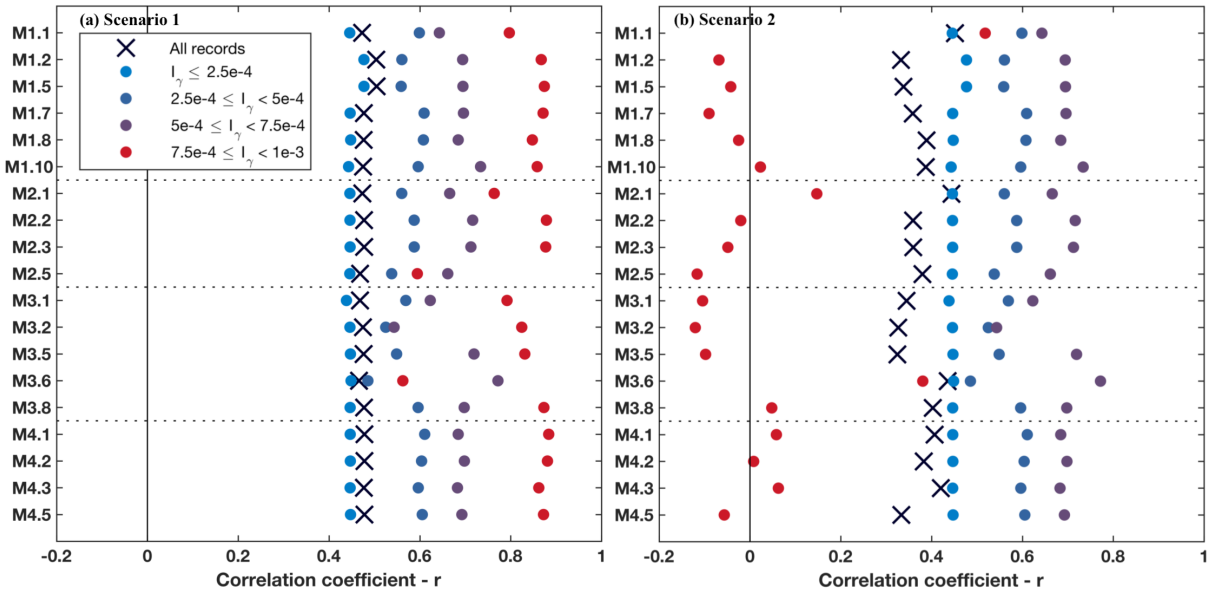


Figure 5.14 Correlation coefficients between the observed and predicted amplification spectra for the individual calibrations of NL-ES analyses binned by the shear strain ratio I_γ.

For Fig. 5.14a, most of the models have similar accuracy across all levels of nonlinearities. This comparison allows the identification of the calibrations that tend to diverge from the others, which occurs for the high-strain nonlinear motions. Specifically, for models M1 and M2, the calibration M1.1 (with $\gamma_{tvp} = 0.01\%$), M2.1, M2.5, and M3.6 leads to a decrease in the accuracy over the other calibrations within the same model for $I_\gamma \geq$ 7.5e-4. This suggests that $\gamma_{tvp} = 0.01\%$ is too low which involves higher pore pressures generation and leads to slightly less precision. Finally, for M4, the precision of the predictions remains constant across all the calibrations and the classes of nonlinearities. The inclusion of all motions in Fig. 5.14b, results in the significant decrease of the r coefficients for class $I_\gamma \geq$ 7.5e-4 for all calibrations, supporting previous findings. Although, the decrease in precision for calibrations M1.1 and M3.6 is less important.

5.6 Pore pressure response of the considered models

5.6.1 Maximum shear strain

This section compares the predicted behavior of the liquefiable layers by the effective models during ground response analyses, with the expected behavior of liquefiable soils as reported in the literature. As mentioned in Section 2.4, previous studies have found that pore pressure buildup is related to shear strains rather than shear stresses. For instance, [127], [31], and [48] compiled databases and proposed lower and upper boundaries of the relation between the pore water pressure ratio and shear strain based on the results of laboratory testing. The [127] correlation is based on the results of stress-controlled testing where r_u were measured after the first loading cycle (N) of shear strain. In opposition, [31], and [48] uses data from strain-controlled triaxial tests where r_u corresponds to $N = 10$. Thus, since the two datasets are subjected to different stress paths, a careful analysis must be exercised when establishing a comparison between the correlations. In Fig. 5.15, the correlations are plotted with the results from all sites and ground motions for the following models: Dobry and Matasovic (M1), GMP (M2), Park and Anh (M3) and Generalized (M4). Only one calibration for each model is considered herein, corresponding to the initial calibration of the pore pressure generation models with a degradation parameter $v = 1$. The predicted response is extracted at several depths within the liquefiable layers at each site. For [127], the mean and mean $\pm$ one standard deviation (σ of the correlation are plotted in the figures. The median values of $D_R = 63\%$ and $\sigma_{vo}^{'} = 99$ kPa of the samples in the database used by the authors were selected [127]. Moreover, in order to account for the differences between the stress paths, a color scheme is adopted to represent the number of equivalent loading cycles (N_{eq}) computed for a reference acceleration of $0.65 \times PGA$ following the procedure described in [111].

The results from Fig. 5.15 indicate that the predictions of the calibrations M1.1 and M3.1 are centered around the lower boundary and upper boundary of [31] and [48] relationship, respectively. For M2.1 and M4.1, which are both energy-based, most of the data is located in between [31] and [48] and [127]. Thus, in general, the results reveal that the computed behavior appears to be consistent with the reference relationships. However, a few data points are located outside of the boundaries of the correlations. For $r_u > 0.9$, this is likely due to the overprediction of liquefaction and the tendency of shear strains to reach unrealistic high values, as illustrated in Fig. 5.1. For lower levels, these inaccuracies might be associated with instabilities in the shear-strain shear-stress cycles predicted by the mathematical forms of the models. Furthermore, the volumetric threshold shear strain γ_{tvp}, generally taken as 0.01% for sands [31], represents a value below which studies have proven that no pore pressure

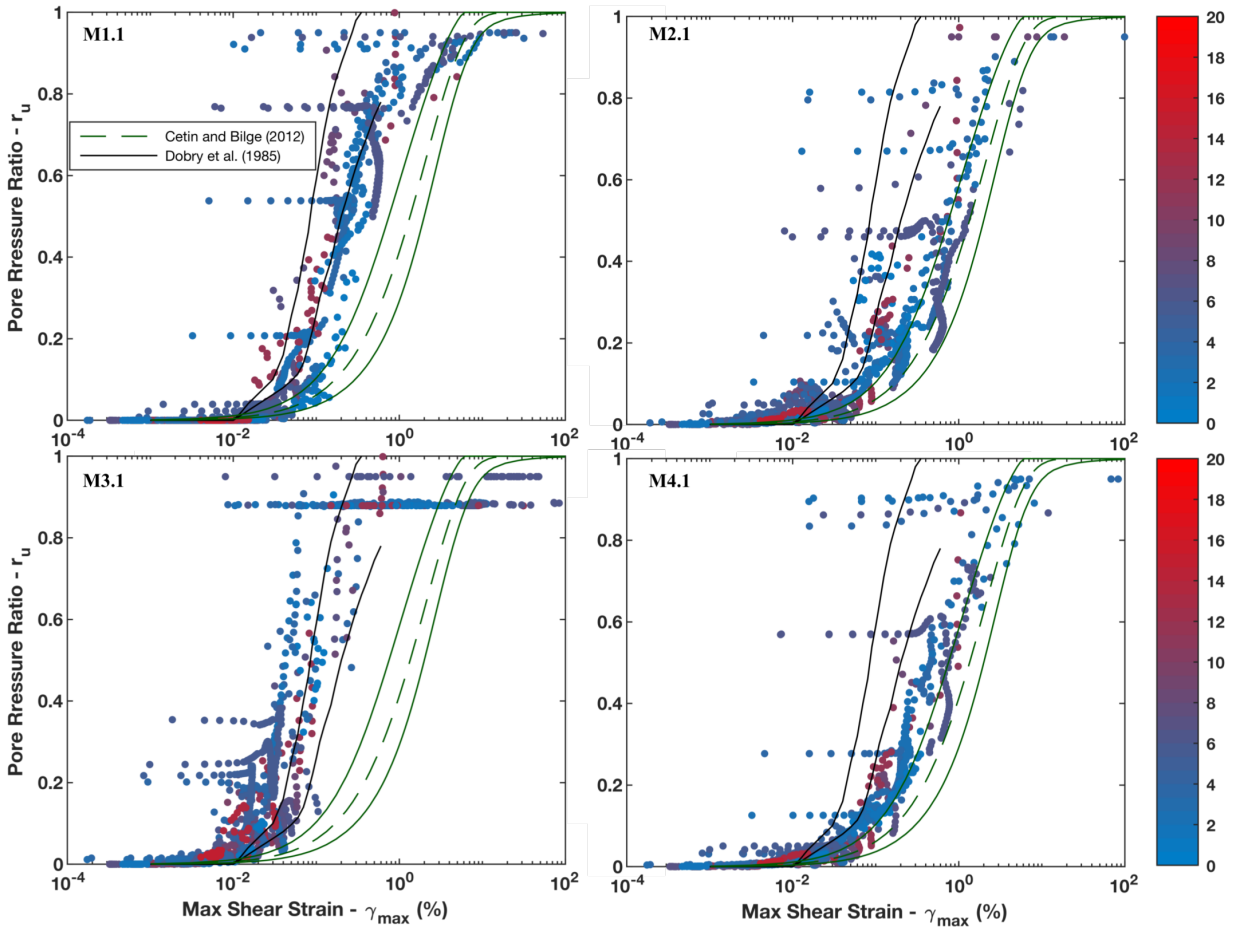


Figure 5.15 Pore pressure response versus the maximum computed shear strains in effective stress analysis for calibrations M1.1, M2.1, M3.1 and M4.1.

generation is generated. The four models considered here show a generation of excess pore pressures for shear strains lower than γ_{tvp}. Interestingly, M1 also exhibits this tendency, even though γ_{tvp} was specified directly as an input parameter in the model, and defined as 0.01%. As will be observed in a subsequent section and presented in Fig. 5.17, this may be related to the fact that some of the individual calibrations are behaving singularly and are showing transient decreases or increases in the pore pressure response as a function of time. Considering that the models only allow the accumulation of pore pressure buildup and strains, this could explains why some values are observed for strains lower than γ_{tvp}. In addition, Fig. 5.15 shows no correlation between N_{eq} and r_u, since the highest values of N_{eq} do not directly yield the highest pore pressure buildup levels. Therefore, other factors must influence the development of the pore pressures.

Similarly, the predictions of the other calibrations were studied for each model. For the Park

and Anh (M3) model, most of the data points in Fig. 5.15 were located outside the upper boundary of [48] . The results from calibration M3.6, are presented in Fig. 5.16.

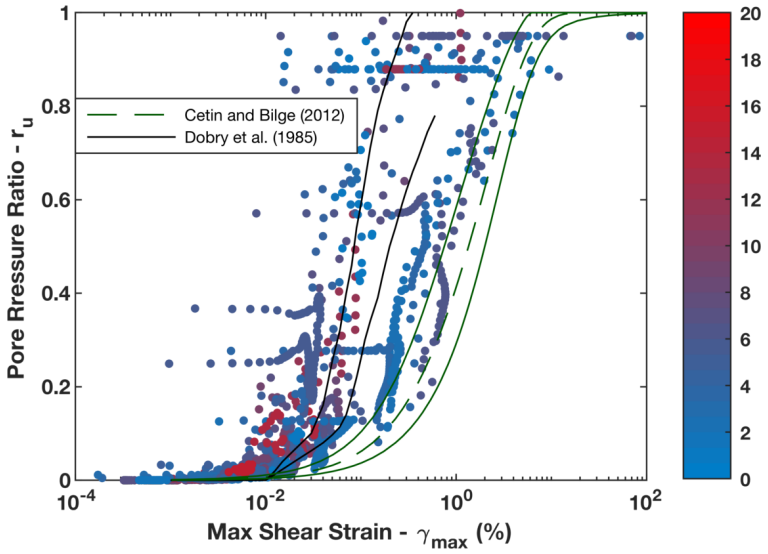


Figure 5.16 Pore pressure response vs the maximum computed shear strain for the Park and Ahn model calibration M3.6.

The results from calibration M3.6 show that the results are more dispersed and are shifted towards the [127] correlation. The difference between this calibration and M3.1, is that the value of the degradation parameter v is taken as 5 rather than 1. Thus, the shift is explained as higher strength degradation is associated with larger shear strains. However, results presented in Fig. 5.15 showed that the precision was decreased for highly nonlinear motions. However, no other calibrations with using $v = 2.5$ or 5 (M1.2, M1.7, M2.3, M2.5, M3.5, M4.3, and M4.6) showed a significant difference than with $v = 1$. Finally, the predictions of the other calibrations were mostly consistent with Fig. 5.15, except for M1.5 (F from [106]) and M4.5 ($\beta = 1.4$), presented in Fig. S2 and Fig. S3 in Appendix A, which revealed a slight shift towards the [127] calibration.

5.6.2 Time

in this section, the pore pressure response is investigated as a function of time. The motion EQ7 ($M_w = 6.9$ & $PGA_{obs-surf} = 0.74$ g) recorded for the centrifuge test CSP3 was used herein. The computed response is compared in Fig. 5.17 with the observed response measured by pore pressure transducers #52 and 55, located at depths 1.1 and 6.82 m, respectively. The instruments are located in a medium dense layer of Nevada sand. Note that the results of each effective stress calibration are presented with the exception of the calibrations that predicted

similar results to the ones presented herein (i.e. M3.3, M3.4, M3.5, M4.2, and M4.3), that are omitted for clarity.

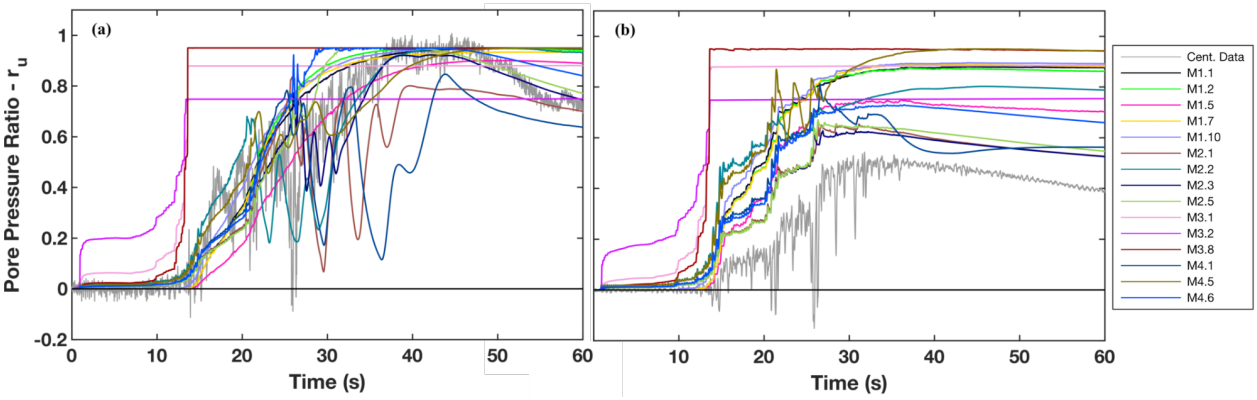


Figure 5.17 Predicted and observed pore pressure response as a function of time – Site CSP3: (a) PPT52 – 1.1m, (b) PPT55 – 6.82 m.

For the shallow layer in Fig. 5.17a, the results show that most models predict liquefaction or levels of pore pressure buildup higher than 0.8. The predictions of the Park & Ahn model (M3) exhibit a rapid offset of pore pressure generation shortly after the beginning of the motion which reaches liquefaction more rapidly than what was observed. The responses of M2.1, M2.2, M2.6, and M4.1, show an unrealistic variation in the response with rapid successive increases and decreases of pore pressures, which highlights the inability of the models of properly considering dilatation. Regarding the results presented in Fig. 5.17b, all models overestimate the pore pressure buildup that occurred. In particular, all calibrations from the model M3 and calibration M4.5 predict the complete liquefaction of the deposit. In addition, some calibrations, such as M2.1, M2.3, M2.5, and M4.6, reproduce a similar rate of generation and dissipation of the pore pressures compared to what was observed, despite having larger amplitudes. Finally, the results illustrate the inability of the models to capture the observed dilation spikes. In general, these observations were found to be consistent across other sites where pore pressure transducers were installed.

5.7 Ground motion parameters comparison

In this section, the performance of each model is evaluated in terms of the following commonly used ground motion parameters: the Arias intensity (AI), significant duration (D_{5-95} and D_{25-75}), number of equivalent loading cycles (N_{eq}), Cumulative Absolute Velocity (CAV), Standardized Cumulative Absolute Velocity (CAV_{STD}), Shaking intensity Rate (SIR) and characteristic periods (T_m, T_o and T_p as defined in [128]). Conventional parameters, such as PGA or PGV, are representative of the ground motion maximum amplitude, while the parameters identified above are considered more reliable since they are found to be influenced simultaneously by the amplitude, frequency content and duration of the motion [37]. Considering their widespread application in various engineering design procedures [129–135] and analyses, their assessment resulting from ground response analyses is important but has not been widely investigated to date.

In the following, the aforementioned parameters were computed from the surface acceleration time series obtained from the analyses and compared with the measured parameters. The comparison was established between EQL, NL-TS, and the average of NL-ES models, and finally between the individual calibrations of the NL-ES analysis. Note that for all subsequent analyses only the calibrations that were considered for all sites were included for the effective stress analysis, as described in the previous sections. The results are analyzed for both scenarios identified in Table 5.1. First, the results are presented for Scenario 1, when the motions from the centrifuge tests where dilatation spikes were identified in the acceleration time histories are omitted, as identified in Table 5.1 and discussed in Section 5.2. Then, Scenario 2, regrouping all 98 motions, is considered. In the following, the computed residuals are first compared individually against the shear strain index I_γ [126] to identify any potential bias. Then, all the ground motion parameters are compared against other parameters such as PGA and PGV of the downhole motion and the PSA at periods $T = 0.1$ and 1 s. Finally, the prediction of each ground motion parameters are compared against each other and conclusions are drawn.

5.7.1 Arias intensity - AI

The Arias intensity (AI) represents the cumulative energy as a function of time and is calculated by the following equation proposed by [136]:

$$AI = \frac{\pi}{2g} \int_0^{t_{max}} a(t)^2 dt \tag{5.5}$$

where $a(t)$ is the acceleration at time t, t_{max} is the duration of the earthquake and g is the gravitational acceleration. Based on this definition, AI is a representation of high frequency ground motions considering that the high acceleration amplitudes are squared [137]. When both orthogonal components of the motion are available, AI is computed as the sum of the Arias Intensities computed for the individual NS and EW components. Also, note that AI was computed for the main shock only when two motions were recorded in the same input motion.

The use of AI has been reported in several studies on the assessment of liquefaction [138, 139], seismic slope stability [140] and structural response [141]. [142] used this parameter to investigate the performance of the nonlinear ground response analysis code SPECTRA and equivalent-linear code SHAKE for motions EQ9 ($M_w = 6.2$) and EQ16 ($M_w = 7.0$) recorded at the LSST site (e.g. LSST12 and LSST16) and found that both codes underpredicted AI. [143] compared the predicted AI from EQL and NL ground response analyses using Deepsoil v5 with measurements obtained from centrifuge experiments for 6 large motions with $M_w > 6.7$ and $PGA > 0.33$ g. They found a tendency towards their over-prediction and a higher bias for the EQL analysis with average residuals for the motions ranging from -0.109 to -0.515 and -0.035 to -0.14 for the NL analysis. More recently, [14] conducted total stress linear, equivalent linear and nonlinear analyses at 114 Kik-net sites and investigated the predictions against AI. They reported that all models under-predicted AI for $\gamma_{max} < 0.007\%$ and over-predicted AI at higher strains.

The results of the present dataset were analyzed in terms of the Arias intensity residuals between the observed and computed surface motion for the EQL, NL-TS and NL-ES analyses and are presented as a function of the shear strain index I_γ in Fig. 5.18. For the motions with records of both orthogonal components, AI was evaluated for the component associated with the maximum acceleration.

The results indicate that both NL-TS and NL-ES over-predict AI for all shear strain levels with residuals ranging from -1.85 to 1.08 and Arias intensities varying from 6.70e-5 to 24.51 m/s with a standard deviation of 2.81 m/s for the NL-TS analysis. The predicted values of the dataset for EQL, NL-TS, and NL-ES analyses are summarized in Table 5.3 (described by the min, max, standard deviation, average) for each ground motion parameter and are compared against the observed data for Scenario 1. The maximum error was found to be associated with a low-amplitude motion with a predicted value of 0.03 m/s compared to 4.80e-3 m/s for the observed motion. Thus, the logarithmic formulation and small values explains the amplitude of these residuals. In general, the results from NL-TS and NL-ES provide similar accuracy with a slight decrease in the precision for NL-TS for $I_\gamma > 7e\text{-}4$.

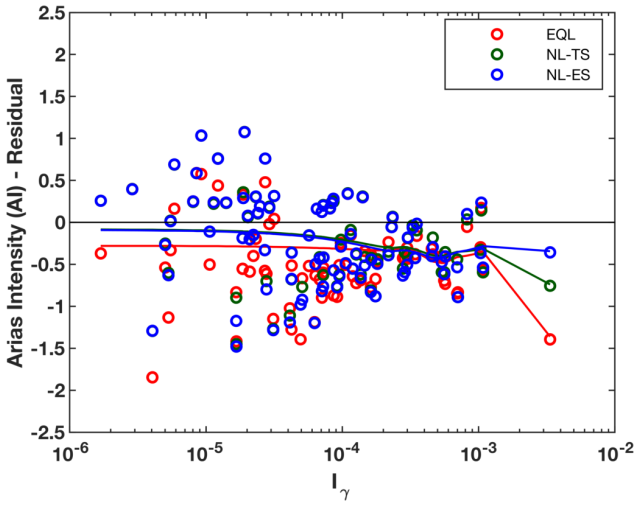


Figure 5.18 Arias intensity residuals as a function of the shear strain index I_γ for EQL, NL-TS, and NL-ES.

For the EQL analysis, the bias is slightly higher than the NL analyses and indicates the over-prediction of AI. Overall, both the decreased precision for the EQL analysis and the amplitude of the average residuals were found to be in good agreement with the findings of [143]. Besides, these findings follow similar tendencies reported by [14], even though this study established the comparisons in terms of the maximum computed shear strain, it is hypothesized that using I_γ would yield equivalent conclusions.

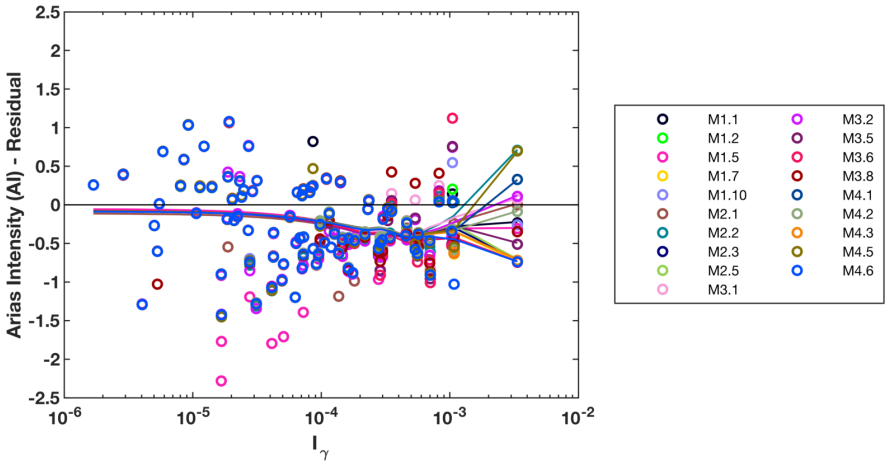


Figure 5.19 Arias intensity (AI) residuals as a function of the shear strain index I_γ for the NL-ES calibrations.

The evaluation of AI between the calibrations of the effective stress models are then compared and are presented in Fig. 5.19. The results show that the predictions of each calibration are

similar until approximately I_γ = 3e-4, or until a highly nonlinear response is observed. At higher shear strain ratios, the results yield larger uncertainty with the residuals from each calibration being more dispersed. At these ratios, the motions are more nonlinear and have a higher probability of liquefaction. Thus, these findings highlight the large variability resulting from the selection of the input parameters for potentially liquefiable soils and illustrate the influence it may have on the computed results. For instance some of the calibrations slightly over-predict AI at low strains, and largely over-predict AI at higher strains, a trend somewhat similar to the findings reported in [14], while others underpredict AI at higher strains.

5.7.2 Significant durations - D_{5-95} and D_{25-75}

As presented in Section 2.4, strength degradation and pore pressure generation are dependent on the number of loading cycles N [144]. A higher number of loading cycles is also characteristic of a motion with a longer duration. Thus, the duration is a useful parameter to evaluate the potential for earthquake damages [145–147] and represent the characteristics of the ground motions [37]. Some parameters have been proposed to represent the duration, including the uniform duration, bracketed duration [148] and significant duration [149]. In this study, the significant duration D_{5-95} and D_{25-75} was were selected, since these parameters are the most commonly used in practice and represents the entire acceleration time series, as opposed to other duration parameters. These parameters are defined as the time interval between 5% and 95% and 25% and 75%, respectively, of the total Arias intensity, and thus represents the time period where a ground motion record contains most of its energy. The residuals for both significant duration metrics are presented in Fig. 5.20 as a function of the shear strain index I_γ for each analysis.

On average, the findings show that all models over-predict D_{5-95} with the residuals ranging from -1.76 to 0.86, corresponding to a maximum error of 54.66 s compared to 9.43 s. This trend remains constant across all levels of nonlinearities for the NL models. For the EQL analysis, the tendency slightly diverges for $I_\gamma >$ 1e-4 and follows an upward slope, which suggests that higher precision is obtained for the higher amplitude motions. For D_{25-75}, the residuals appear to be more dispersed, ranging from -2.27 to 1.79 (maximum error of 15.9 s). This results in slightly higher average residuals at low shear strains compared to parameter D_{5-95}.

Again the residuals are compared for each calibration of the effective stress models and are presented in Fig. 5.21 for D_{5-95}.

Analogous to AI, the determination of D_{5-95} is influenced by the selection of the input parameters and reveals that a larger variability is obtained at higher I_γ. However, the

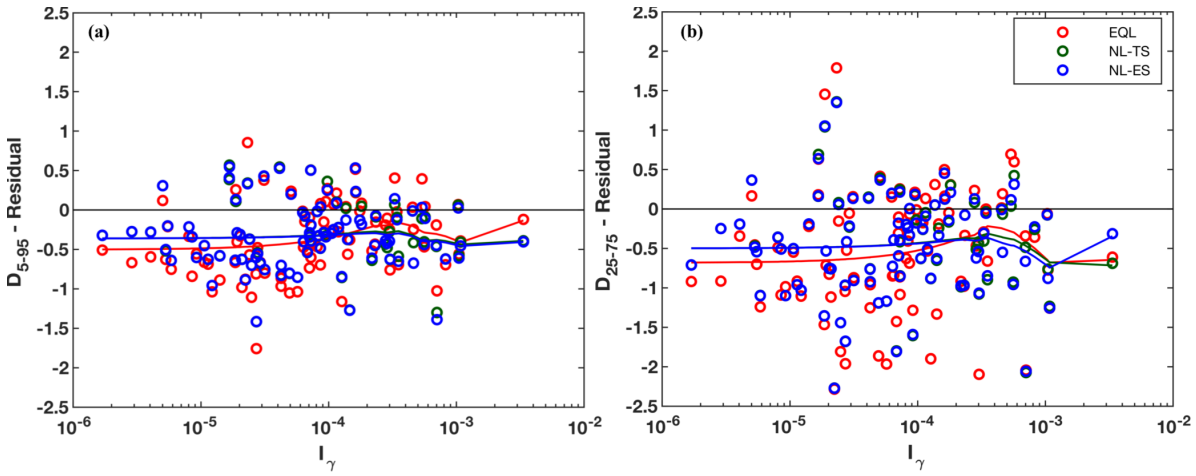


Figure 5.20 Significant duration D_{5-95} and D_{25-75} residuals as a function of the observed downhole shear strain index I_γ for EQL, NL-TS, and NL-ES analyses.

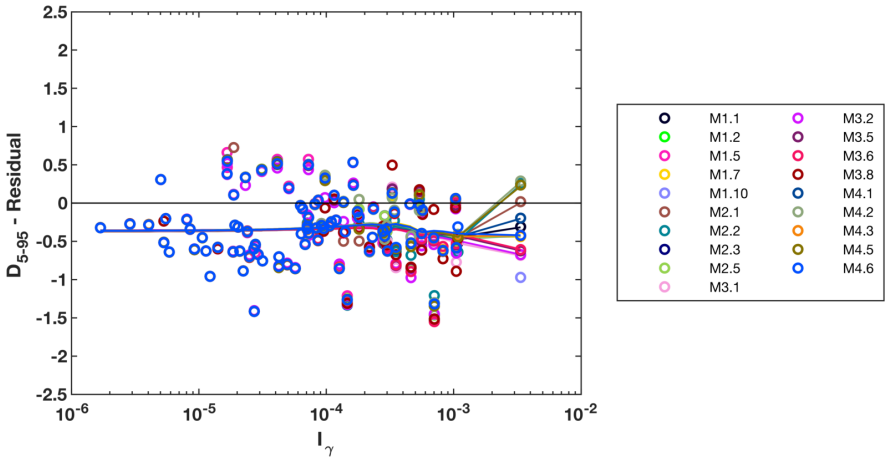


Figure 5.21 Significant duration D_{5-95} residuals as a function of the observed downhole shear strain index I_γ for NL-ES analysis per calibration.

residuals are less dispersed for the nonlinear motions than what was found for AI, with values ranging from -1.60 to 1.20.

5.7.3 Number of equivalent loading cycles - N_{eq}

As mentioned in Section 2, the number of equivalent loading cycles is a parameter of interest when assessing the potential for pore pressure generation and liquefaction. It is included in a few of the effective stress models and degradation formulations presented in Section 2, and many liquefaction procedures and studies have highlighted its role in the evaluation of liquefaction [16]. In the following, the number of equivalent loading cycles (N_{eq}) was computed

based on the procedure described in [111] for a reference acceleration of $0.65 \times PGA_{surf}$. In

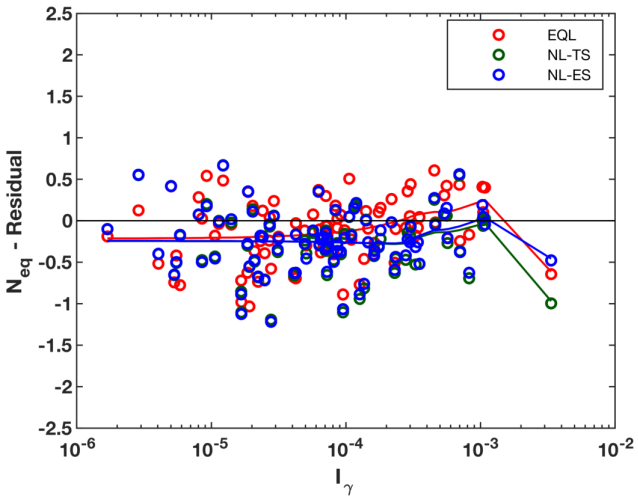


Figure 5.22 Number of equivalent loading cycles N_{eq} residuals as a function of the observed downhole shear strain index I_γ for EQL, NL-TS, and NL-ES analyses.

general, most models follow a tendency of over-predicting this parameter for low levels of nonlinearities. At higher I_γ, the residuals from the EQL analysis exhibit an upward slope and positive residuals indicating the under-prediction of this parameter compared to what was observed. For the NL-TS results, the slope at high strain levels is slightly increased compared to the NL-ES results. Overall, shows that N is reasonably captured when comparing against the other parameters included in this study with residuals ranging from -1.19 to 0.67. For the highest residual, the predicted $N_{eq} = 10.96$ compared to 3.33 cycles. In Fig. 5.23 are presented the difference between the calibrations of the NL-ES models. A similar trend of increasing variability at higher strain levels is observed.

5.7.4 Cumulative absolute velocity - CAV & CAV_{STD}

The Cumulative Absolute Velocity is defined by the following equation [150].

$$CAV = \int_0^{t_{max}} |a(t)|dt \tag{5.6}$$

[151] then proposed the standardized cumulative absolute velocity (CAV_{STD}) [152]. This was developed to limit the influence of low-amplitude ground motion amplitudes that can occur before and after the main part of shaking in order to represent only the strong motion shaking portion of the record. Therefore, the formulation of this parameter proposed to integrate the absolute acceleration time history by limiting its evaluation to 1 second time

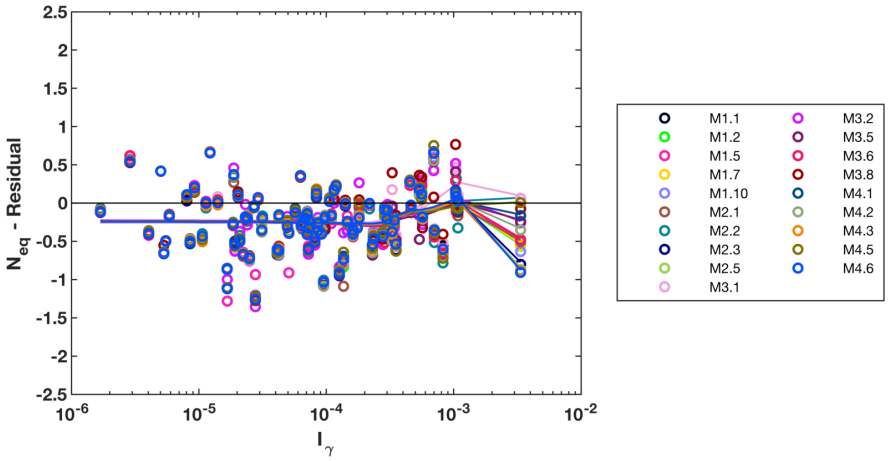


Figure 5.23 Number of equivalent loading cycles N_{eq} residuals as a function of the observed downhole shear strain index I_γ for NL-ES analysis per calibration.

windows that have a peak ground amplitude (PGA_i) of at least 0.025 g.

$$CAV_{STD} = \sum (H(PGA_i - 0.025) \int_{t=t_i}^{t_{i+1}} |a(t)|dt \tag{5.7}$$

where N is the number of discrete 1 second time window, t_i is the start of the time window i, and $H(x)$ is he Heaviside Step function defined below:

$$H(x) = \begin{cases} 0 & \text{for } x < 0 \\ 1 & \text{for } x \geq 1 \end{cases} \tag{5.8}$$

Based on these definition, CAV_{STD} is always smaller or equal to CAV. The highest differences between the two parameters are expected to occur for long duration and small amplitudes earthquakes.

These two parameters are typically used to evaluate the damage potential of earthquakes to building [153]. For instance, these are used by the U.S. Nuclear Regulatory Commission (USNRC) has defined CAV and CAV_{STD} thresholds at which it becomes necessary to shut down nuclear powerplants for inspection. [154] developed a multi-level criterion to define these limits based on the response spectrum (PSA and PSV) and CAV. Threshold limits of 0.30 and 0.16 g-s, for CAV and CAV_{STD} respectively, have been recommended by [150] and [151]. [153] determined that using CAV as a proxy for induced damage, generally leads to a smaller uncertainty than the use of other conventional intensity measures. It was also concluded that including the CAV criterion may lead to the avoidance of unnecessary plant

shutdown, particularly in the case of nearby small-magnitude earthquakes of distance large-magnitude earthquakes, that may otherwise exceed response spectrum criterion [153]. [155] and [156] conducted a parametric study to evaluate the performance of 23 different intensity measures (IM) in predicting pore pressure generation and permanent building settlements using centrifuge experimental results. The authors concluded that CAV led to the best combination of efficiency, sufficiency and predictability when assessing building settlements. Subsequently, [157] developed rock ground motion prediction equations (GMPEs) for these intensity measures. These were then integrated in a predictive model for building's permanent settlements of shallow-founded structures on liquefiable soils [158] based on parameter CAV.

Fig. 5.24 presents the computed residuals of CAV and CAV_{STD} against I_γ for the EQL, NL-TS and NL-ES analyses. The computed residuals for CAV varied from -1.10 to 0.78 (max. error of 0.83 g-s) and from -1.32 to 2.45 (max. error of 0.014 g-s). In general, the results show a tendency of the over-prediction of parameter CAV for all I_γ, with a slightly higher average residual for the EQL analysis. Overall, the residuals computed for CAV are lower than for AI, which is consistent with the results from previous studies. In opposition, the average residuals for CAV_{STD} are more scattered than with CAV. This was found to occur for observed motions of low-amplitude having few peaks over $a(t) > 0.025\ g$, thus yielding low CAV_{STD} values. Consequently, any slight error from the ground response models leads to amplified residuals considering the computation of the residuals in the logarithmic space. Also these appear to be mostly centered around zero for $I_\gamma <$ 5e-5 for all analyses. This occurs due to the acceleration threshold $a(t) > 0.025\ g$, which is not attained for small amplitude motions. At higher shear strains, negative residuals are obtained suggesting the over-prediction of this parameter.

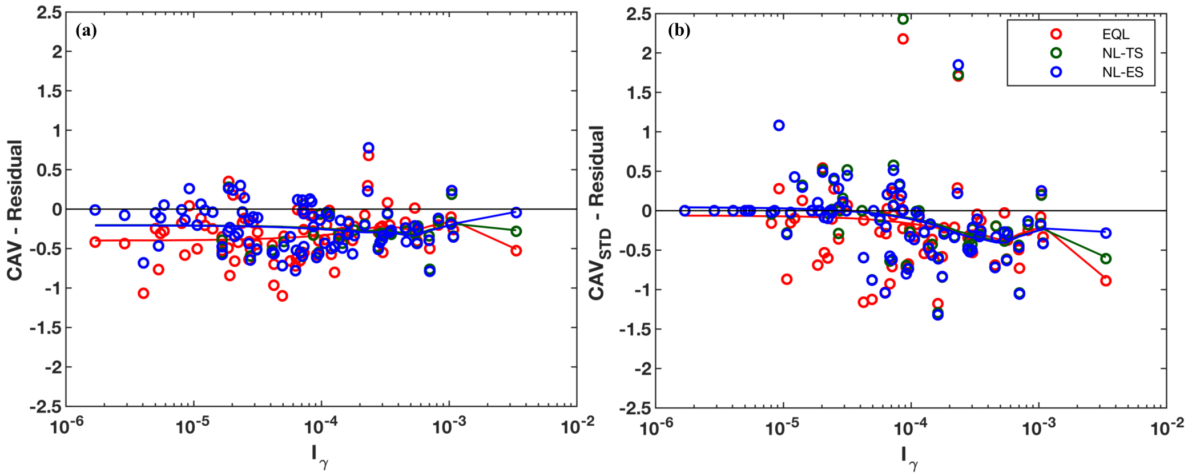


Figure 5.24 Cumulative Absolute Velocity Residuals as a function of the observed downhole shear strain index I_γ for EQL, NL-TS and NL-ES analyses.

In Fig. 5.25 are presented the residuals for the NL-ES analysis per calibration CAV and CAV_{STD}. The results show that the amplitude of the residuals vary from -1 to 0.90 for CAV and -1.39 to 1.96 for CAV_{STD} and again are smaller than what was found for parameter AI. The residuals are generally negative and the results from the different calibrations begin diverging at $I_\gamma >$ 4e-4, with the most variation being observed for the motion with the maximum value of I_γ ($\approx$ 3.5e-5).

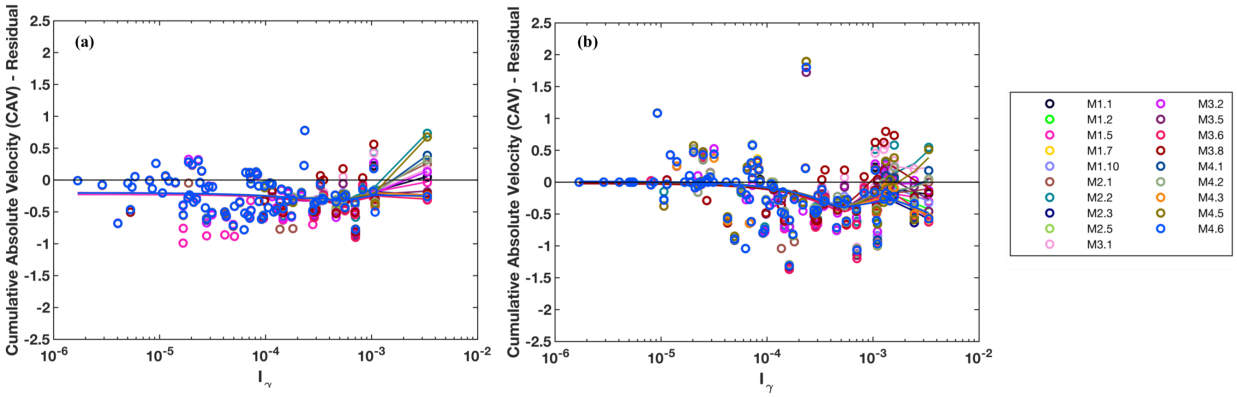


Figure 5.25 Cumulative absolute velocity (a) CAV & (b) CAV_{STD} residuals as a function of the observed downhole shear strain index I_γ for NL-ES analysis per calibration.

5.7.5 Shakin intensity Rate - SIR

The Shaking intensity Rate (SIR) was proposed by [60] and is defined as:

$$SIR = \frac{AI_{5-75}}{D_{5-75}} \tag{5.9}$$

where AI_{5-75} is the variation of AI from 5 to 75 % and D_{5-75} is the associated significant duration.

The SIR is expected to represent the rate of earthquake energy buildup in addition to simultaneously illustrate the excess-pore pressure generation, rate of soil particle disturbance and the seismic demand on structures [60]. In her work, [60] demonstrated that liquefaction-induced building settlements appeared to increase with increasing SIR. Thus, it was suggested that this parameter appears to be a reliable mesure of the evaluation of liquefaction consequences on structures. Amongst, the investigated parameters in their study, [155] and [156] reported that SIR is one of the most accurate parameters in evaluating pore pressure generation in the free-field. The SIR is computed for all types of analyses and the residuals are compared to the shear strain index I_γ in Fig. 5.26.

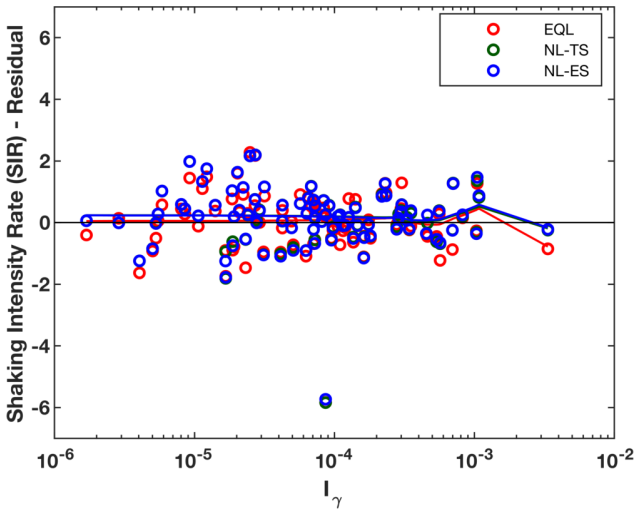


Figure 5.26 Shaking intensity Rate residuals as a function of the observed downhole shear strain index I_γ for EQL, NL-TS and NL-ES analyses.

In general, the results from Fig. 5.26 suggests that NL-TS and NL-ES analyses underestimate SIR compared to what was observed, for all I_γ strain levels. In opposition, the average residuals from the EQL analysis appears to be mostly centered around zero. Compared to all the other parameters included in this study, the amplitude of the residuals, from

-1.80 to 2.30 approximatively, was found to be the highest and suggests that less precision is obtained when evaluating this parameter. A single data point, associated with motion #EQ1 of centrifuge test CFF2 yielded a higher residual of -5.84 (predicted value of 0.27 m/s/s compared to 7e-4 m/s/s). Thus, the error is explained by the small amplitude of the observed SIR. In Fig. 5.27 are presented the comparison of the residuals between the NL-ES calibrations. Again, increased variability is obtained at high strain levels, confirming previous results.

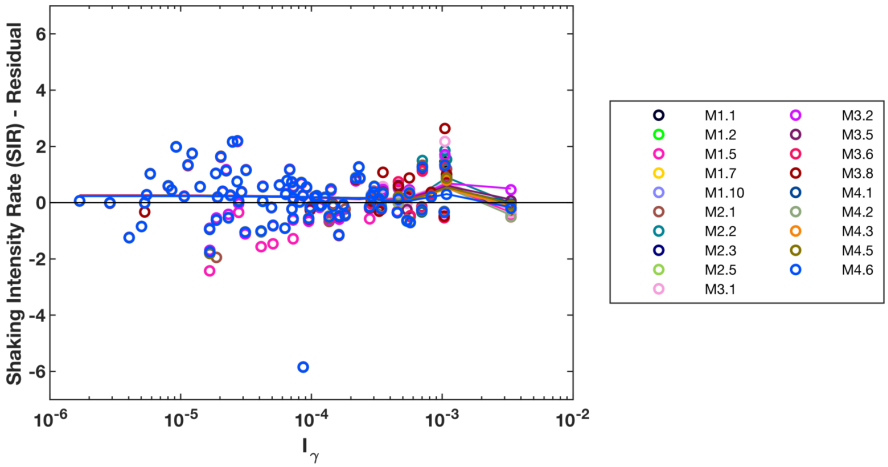


Figure 5.27 Shaking intensity Rate residuals as a function of the observed downhole shear strain index I_γ for NL-ES analysis per calibration.

5.7.6 Frequency content - T_m, T_o, and T_p

Finally, the results from the EQL, NL-TS, and NL-ES are evaluated as a function of the mean period (T_m), the smoothed spectral predominant period (T_o) and the predominant spectral period (T_p) [128]. These parameters are used to characterize the frequency content of the motions and are used in various seismic design procedures [131, 159–161]. As presented previously, other methods also compare the fundamental frequencies of soil profiles with the ground motion's mean period T_m to evaluate potential resonance that may amplify the ground motion characteristics [132, 162]. The following defines each of these parameters and compares their respective performance and application. Note that a complete review of these periods is available in [128] which served as the basis for the following discussion.

First, the mean period (T_m) [162] is determined based on the Fourier Amplitude Spectrum (FAS) and is defined by the following equation.

$$T_m = \frac{\sum_i C_i^2 \left(\frac{1}{f_i}\right)}{\sum_i C_i^2} \tag{5.10}$$

where C_i are the discrete Fourier amplitude coefficients and f_i are the associated discrete Fourier transform frequencies between 0.25 and 20 Hz. Similarly, the smoothed spectral predominant period (T_o) is determined from the 5%-damped acceleration response spectrum expressed by Equation 5.11.

$$T_o = \frac{\sum_i T_i \cdot ln\left(\frac{S_a(T_i)}{PGA}\right)}{\sum_i ln\left(\frac{S_a(T_i)}{PGA}\right)} \tag{5.11}$$

where T_i are logarithmically spaced discrete periods in the $PSA$with $S_a/PGA \geq$1.2, $S_a(T_i)$ are the spectral accelerations, and PGA is the peak ground acceleration.

Regarding the applicability of these parameters, [128] reported that period T_m is representative of the frequency content of strong motions over moderate to long periods. In opposition, period T_o is associated with low to moderate period contents of strong motions. Based on these definitions, this study stated that the use of FAS is more representative of the frequency content than the PSA spectrum. In fact, this is explained by the fact that PSA consists of an approximation of the frequency content of the motion since it represents the maximum response of a single degree of freedom oscillator ($SDOF$). Thus, the use of T_m is recommended over other characteristic periods and its prediction is subjected to less variability.

The predominant spectral period (T_p) corresponds to the period related to the maximum spectral acceleration. Since it is defined as a single point of the PSA spectrum, this parameter is subjected to large variability. However, in some cases, this parameter is still used in practice because of the simplicity of its determination and thus was included in the following analyses. Note that a previous study by [10] used this parameter in the assessment of the accuracy of EQL analyses and found that the analysis of the intra-site residuals exhibited a bias towards over-prediction for $T_p >$ 0.2-0.3 s.

The residuals and ratio of surface to downhole of T_m are compared with the observed motion for the EQL, NL-TS and NL-ES analyses are presented in Fig. 5.28. The residuals and ratio of surface to downhole of T_o and T_p are compared with the observed motion for all analyses in 5.29.

With a few exceptions, the results presented herein suggest that all the analyses appear to capture T_m better compared to the other parameters presented in 5.29, since the average residuals are mostly centered around zero. This tendency follows an downward slope for the motions with higher levels of nonlinearities, or for $I_\gamma >$ 1e-3. At $I_\gamma >$ 7e-4, the predictions

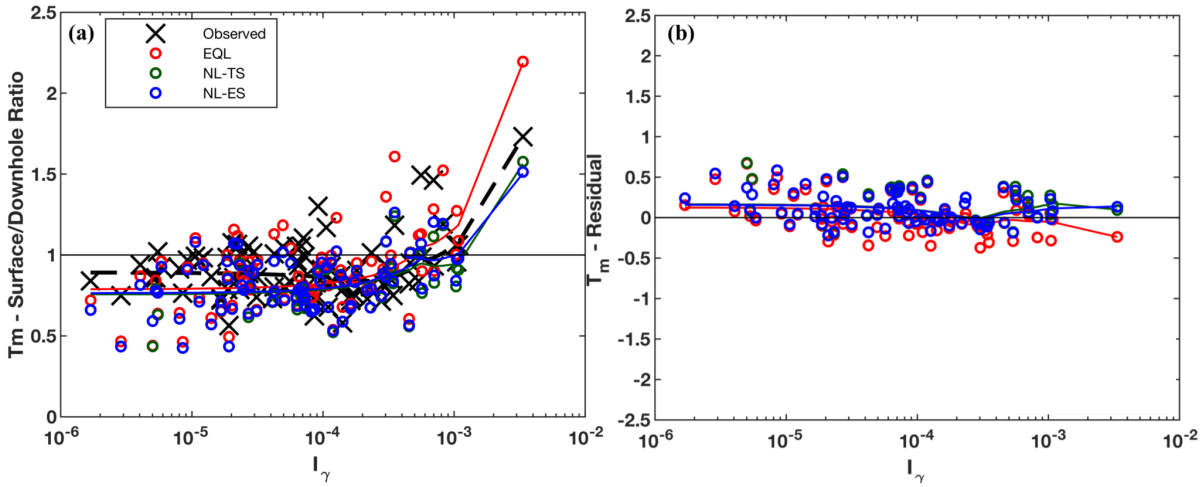


Figure 5.28 Residuals (a) and Ratio ratio of surface to downhole (b) of T_m as a function of the observed downhole shear strain index I_γ for EQL, NL-TS, and NL-ES analyses.

of NL-ES appear to be more biased than NL-TS. The average residuals show that most models over-predict the motions' mean periods, with the EQL approach providing slightly less precision. Finally, both the range of the residuals, from -0.37 to 0.68 (maximum error of 0.20 s) approximately, and the tendency towards over-prediction are in good agreement with the findings of AI, D_{5-95}, and D_{25-75}. When comparing the ratios of surface to downhole mean periods, a period lengthening effect is observed at high strains, consistent with observations for both NL-TS and NL-ES. However, EQL simulations show an important misfit at all strain levels.

For parameter T_o, all models show a large negative bias (Fig. 5.29a) and similar unrealistic tendencies of the over-prediction of period lengthening (Fig. 5.29c) across all levels of nonlinearities with average ratios of approximately 2 and a slight decrease for the NL-ES analysis. This is contrary to the observed records, where unexpectedly the periods are mostly shortened, which is contrary to the expected behavior. There is also a larger variability in the results with maximum computed ratios of 6.70, which is the highest for all the parameters compared. The computed residuals ranged from -1.87 (error of 0.83 s) to 0.48. Finally, for T_p, a larger variability is obtained both in terms of the observed response and the comparison between the predictions of the different models when comparing with the results of the T_m parameter (residuals ranging from -1.68 to 1.25, with max. error of 0.52 s) Overall, these results suggest that the predictions of T_m from the different models are close to the observations and diverge for T_o and T_p. Thus, this confirms the findings reported in [128], which recommended the use of T_m for characterizing the frequency content of the motion, since it is subjected to less variability.

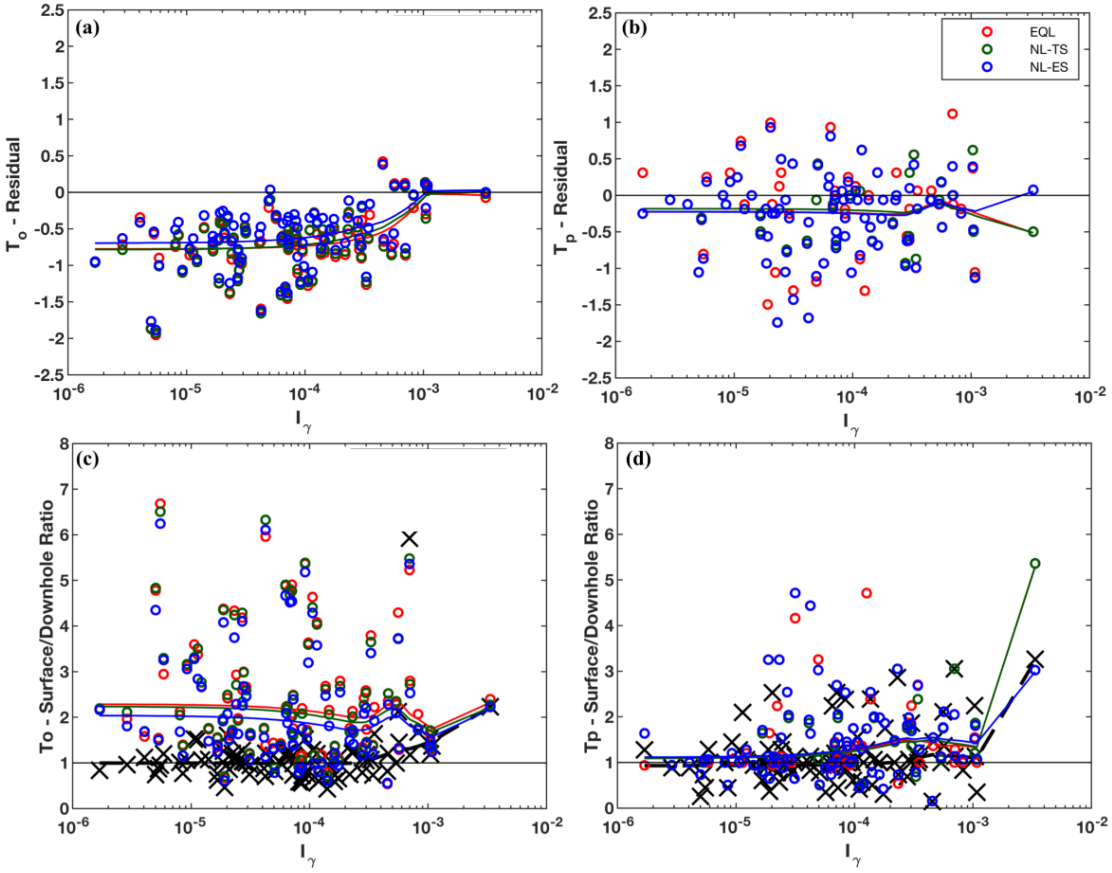


Figure 5.29 Residuals (a-b) and Ratio ratio of surface to downhole (c-d) of T_o and T_p as a function of the observed downhole shear strain index I_γ for EQL, NL-TS, and NL-ES analyses.

The similarities between the predictions of AI and D_{5-95} are also reflected in the comparison of the individual calibrations of the ES model presented in Fig 5.30. In fact, for both T_m and T_p, the findings reveal the same increased variability for high strain motions, where the predictions of the calibrations diverge at a threshold of approximately I_γ = 2e-4. For T_o, this diverging tendency occurs at all strain levels. The amplitude of the ratios is the lowest for T_m, which further supports prioritizing this parameter, specifically when using effective stress ground response analysis.

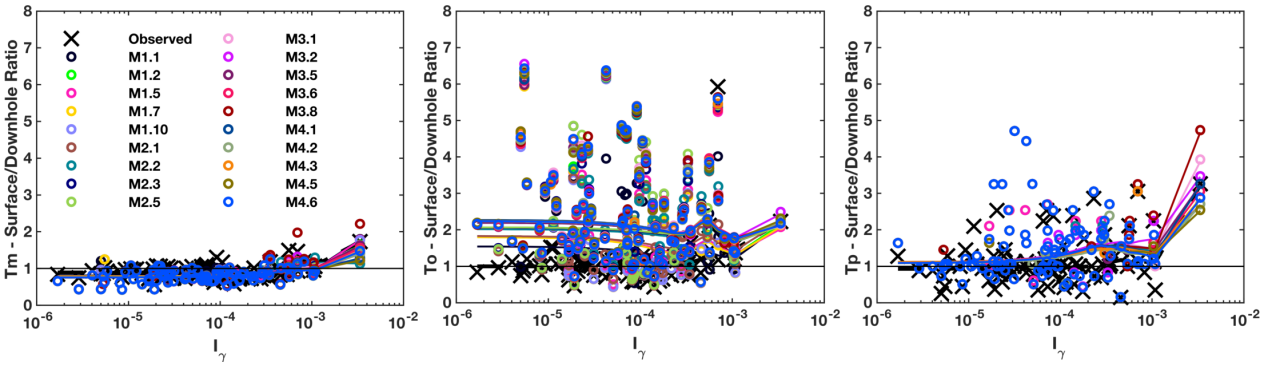


Figure 5.30 Ratio of surface to downhole of T_m, T_o, and T_p as a function of the observed downhole shear strain index I_γ for NL-ES analysis per calibration.

5.7.7 Comparison against PGA, PGV, and $PSA(T)$ for each scenario

In this section, the parameters described in Section 5.7.1 to 5.7.6 are compared against other parameters such as PGA and PGV of the downhole motion and the PSA at periods $T =$ 0.1 and 1s, in order to evaluate the possibility of the presence of a systematic bias in the data. First, the results are presented for Scenario 1, when the motions from the centrifuge tests affected by increased dilative tendencies and soil softening are neglected, as identified in Table 5.1 and discussed in Section 5.2. Then, Scenario 2 is considered regrouping all 98 motions considered in this study. Note that the predicted values of the dataset for EQL, NL-TS, and NL-ES analyses summarized in Table 5.3 (described by the min, max, standard deviation, average) for each ground motion parameter and are compared against the observed data for Scenario 1 and 2.

Scenario 1:

The residuals of the parameters AI, D_{5-95}, D_{25-75}, N_{eq}, CAV, CAV_{STD}, SIR, T_m, T_o, and T_p against PGA, PGV, $PSA_{T=0.1s}$, and $PSA_{T=1s}$ are presented in Fig. 5.31 and Fig. 5.32 for Scenario 1. Overall, the results are consistent with the trends identified when comparing the analysis of the residuals against the shear strain index I_γ.

Scenario 2 – All motions:

The residuals of the parameters AI, D_{5-95}, D_{25-75}, N_{eq}, CAV, CAV_{STD}, SIR, T_m, T_o, and T_p against PGA, PGV, $PSA_{T=0.1s}$, and $PSA_{T=1s}$ are presented in Fig. 5.33 and Fig. 5.34 for Scenario 2. Note that the y-axis scale for AI, CAV, CAV_{STD}, SIR was changed to better represent the trends in the data. The main difference is associated with the increase in the negative bias obtained for the motions of the centrifuge tests for high levels of nonlinearities

when estimating parameter AI, N_{eq}, CAV, CAV_{STD}, SIR, T_m, T_o, and T_p. This leads to a downward tendency and the over-prediction of these parameters when including the results from the high strain motions of the centrifuge tests. In particular, this tendency is amplified when estimating parameter AI and SIR, with residuals reaching a maximum of -6.30 compared to -1.50 in Scenario 1. Thus, this suggests that the amplitude of the predicted acceleration time histories have been over-predicted, as observed in Fig. 16 for the high strain motions in test CFF2. When comparing the residuals against I_γ, this tendency occurs for $I_\gamma > 10e\text{-}3$, or for high levels of nonlinearities. These results corroborate the findings found in the previous sections (Section 5.2, 5.4 and 5.5), which suggested that a significant decrease in the accuracy and precision of the analyses is obtained when including the motions from the centrifuge tests which are affected significantly by dilative tendencies. In Scenario 2, the residuals of the NL-ES for SIR appear to be reduced compared to the EQL and NL-TS total stress analyses for the highest values of all the x-axis parameters that were studied. In opposition, parameters D_{5-95} and D_{25-75}, appear to be the less affected by the inclusion of these motions. When comparing the amplitude of the residuals of all the evaluated intensity measures, T_m seems to be the best overall predicted parameter because the lowest uncertainty is obtained.

Table 5.3 Minimum, maximum and standard deviation of predicted set of data for each ground motion parameter for scenario 1

Analysis	Parameter	Units	Min	Max	Std. Dev. σ_i	Avg.
Observed	AI	m/s	5.20E-05	28.27	3.16	0.75
	D_{5-95}	s	3.80	82.10	16.92	24.08
	D_{25-75}	s	0.21	31.72	5.64	6.72
	N	cycles	1.27	18.56	3.10	5.72
	T_m	s	0.15	0.87	0.13	0.33
	T_o	s	0.09	0.97	0.14	0.25
	T_p	s	0.07	1.13	0.16	0.22
	CAV	g-s	0.01	9.25	1.06	0.60
	CAV_{STD}	g-s	0	8.59	0.99	0.35
	SIR	m/s/s	6.69E-06	1.62	0.19	0.07
EQL	AI	m/s	8.90E-05	23.80	2.84	0.86
	D_{5-95}	s	4.66	124.88	26.40	34.71
	D_{25-75}	s	0.74	59.26	11.43	11.88
	N	cycles	1.19	21.03	3.77	6.55
	T_m	s	0.10	1.11	0.16	0.33
	T_o	s	0.25	1.14	0.20	0.48
	T_p	s	0.09	1.85	0.23	0.29
	CAV	g-s	0.01	7.64	0.98	0.63
	CAV_{STD}	g-s	0	6.99	0.87	0.38
	SIR	m/s/s	1.68E-05	0.94	0.15	0.06
NL-TS	AI	m/s	6.70E-05	24.51	2.81	0.80
	D_{5-95}	s	5.76	100.82	21.10	32.20
	D_{25-75}	s	1.02	34.30	6.53	9.59
	N	cycles	1.30	18.14	3.82	7.44
	T_m	s	0.10	0.79	0.12	0.30
	T_o	s	0.26	1.08	0.20	0.47
	T_p	s	0.09	1.85	0.23	0.28
	CAV	g-s	0.01	7.66	0.96	0.59
	CAV_{STD}	g-s	0	7.05	0.87	0.37
	SIR	m/s/s	1.56E-05	0.51	0.10	0.05
NL-ES	AI	m/s	6.80E-05	22.33	2.56	0.75
	D_{5-95}	s	5.66	101.38	21.04	32.35
	D_{25-75}	s	1.01	34.99	6.56	9.64
	N	cycles	1.30	18.52	3.81	7.35
	T_m	s	0.13	0.76	0.12	0.30
	T_o	s	0.26	0.96	0.18	0.43
	T_p	s	0.09	1.04	0.17	0.27
	CAV	g-s	0.05	7.30	1.30	0.91
	CAV_{STD}	g-s	0	6.68	0.82	0.36
	SIR	m/s/s	1.56E-05	0.50	0.10	0.05

Table 5.4 Minimum, maximum and standard deviation of predicted set of data for each ground motion parameter for scenario 2

Analysis	Parameter	Units	Min	Max	Std. Dev. σ_i	Avg.
Observed	AI	m/s	5.20E-05	28.27	3.16	1.00
	D_{5-95}	s	3.80	82.10	16.38	23.08
	D_{25-75}	s	0.12	31.72	5.55	6.65
	N	cycles	1.04	18.56	3.06	5.45
	T_m	s	0.15	0.87	0.15	0.35
	T_o	s	0.09	0.97	0.14	0.25
	T_p	s	0.065	1.13	0.16	0.22
	CAV	g-s	0.01	9.25	1.06	0.60
	CAV_{STD}	g-s	0	8.59	0.99	0.43
	SIR	m/s/s	6.69E-06	2.59	0.33	0.11
EQL	AI	m/s	8.90E-05	102.36	14.94	4.12
	D_{5-95}	s	4.66	124.88	25.70	32.60
	D_{25-75}	s	0.74	59.26	11.02	11.29
	N	cycles	1.18	21.03	3.82	1 6.46
	T_m	s	0.10	1.11	0.18	0.36
	T_o	s	0.25	1.28	0.28	0.55
	T_p	s	0.09	1.85	0.25	0.32
	CAV	g-s	0.01	12.02	2.02	1.08
	CAV_{STD}	g-s	0	6.99	1.09	0.61
	SIR	m/s/s	1.68E-05	12.02	1.90	0.50
NL-TS	AI	m/s	6.70E-05	73.39	10.83	3.21
	D_{5-95}	s	5.76	100.82	20.51	30.64
	D_{25-75}	s	1.02	34.30	6.38	9.39
	N	cycles	1.30	20.07	3.89	7.50
	T_m	s	0.102	0.79	0.14	0.32
	T_o	s	0.26	1.26	0.28	0.54
	T_p	s	0.09	1.85	0.25	0.32
	CAV	g-s	0.01	10.51	1.84	1.02
	CAV_{STD}	g-s	0	7.05	1.00	0.56
	SIR	m/s/s	1.56E-05	10.51	1.69	0.44
NL-ES	AI	m/s	6.80E-05	22.37	4.77	1.86
	D_{5-95}	s	5.66	101.38	20.53	30.54
	D_{25-75}	s	1.01	34.99	6.33	9.22
	N	cycles	1.30	18.52	3.75	6.97
	T_m	s	0.123	1.12	0.19	0.35
	T_o	s	0.26	1.26	0.27	0.50
	T_p	s	0.09	1.25	0.23	0.33
	CAV	g-s	0.01	7.30	1.25	0.85
	CAV_{STD}	g-s	0	6.68	0.91	0.51
	SIR	m/s/s	1.56E-05	5.09	0.98	0.29

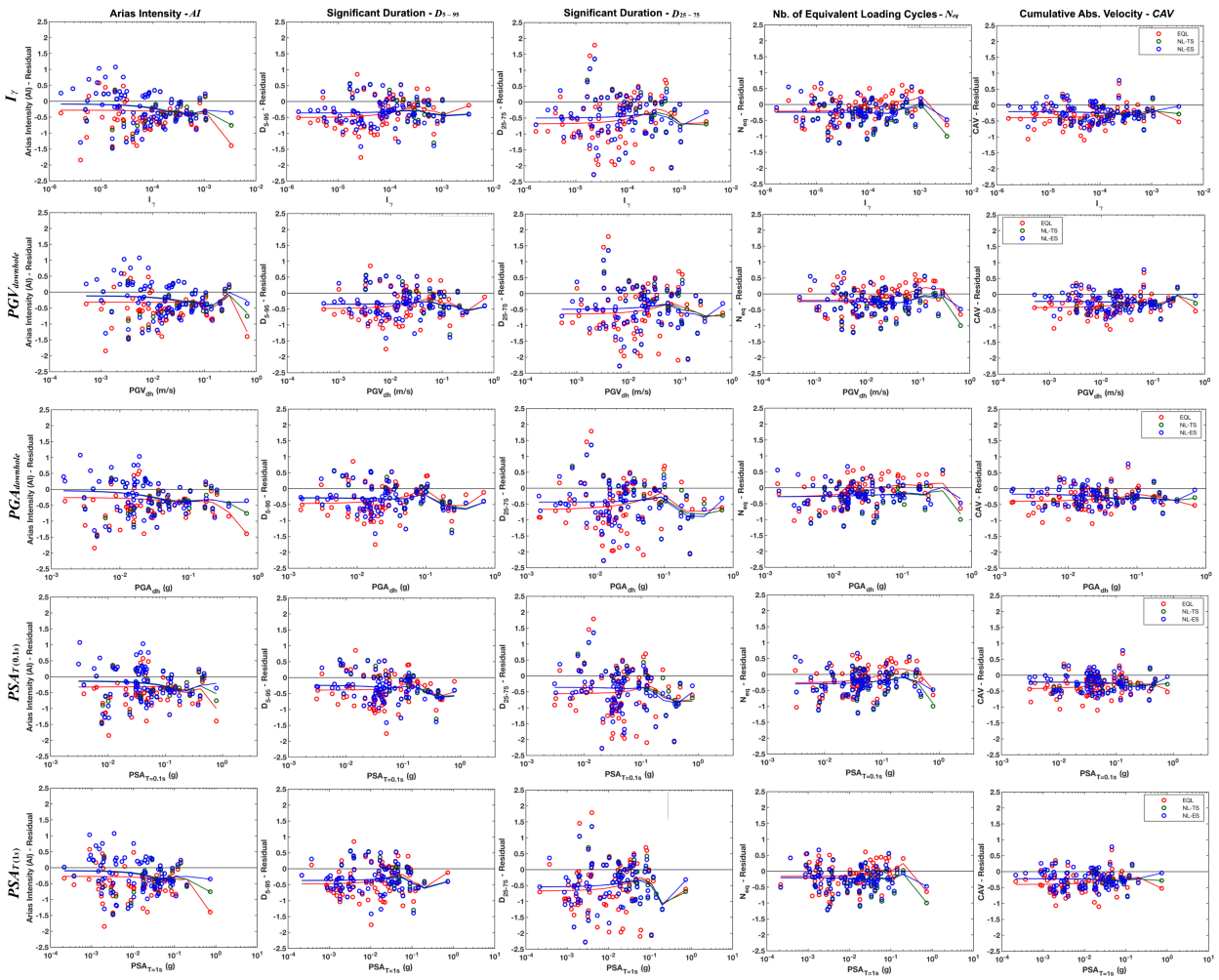


Figure 5.31 Residuals of parameters AI, D_{5-95}, D_{25-75}, N_{eq}, CAV as a function of I_γ, PGA, PGV, $PSA_{T=0.1s}$, and $PSA_{T=1s}$ – scenario 1.

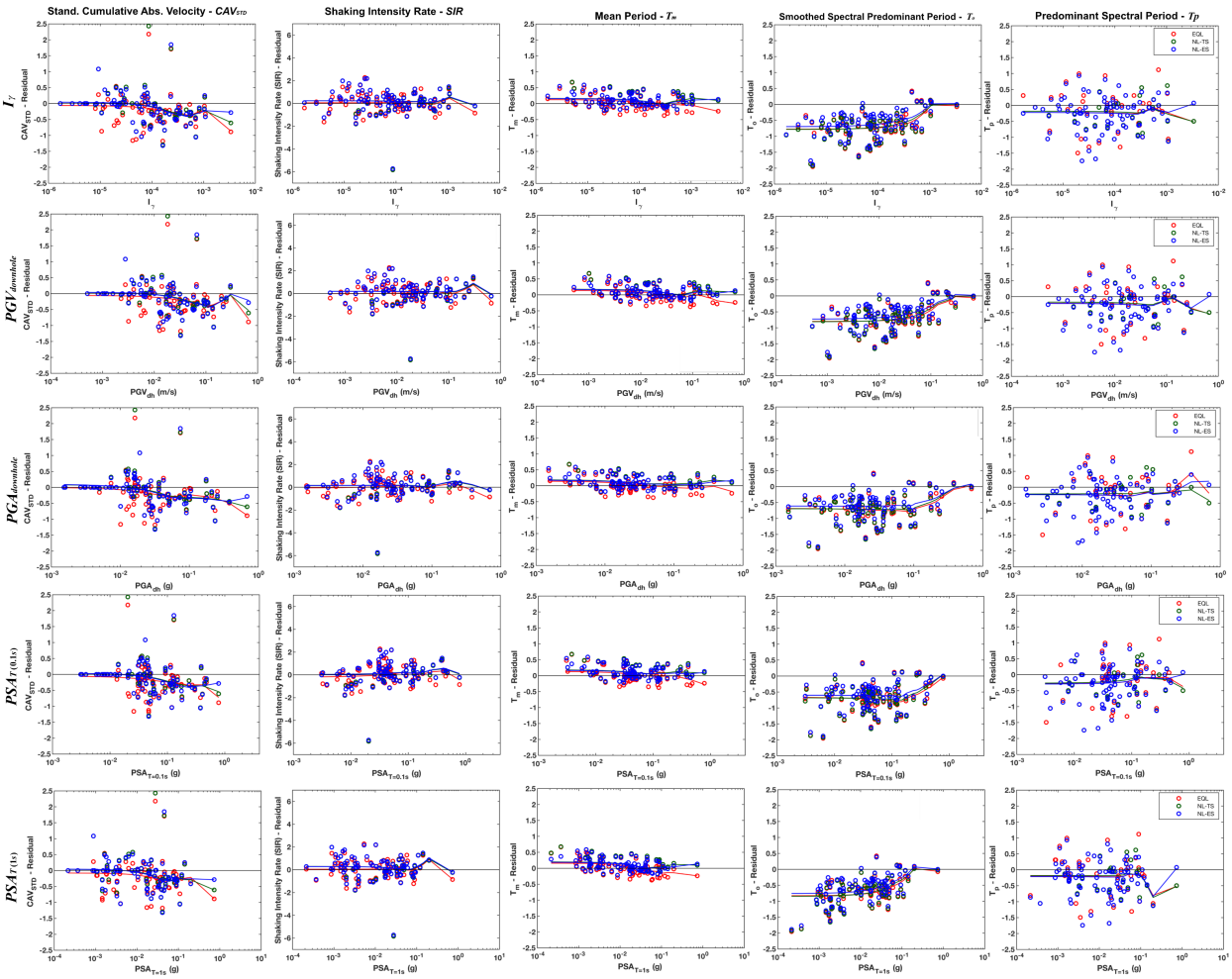


Figure 5.32 Residuals of parameters CAV_{STD}, SIR T_m, T_o, and T_p as a function of I_γ, PGA, PGV, $PSA_{T=0.1s}$, and $PSA_{T=1s}$ – scenario 1.

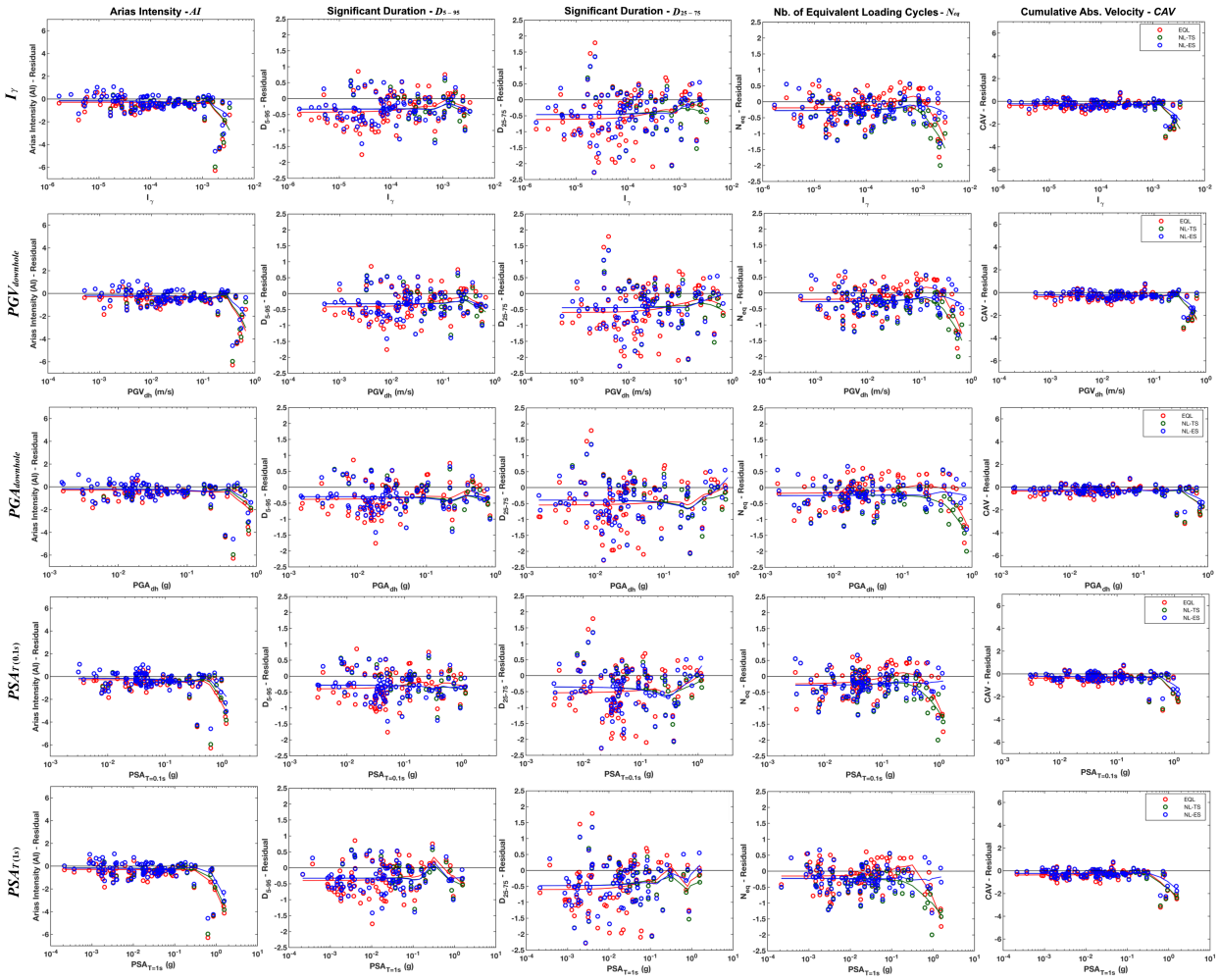


Figure 5.33 Residuals of parameters AI, D_{5-95}, D_{25-75}, N_{eq}, CAV as a function of I_γ, PGA, PGV, $PSA_{T=0.1s}$, and $PSA_{T=1s}$ – scenario 2.

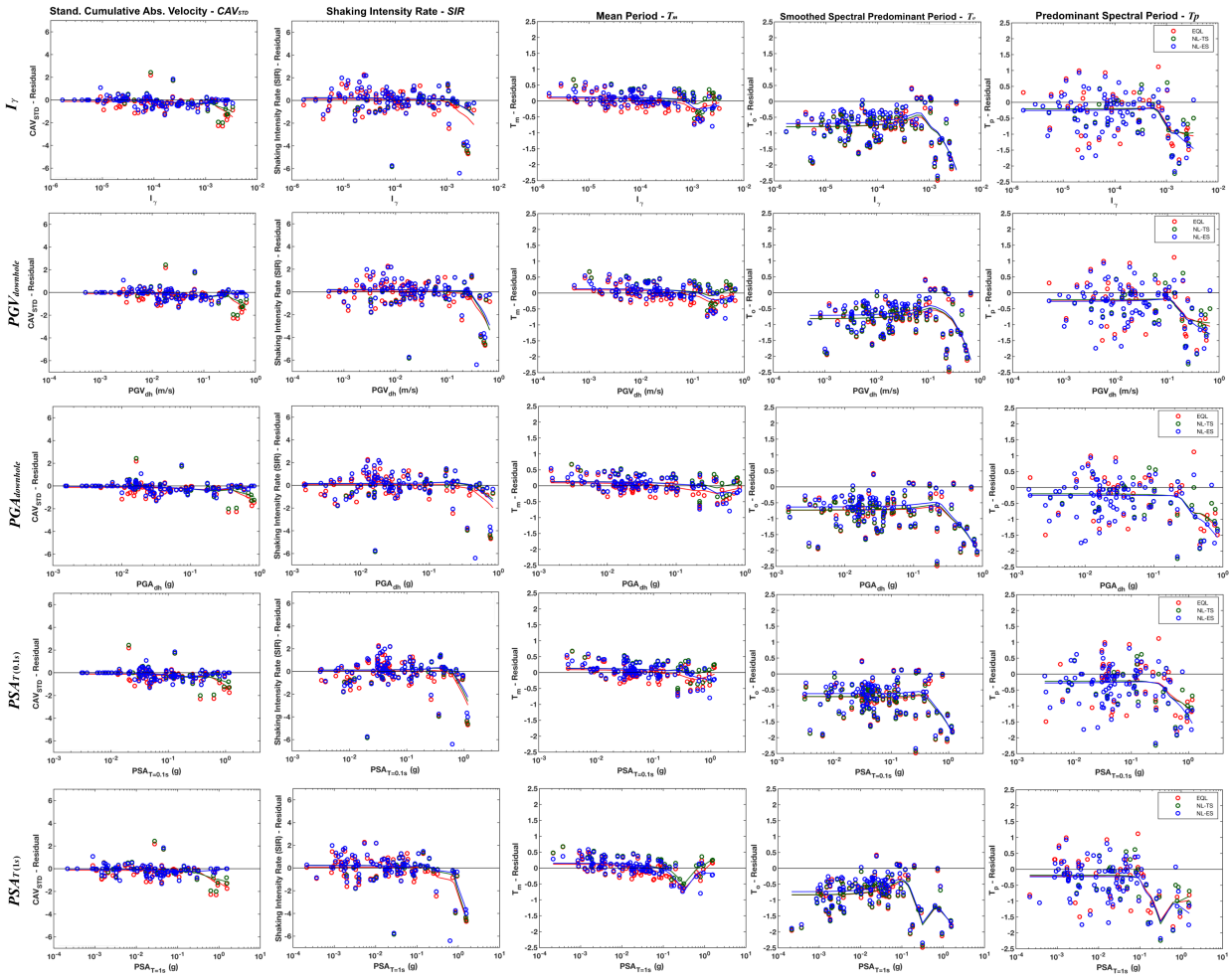


Figure 5.34 Residuals of parameters CAV_{STD}, SIR, T_m, T_o, and T_p as a function of I_γ, PGA, PGV, $PSA_{T=0.1s}$, and $PSA_{T=1s}$ – scenario 2.

5.7.8 Summary

In this section, a summary of the comparison of the precision and accuracy of the predictions of the ground motion parameters is provided. Considering that the differences were shown to be small between each type of analysis and scenario, as described in Section 5.7.1 to 5.7.7, the residuals are presented for the EQL and NL-TS analyses and scenario 1. The predicted and observed values of the dataset are detailed in Table 5.3 for scenario 1 and defined by the minimum, maximum, standard deviation σ_i and average of each dataset for the EQL, NL-TS and NL-ES analyses. In Fig. 5.35, are presented the range and mean of the residuals obtained when comparing the EQL and NL-TS results to the observed values for each parameter.

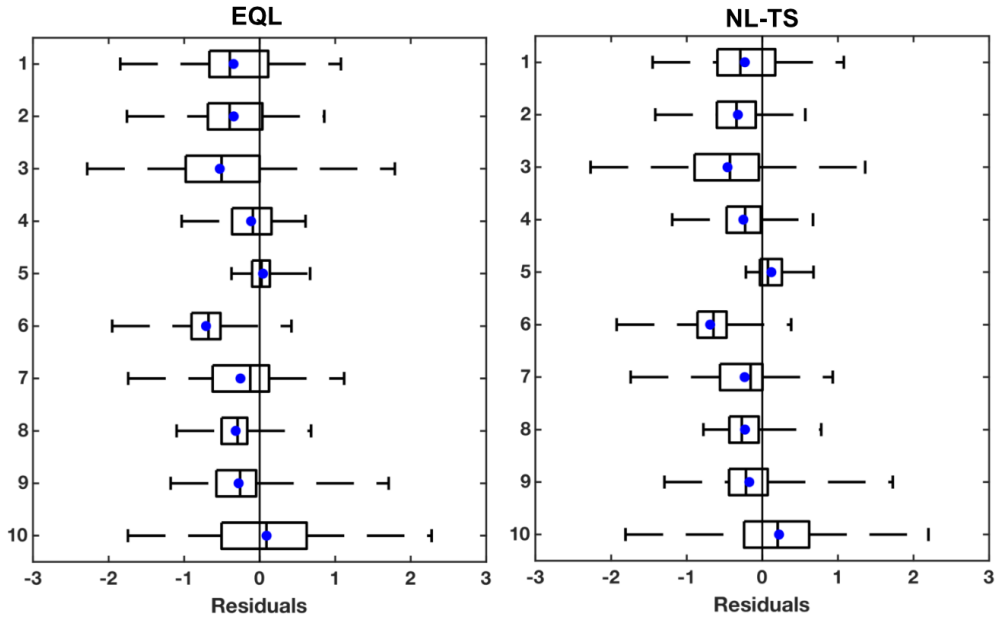


Figure 5.35 Range of residuals for each ground motion parameter for the EQL and NL-TS analyses for scenario 1.

The results from Table 5.3 shows that the lowest computed standard deviations σ_i are obtained for SIR and for the parameters based on the frequency content of the motion such as: T_m, T_o, and T_p. From the results of Fig. 5.35, a tendency towards the over-prediction of these parameters is revealed expect for T_m and SIR which are slightly under-predicted. The range of residuals is the largest for D_{25-75} and SIR and the largest error is committed upon the evaluation of T_o with average residuals values significantly diverging from zero. Thus, this suggests that ground response analysis can accurately capture this frequency content parameter. Excluding T_m, the intensity measures N_{eq} and CAV also demonstrate low variability and range of residuals compared to the other ground motion parameters. In general, the

range of residuals obtained from the nonlinear analysis was revealed to be slightly narrower than for the equivalent-linear analysis across all the investigated parameters. However, this difference was not found to be particularly significant. The average residuals also appear to be slightly decreased with the use of NL models except for parameters N_{eq}, T_m and SIR.

5.8 Limitations

The following section discusses the limitations that might have influenced the results obtained in this study. The scarcity of earthquake recordings at key locations from a liquefaction standpoint, the uncertainty related to site properties, limitations of current effective stress models and nonlinear models are discussed.

First, while an effort was made to select sites with ground motions with a broad range of amplitudes and pore pressure buildup levels, only a few downhole seismic arrays are instrumented with pore pressure transducers and have recorded liquefaction. In comparison with studies using a similar mixed-effect regression model [7, 10] which used respectively 100 Kik-net sites and 3720 ground motions and 6 sites and 191 ground motions, the sample size in this study is composed of only 7 sites and 98 ground motions. In addition, only 11 motions were confirmed cases of liquefaction obtained from pore pressure transducers records. Given the smaller sample size, the results from such analyses should be interpreted with caution and would benefit from being validated by a larger sample size, which requires further data collection. In particular, the installation of pore pressure transducers would be of interest since the unavailability of pore pressure records at most sites used in this study restricted the analysis of the results. In fact, only centrifuge tests, WLA and the Lotung sites had some. Since the high-strain motions of the centrifuge tests were more strongly affected by dilative tendencies, this was found to influence considerably the precision of the predicted behavior.

Another limitation of the current study is associated with the uncertainty regarding the site properties. As discussed previously, although the profiles were calibrated by performing ground response analyses for the low amplitude motions, the coarseness of the Kik-net shear-wave velocity profiles (KSRH07 and TCGH16) and sometimes unknown profiles for the centrifuge tests (CSP3 and CFF2), may have interfered in the results. In addition, limited information on the soil properties was sometimes available at some of the sites and few geotechnical investigations were conducted. The calibration of effective stress models is complex because they require a large number of input parameters, that are difficult to calibrate even with the proposed correlation relationships developed considering that most of them have been developed on clean sands. In general, the models require fitting parameters based on laboratory test data where few guidelines are proposed. Thus, due care must be exercised when using these models to represent different soil types and conditions. Despite these limitations, it is believed that the findings of this study would compare well with the approach that would be used in practice by an engineer. In fact, a rigorous calibration scheme of these models was adopted involving a total of 34 different calibrations.

Other limitations of the current effective stress models include the dissipation of pore pressures in the vertical direction only which might induce unrealistic strains and behaviors. The investigation of the high-strain motions in the centrifuge tests have also demonstrated the importance of developing models that account for dilatation in a more accurate manner. Finally, only one model can be used to represent the development of pore pressures in clays, and its predictions were found to not capture the observed behavior [30].

Given that the focus of this study was the assessment of effective stress approach, there is a possibility that a number of limitations might have influenced the results obtained. Namely, past studies have highlighted areas of improvements regarding the implementation of the 1D nonlinear models. For instance, the uncertainties of these models, may be associated with site characterization, constitutive model and their input parameters, form of the computational model and instrument recordings [124]. The computational model uncertainties includes the simplification of the model as a 1D problem, which neglects 2D-3D effects (soil stratigraphy and wave propagation), and have been identified by previous studies as a potential source of inaccuracy [8–11, 14, 67, 163–165]. Also, the vertical component of the earthquake motions was not considered in the present study. Past earthquakes (Northridge 1994, Kobe 1995) have shown that these may be associated with strong amplitudes and can result in significant damage to engineering structures [124, 166, 167]. Thus, this component of the motion should be considered when performing ground response analyses. While studies have attempted to develop vertical ground response analytical procedures [168–170], further research is recommended to establish reliable procedures [171]. However, for the scope of this study, the vertical component of the motion is not expected to influence liquefaction as much as the horizontal one.

CHAPTER 6 CONCLUSION

In this study, mixed-effect regression analysis and Pearson's correlation coefficient were used to evaluate the performance of 1D nonlinear effective stress analysis over equivalent linear and nonlinear total stress analyses. The ground response analyses were conducted for seven liquefaction case studies and 98 earthquake recordings representing varying ground motion amplitude and pore pressure buildup levels. Five effective stress constitutive models were reviewed and compared, and their input parameters were calibrated based on the available site properties, recommendations by the authors and general correlation relationships found in the litterature.

In general, the evidence from this study implies that effective stress models have poor accuracy compared with total stress nonlinear models in terms of the evaluation of the response spectra. In fact, the findings indicate that effective stress models increased the variability at long periods. Although, the results demonstrated the ability of the models of capturing liquefaction when it occurred. Moreover, the selection of the input parameters showed low variability in the results when comparing a set of different calibrations. This research highlighted the importance of addressing the current limitations of the effective stress models, particularly in the selection of the input parameters and the accuracy of the dilative behavior. The effective stress models were also found to approximate reasonably well, with a few exceptions, the expected behavior of liquefiable soils in terms of their pore pressure response as a function of shear strain when compared to existing correlation relationships. In some cases, the models also reproduced accurately the rate of generation and dissipation of the excess pore pressures with time. Finally, the comparison of the predictions of common ground motion parameters, including the Arias intensity, significant durations, number of loading cycles, cumulative absolute velocities, shaking intensity rate and characteristic periods, revealed a tendency towards their over-prediction. Overall, the mean period T_m was found to yield the best accuracy resulting from ground response analyses.

Therefore, based on these results, effective stress analyses are considered as being not yet satisfying tools to use in practice. Further work on the topic is required before the integration of effective stress models in 1D ground response analysis. Thus, in opposition to the recommendations of the National Building Code of Canada 2015, the results of this study indicate that a rigorous nonlinear total stress analysis should be prioritized over the effective stress approach. Based on these results, future work should focus on the validation of the models against earthquake recordings of varying amplitudes and pore pressure generation

levels and not only for motions triggering liquefaction.

The importance of this work lies in the fact that this study provides a valuable framework for the validation of future effective stress models by the development of a vast database of liquefaction case studies. Considerable research has been conducted by the author to thoroughly characterize each of the considered soil profiles and their properties. The findings reported in this study improve the knowledge of the integration of the effective stress approach and the liquefiable behavior in ground response analysis procedures. The aim is to bridge the gap that currently exists between the theoretical models developed and their potential use in practice in order to increase the use of these procedures in practice. Therefore, this research constitutes an initial step towards the development of new models and provides a useful aid in the accomplishment of this task by identifying the areas of improvement of the current available models. The long-term goal of this research would be to integrate these findings in the development of design guidelines for practitioners. These would assist them in accurately performing effective stress 1D ground response analysis as well as better representing the influence of excess pore water pressures on the cyclic behavior of both sands and clays.

BIBLIOGRAPHY

[1] J. Olarte, B. Paramasivam, S. Dashti, A. Liel, and J. Zannin, "Centrifuge modeling of mitigation-soil-foundation-structure interaction on liquefiable ground," *Soil Dynamics and Earthquake Engineering*, vol. 97, pp. 304–323, 2017.

[2] I. M. Idriss and H. B. Seed, "Seismic response of horizontal soil layers," *American Society of Civil Engineering Soil Mechanics and Foundations Division*, 1968.

[3] H. B. Seed and I. Idriss, "Analyses of ground motions at Union Bay, Seattle during earthquakes and distant nuclear blasts," *Bulletin of the Seismological Society of America*, vol. 60, no. 1, pp. 125–136, 1970.

[4] P. B. Schnabel, "SHAKE: A computer program for earthquake response analysis of horizontally layered sites," *EERC Report 72-12, University of California, Berkeley.*, 1972.

[5] N. M. Newmark, "A method of computation for structural dynamics," *Journal of the Engineering Mechanics Division*, vol. 85, no. 3, pp. 67–94, 1959.

[6] J. P. Stewart, Y. M. A. Hashash, N. Matasovic, R. Pyke, Z. Wang, and Z. Yang, *Benchmarking of nonlinear geotechnical ground response analysis procedures*. Pacific Earthquake Engineering Research Center, 2008.

[7] J. Kaklamanos, L. G. Baise, E. M. Thompson, and L. Dorfmann, "Comparison of 1D linear, equivalent-linear, and nonlinear site response models at six KiK-net validation sites-net validation sites," *Soil Dynamics and Earthquake Engineering*, vol. 69, pp. 207–219, 2015.

[8] A. O. Kwok, J. P. Stewart, and Y. M. Hashash, "Nonlinear ground-response analysis of Turkey Flat shallow stiff-soil site to strong ground motion," *Bulletin of the Seismological Society of America*, vol. 98, no. 1, pp. 331–343, 2008.

[9] B. Kim and Y. M. Hashash, "Site response analysis using downhole array recordings during the march 2011 Tohoku-Oki earthquake and the effect of long-duration ground motions," *Earthquake spectra*, vol. 29, no. s1, pp. S37–S54, 2013.

[10] J. Kaklamanos, B. A. Bradley, E. M. Thompson, and L. G. Baise, "Critical parameters affecting bias and variability in site-response analyses using KiK-net downhole array

data," *Bulletin of the Seismological Society of America*, vol. 103, no. 3, pp. 1733–1749, 2013.

[11] J. Kaklamanos and B. A. Bradley, "Evaluation of 1D nonlinear total-stress site response model performance at 114 KiK-net downhole array sites," in *Proceedings of the 6th International Conference on Earthquake Geotechnical Engineering*, Christchurch, New Zealand, 2015, pp. 1–4.

[12] G. Zalachoris and E. M. Rathje, "Evaluation of one-dimensional site response techniques using borehole arrays," *Journal of Geotechnical and Geoenvironmental Engineering*, vol. 141, no. 12, p. 04015053, 2015.

[13] J. Shi and D. Asimaki, "From stiffness to strength: Formulation and validation of a hybrid hyperbolic nonlinear soil model for site-response analyses," *Bulletin of the Seismological Society of America*, vol. 107, no. 3, pp. 1336–1355, 2017.

[14] J. Kaklamanos and B. A. Bradley, "Challenges in predicting seismic site response with 1D analyses: Conclusions from 114 KiK-net vertical seismometer arrays," *Bulletin of the Seismological Society of America*, vol. 108, no. 5A, pp. 2816–2838, 2018.

[15] G. Li, R. Motamed, and S. Dickenson, "Evaluation of one-dimensional multi-directional site response analyses using geotechnical downhole array data in California and Japan," *Earthquake Spectra*, vol. 34, no. 1, pp. 349–376, 2018. [Online]. Available: http://dx.doi.org/10.1193/010617EQS005M

[16] I. M. Idriss and R. W. Boulanger, *Soil liquefaction during earthquakes*. Oakland: EERI Publication, Monorgraph MNO-12, Earthquake Engineering Research Institute, 2008.

[17] W.-J. Chang, E. M. Rathje, K. H. Stokoe, and K. Hazirbaba, "In situ pore-pressure generation behavior of liquefiable sand," *Journal of Geotechnical and Geoenvironmental Engineering*, vol. 133, no. 8, pp. 921–931, 2007.

[18] Y. M. A. Hashash, M. I. Musgrove, J. A. Harmon, D. Groholski, C. A. Phillips, and D. Park, "Deepsoil v6.1, user manual, technical report„" Urbana, IL, Tech. Rep., 2016.

[19] J. Régnier, L.-F. Bonilla, P.-Y. Bard, E. Bertrand, F. Hollender, H. Kawase, D. Sicilia, P. Arduino, A. Amorosi, D. Asimaki *et al.*, "PRENOLIN: International benchmark on 1D nonlinear site-response analysis," *Bulletin of the Seismological Society of America*, vol. 108, no. 2, pp. 876–900, 2018.

[20] D. R. Groholski, Y. M. Hashash, B. Kim, M. Musgrove, J. Harmon, and J. P. Stewart, "Simplified model for small-strain nonlinearity and strength in 1D seismic site response analysis," *Journal of Geotechnical and Geoenvironmental Engineering*, vol. 142, no. 9, p. 04016042, 2016.

[21] M. Vucetic and R. Dobry, "Degradation of marine clays under cyclic loading," *Journal of Geotechnical Engineering*, vol. 114, no. 2, pp. 133–149, 1988.

[22] R. Green, J. Mitchell, and C. Polito, "An energy-based excess pore pressure generation model for cohesionless soils," in *Proceedings of the John Booker Memorial Symposium, Sidney Australia, AA Balkema Publishers, Rotterdam, Netherlands*, 2000.

[23] T. Park and J. Ahn, "Accumulated stress based model for prediction of residual pore pressure," in *Proceedings of the 18th international conference on soil mechanics and geotechnical engineering*, vol. 2, Paris, France, 2013, pp. 1567–1570.

[24] J. Berrill and R. Davis, "Energy dissipation and seismic liquefaction of sands: revised model," *Soils and Foundations*, vol. 25, no. 2, pp. 106–118, 1985.

[25] N. Matasovic and M. Vucetic, "Cyclic characterization of liquefiable sands," *Journal of Geotechnical Engineering*, vol. 119, no. 11, pp. 1805–1822, 1993.

[26] R. Kayen, R. Moss, E. Thompson, R. Seed, K. Cetin, A. D. Kiureghian, Y. Tanaka, and K. Tokimatsu, "Shear-wave velocity–based probabilistic and deterministic assessment of seismic soil liquefaction potential," *Journal of Geotechnical and Geoenvironmental Engineering*, vol. 139, no. 3, pp. 407–419, 2013.

[27] R. Boulanger and I. Idriss, "CPT and SPT based liquefaction triggering procedures," *Report No. UCD/CGM.-14/01, Department of Civil and Environmental Engineering, University of California, Davis, CA*, p. 138, 2014.

[28] K. Ishihara, "Liquefaction and flow failure during earthquakes," *Géotechnique*, vol. 43, no. 3, pp. 351–451, 1993.

[29] N. Matasovic and M. Vucetic, "Generalized cyclic-degradation-pore-pressure generation model for clays," *Journal of geotechnical engineering*, vol. 121, no. 1, pp. 33–42, 1995.

[30] N. Matasovic, "Seismic response of composite horizontally-layered soil deposits," Ph.D. dissertation, University of California at Los Angeles, Los Angeles, California, 1993.

[31] R. Dobry, R. Ladd, F. Y. Yokel, R. M. Chung, and D. Powell, *Prediction of pore water pressure buildup and liquefaction of sands during earthquakes by the cyclic strain method*. Gaithersburg, MD. National Bureau of Standards, 1982, vol. 138.

[32] N. Matasovic and M. Vucetic, "A pore pressure model for cyclic straining of clay," *Soils and Foundations*, vol. 32, no. 3, pp. 156–173, 1992.

[33] M. Vucetic, "Cyclic characterization for seismic regions based on Pl," in *Proceedings of the International Conference on Soil Mechanics and Foundation Engineering*, vol. 1, New Delhi, India, 1994, pp. 329–332.

[34] K. L. Lee and A. Albaisa, "Earthquake induced settlements in saturated sands," *Journal of Geotechnical and Geoenvironmental Engineering*, vol. 100, no. Paper 10496, 1974.

[35] H. B. Seed, R. Pyke, and G. R. Martin, "Effect of multi-directional shaking on liquefaction of sands," Earthquake Engineering Research Center, University of California, Tech. Rep. EERC 75-41, 1975.

[36] J. R. Booker, M. S. Rahman, and H. B. Seed, "GADFLEA: A computer program for the analysis of pore pressure generation and dissipation during cyclic or earthquake loading," 1976.

[37] S. Kramer, *Geotechnical Earthquake Engineering*. Upper Saddle River: Prentice-Hall Civil Engineering and Engineering Mechanics Series, Prentice Hall, 1996, p. 653.

[38] A. Chiaradonna, G. Tropeano, A. d'Onofrio, and F. Silvestri, "Development of a simplified model for pore water pressure build-up induced by cyclic loading," *Bulletin of Earthquake Engineering*, vol. 16, no. 9, pp. 3627–3652, 2018.

[39] V. P. Drnevich and F. Richart, "Dynamic prestraining of dry sand," *Journal of Soil Mechanics & Foundations Division*, 1970.

[40] T. L. Youd, "Compaction of sands by repeated shear straining," *Journal of Soil Mechanics & Foundations Division*, vol. 98, no. sm7, 1972.

[41] M. L. Silver and H. B. Seed, "Volume changes in sands during cyclic loading," *Journal of Soil Mechanics & Foundations Division*, 1971.

[42] R. Pyke, H. Seed, and C. Chan, "Settlement of sands under multidirectional shaking," *Journal of Geotechnical and Geoenvironmental Engineering*, vol. 101, no. ASCE# 11251 Proceeding, 1975.

[43] G. R. Martin, W. L. Finn, and H. B. Seed, "Fundamentals of liquefaction under cyclic loading," *Journal of Geotechnical and Geoenvironmental Engineering*, vol. 101, no. ASCE# 11231 Proceeding, 1975.

[44] W. Finn, P. Bransby, and D. Pickering, "Seismic pore water pressure generation and dissipation," in *Symposium on Soil Liquefaction*. ASCE National Convention Philadelphia, 1976, pp. 169–198.

[45] W. Liam Finn, K. W. Lee, and G. Martin, "An effective stress model for liquefaction," *Electronics Letter*, vol. 103, no. ASCE 13008 Proceedings, 1977.

[46] P. M. Byrne, "A model for predicting liquefaction induced displacement," in *Proceedings of the Second International Conference on Recent Advances in Geotechnical Earthquake Engineering and Soil Dynamics*, St. Louis, Missouri, 1991.

[47] G. Chen, D. Zhao, W. Chen, and C. H. Juang, "Excess pore-water pressure generation in cyclic undrained testing," *Journal of Geotechnical and Geoenvironmental Engineering*, vol. 145, no. 7, p. 04019022, 2019.

[48] R. Dobry, W. Pierce, R. Dyvik, G. Thomas, and R. Ladd, "Pore pressure model for cyclic straining of sand," *Research Report, Rensselaer Polytechnic Institute, Troy, New York*, 1985.

[49] M. Vucetic and R. Dobry, "Cyclic triaxial strain-controlled testing of liquefiable sands," in *Advanced triaxial testing of soil and rock*, R. C. C. Robert T. Donaghe and M. L. S. Eds, Eds. Philadelphia: American Society for Testing and Materials, 1988, no. ASTM STP 977, pp. 475–485.

[50] W. Finn and S. Bathia, "Prediction of seismic pore water pressures," in *10th International conference in soil mechanics and foundations*, Stockholm, 1982, pp. 201–206.

[51] T. Ivšić, "A model for presentation of seismic pore water pressures," *Soil Dynamics and Earthquake Engineering*, vol. 26, no. 2-4, pp. 191–199, 2006.

[52] C. P. Polito, R. A. Green, and J. Lee, "Pore pressure generation models for sands and silty soils subjected to cyclic loading," *Journal of Geotechnical and Geoenvironmental Engineering*, vol. 134, no. 10, pp. 1490–1500, 2008.

[53] B. Carlton, "An improved description of the seismic response of sites with high plasticity soils, organic clays, and deep soft soil deposits," Ph.D. dissertation, 2014.

[54] X. Mei, S. M. Olson, and Y. M. Hashash, "Evaluation of a simplified soil constitutive model considering the implied strength and porewater pressure generation for 1D seismic site response," in *Geotechnical Frontiers 2017: Seismic Performance and Liquefaction*. GSP 281, 2017, pp. 352–360.

[55] S. J. Brandenberg, J. P. Stewart, and K. B. Afacan, "Influence of liquefaction on earthquake ground motions," Final report for USGS award number G12AP20098, Tech. Rep. 2, 2013.

[56] D. W. Wilson, "Soil-pile-superstructure interaction in liquefying sand and soft clay," Ph.D. dissertation, University of California, Davis, 1998.

[57] C. S. Markham, J. D. Bray, J. Macedo, and R. Luque, "Evaluating nonlinear effective stress site response analyses using records from the Canterbury earthquake sequence," *Soil Dynamics and Earthquake Engineering*, vol. 82, pp. 84–98, 2016.

[58] X. Mei, S. Olson, and Y. Hashash, "Evaluation of a simplified soil constitutive model considering implied strength and porewater pressure generation for 1D seismic site response," *Canadian Geotechnical Journal*, 2019.

[59] K. Arulmoli, K. K. Mualeetharan, M. M. Hossain, and L. S. Fruth, "Velacs: Verification of liquefaction analysis by centrifuge studies, laboratory testing program, soil data report," The Earth Technology Corporation, Irvine, California, Tech. Rep. Project No. 90-0562, 1992.

[60] S. Dashti, J. D. Bray, J. M. Pestana, M. Riemer, and D. Wilson, "Centrifuge testing to evaluate and mitigate liquefaction-induced building settlement mechanisms," *Journal of Geotechnical and Geoenvironmental Engineering*, vol. 136, no. 7, pp. 918–929, 2009.

[61] S. M. Olson, X. Mei, and Y. M. Hashash, "Nonlinear site response analysis with porewater pressure generation for liquefaction triggering evaluation," *Journal of Geotechnical and Geoenvironmental Engineering*, vol. 146, no. 2, p. 04019128, 2019.

[62] J.-P. Bardet and M. Kapuskar, "Liquefaction sand boils in San Francisco during 1989 Loma Prieta earthquake," *Journal of Geotechnical Engineering*, vol. 119, no. 3, pp. 543–562, 1993.

[63] S. L. Kramer, S. S. Sideras, M. W. Greenfield, and B. Hushmand, "Liquefaction, ground motions, and pore pressures at the Wildlife Liquefaction Array in the 1987 Superstition Hills earthquake," in *Geotechnical Earthquake Engineering and Soil Dynamics V:*

Liquefaction Triggering, Consequences, and Mitigation. American Society of Civil Engineers Reston, VA, 2018, pp. 384–402.

[64] R. G. Stockwell, L. Mansinha, and R. Lowe, "Localization of the complex spectrum: the S transform," *IEEE transactions on signal processing*, vol. 44, no. 4, pp. 998–1001, 1996.

[65] S. L. Kramer, B. A. Asl, P. Ozener, and S. S. Sideras, "Effects of liquefaction on ground surface motions," in *Perspectives on Earthquake Geotechnical Engineering.* Springer, 2015, pp. 285–309.

[66] S. Kramer, S. Sideras, and M. Greenfield, "The timing of liquefaction and its utility in liquefaction hazard evaluation," *Soil Dynamics and Earthquake Engineering*, vol. 91, pp. 133–146, 2016.

[67] E. M. Thompson, L. G. Baise, Y. Tanaka, and R. E. Kayen, "A taxonomy of site response complexity," *Soil Dynamics and Earthquake Engineering*, vol. 41, pp. 32–43, 2012.

[68] M. Bennett, P. McLaughlin, J. Sarmiento, and T. Youd, "Geotechnical investigation of liquefaction sites, Imperial Valley, California," US Geological Survey, Open-File Report 95-663, 360 pp., Tech. Rep., 1984.

[69] T. L. Youd, C. M. Hansen, and S. F. Bartlett, "Revised multilinear regression equations for prediction of lateral spread displacement," *Journal of Geotechnical and Geoenvironmental Engineering*, vol. 128, no. 12, pp. 1007–1017, 2002.

[70] T. L. Youd, H. A. Bartholomew, and J. S. Proctor, "Geotechnical logs and data from permanently instrumented field sites: Garner Valley Downhole Array (GVDA) and Wildlife Liquefaction Array (WLA)," *NEES@ UCSB internal report*, 2004.

[71] T. L. Youd and T. L. Holzer, "Piezometer performance at Wildlife Liquefaction site, California," *Journal of Geotechnical Engineering*, vol. 120, no. 6, pp. 975–995, 1994.

[72] T. Holzer, T. Hanks, and T. Youd, "Dynamics of liquefaction during the 1987 Superstition Hills, California, Earthquake," *Science*, vol. 244, no. 4900, pp. 56–59, 1989.

[73] NEES@UCSB. (2012) Network for Earthquake Engineering Simulations at University of California, Los Angeles (NEES@UCSB). available at http://nees.ucsb.edu/facilities/wla. [Online]. Available: http://nees.ucsb.edu/facilities/wla

[74] EPRI, "Guidelines for determining design basis ground motions," Electrical Power Research Institute, Palo Alto, CA, Tech. Rep. Report No. EPRI TR-102293, 1993.

[75] D. Anderson and Y. Tang, "Summary of soil characterization program for the Lotung large-scale seismic experiment," in *Proceedings of EPRI/NRC/TPC workshop on seismic soil–structure interaction analysis techniques using data from Lotung*, vol. 1, 1989, pp. 4–1.

[76] D. Anderson, "Geotechnical synthesis report for the Lotung large-scale seismic experiment," *Technical Report No. TR-102362, Electric Power Research Institute, Palo Alto, California*, 1993.

[77] R. I. Borja, H.-Y. Chao, F. J. Montáns, and C.-H. Lin, "SSI effects on ground motion at Lotung LSST site," *Journal of Geotechnical and Geoenvironmental Engineering*, vol. 125, no. 9, pp. 760–770, 1999.

[78] C.-H. Chen, "Pore water pressure response measurement at Lotung site," in *EPRI/NRC/TPC SSI Workshop on Volidation of Seismic Soil-Structure Interaction Analysis Techniques Using Lotung Experiment Data*, 1987, pp. Palo–Alto.

[79] S. Glaser and L. Baise, "System identification estimation of soil properties at the Lotung site," *Soil Dynamics and Earthquake Engineering*, vol. 19, no. 7, pp. 521–531, 2000.

[80] Y. Iwasaki and M. Tai, "Strong motion records at Kobe Port Island," *Soils and foundations*, vol. 36, no. Special, pp. 29–40, 1996.

[81] K. Ishihara, S. Yasuda, and H. Nagase, "Soil characteristics and ground damage," *Soils and Foundations*, vol. 36, no. Special, pp. 109–118, 1996.

[82] T. Shibata, F. Oka, and Y. Ozawa, "Characteristics of ground deformation due to liquefaction," *Soils and foundations*, vol. 36, no. Special, pp. 65–79, 1996.

[83] P. Kirkwood and S. Dashti, "A centrifuge study of seismic structure-soil-structure interaction on liquefiable ground and implications for design in dense urban areas," *Earthquake Spectra*, vol. 34, no. 3, pp. 1113–1134, 2018.

[84] J. Ramirez, A. R. Barrero, L. Chen, S. Dashti, A. Ghofrani, M. Taiebat, and P. Arduino, "Site response in a layered liquefiable deposit: evaluation of different numerical tools and methodologies with centrifuge experimental results," *Journal of Geotechnical and Geoenvironmental Engineering*, vol. 144, no. 10, p. 04018073, 2018.

[85] J. Zhang, R. D. Andrus, and C. H. Juang, "Normalized shear modulus and material damping ratio relationships," *Journal of Geotechnical and Geoenvironmental Engineering*, vol. 131, no. 4, pp. 453–464, 2005.

[86] M. B. Darendeli, "Development of a new family of normalized modulus reduction and material damping curves," Ph.D. dissertation, University of Texas at Austin, 2001.

[87] A. Casagrande, "Classification and identification of soils," *Transactions of the American Society of Civil Engineers*, vol. 113, pp. 901–930, 1948.

[88] W. K. Choi, "Dynamic properties of ash-flow tuffs," Ph.D. dissertation, University of Texas at Austin, 2008.

[89] C. Phillips and Y. M. Hashash, "Damping formulation for nonlinear 1D site response analyses," *Soil Dynamics and Earthquake Engineering*, vol. 29, no. 7, pp. 1143–1158, 2009.

[90] K. Terzaghi and R. B. Peck, *Soil mechanics in engineering pratice*, 2nd ed. New York: John Wiley, 1967.

[91] C. C. Ladd and R. Foott, "New design procedure for stability of soft clays," *Journal of Geotechnical and Geoenvironmental Engineering*, vol. 100, no. Proc Paper 10064, 1974.

[92] C. C. Ladd and D. J. DeGroot, "Recommended practice for soft ground site characterization: Arthur Casagrande Lecture," in *12th Panamerican Conference on Soil Mechanics and Geotechnical Engineering*, vol. 1. Verlag GmbH Essen, Germany, 2003, pp. 1–57.

[93] A. O. Kwok, J. P. Stewart, Y. M. Hashash, N. Matasovic, R. Pyke, Z. Wang, and Z. Yang, "Use of exact solutions of wave propagation problems to guide implementation of nonlinear seismic ground response analysis procedures," *Journal of Geotechnical and Geoenvironmental Engineering*, vol. 133, no. 11, pp. 1385–1398, 2007.

[94] D. M. Boore and J. J. Bommer, "Processing of strong-motion accelerograms: needs, options and consequences," *Soil Dynamics and Earthquake Engineering*, vol. 25, no. 2, pp. 93–115, 2005.

[95] D. M. Boore, "Some thoughts on relating density to velocity," *Notes on personal web, not published*, 2007.

[96] B. Hasselström, "Water prospecting and rock-investigation by the seismic refraction method," *Geoexploration*, vol. 7, no. 2, pp. 113–132, 1969.

[97] F. Haeni, "Application of seismic refraction methods in groundwater modeling studies in New England," *Geophysics*, vol. 51, no. 2, pp. 236–249, 1986.

[98] G. Grelle and F. M. Guadagno, "Seismic refraction methodology for groundwater level determination:"water seismic index"," *Journal of Applied Geophysics*, vol. 68, no. 3, pp. 301–320, 2009.

[99] C.-Y. Chang, Y. Tang, C. Mok, H. Tang, M. Power, and J. Stepp, "Development of shear modulus reduction curves based on Lotung downhole ground motion data," in *Proceedings of the Second International Conference on Recent Advances in Geotechnical Earthquake Engineering and Soil Dynamics*, St. Louis, Missouri, 1991.

[100] M. Zeghal, A.-W. Elgamal, H. Tang, and J. Stepp, "Lotung downhole array II: Evaluation of soil nonlinear properties," *Journal of Geotechnical Engineering*, vol. 121, no. 4, pp. 363–378, 1995.

[101] P. M. Byrne, S.-S. Park, M. Beaty, M. Sharp, L. Gonzalez, and T. Abdoun, "Numerical modeling of liquefaction and comparison with centrifuge tests," *Canadian Geotechnical Journal*, vol. 41, no. 2, pp. 193–211, 2004.

[102] K. B. Afacan, S. Yniesta, A. Shafiee, J. P. Stewart, and S. J. Brandenberg, "Total stress analysis of soft clay ground response in centrifuge models," *Journal of Geotechnical and Geoenvironmental Engineering*, vol. 145, no. 10, p. 04019061, 2019.

[103] W. M. Isenhower and K. H. Stokoe, "Strain-rate dependent shear modulus of San Francisco Bay mud," in *Proceedings of the First International Conference on Recent Advances in Geotechnical Earthquake Engineering and Soil Dynamics*, St. Louis, Missouri, 1981.

[104] L. Matesic and M. Vucetic, "Strain-rate effect on soil secant shear modulus at small cyclic strains," *Journal of Geotechnical and Geoenvironmental Engineering*, vol. 129, no. 6, pp. 536–549, 2003.

[105] K. Tokimatsu and Y. Yoshimi, "Empirical correlation of soil liquefaction based on SPT N-value and fines content," *Soils and Foundations*, vol. 23, no. 4, pp. 56–74, 1983.

[106] X. Mei, S. M. Olson, and Y. M. Hashash, "Empirical porewater pressure generation model parameters in 1D seismic site response analysis," *Soil Dynamics and Earthquake Engineering*, vol. 114, pp. 563–567, 2018.

[107] M. Cubrinovski and K. Ishihara, "Empirical correlation between SPT N-value and relative density for sandy soils," *Soils and Foundations*, vol. 39, no. 5, pp. 61–71, 1999.

[108] H. B. Seed, R. T. Wong, I. Idriss, and K. Tokimatsu, "Moduli and damping factors for dynamic analyses of cohesionless soils," *Journal of Geotechnical Engineering*, vol. 112, no. 11, pp. 1016–1032, 1986.

[109] C.-C. Hsu and M. Vucetic, "Threshold shear strain for cyclic pore-water pressure in cohesive soils," *Journal of Geotechnical and Geoenvironmental Engineering*, vol. 132, no. 10, pp. 1325–1335, 2006.

[110] T. Park, D. Park, and J.-K. Ahn, "Pore pressure model based on accumulated stress," *Bulletin of Earthquake Engineering*, vol. 13, no. 7, pp. 1913–1926, 2015.

[111] H. B. Seed, "Representation of irregular stress time histories by equivalent uniform stress series in liquefaction analyses," Earthquake Engineering Research Center, University of California, Berkeley, Tech. Rep. EERC 75-29, 1975.

[112] N. US, "Soil mechanics design manual 7.1, NAVFAC DM-7.1," 1986.

[113] B. Hough, *Basic Soils Engineering*. New York: The Ronald Press Company, 1957.

[114] P. Domenico and M. Mifflin, "Water from low-permeability sediments and land subsidence," *Water Resources Research*, vol. 1, no. 4, pp. 563–576, 1965.

[115] J. M. Pestana, C. E. Hunt, and R. R. Goughnour, *FEQDrain: A finite element computer program for the analysis of the earthquake generation and dissipation of pore water pressure in layered sand deposits with vertical drains*. Earthquake Engineering Research Center, University of California, 1997.

[116] R. F. Scott and B. Hushmand, "Piezometer performance at Wildlife Liquefaction site, California," *Journal of Geotechnical Engineering*, vol. 121, no. 12, pp. 912–919, 1995.

[117] T. L. Holzer and T. L. Youd, "Liquefaction, ground oscillation, and soil deformation at the Wildlife Array, California," *Bulletin of the Seismological society of America*, vol. 97, no. 3, pp. 961–976, 2007.

[118] A. Brennan, N. Thusyanthan, and S. Madabhushi, "Evaluation of shear modulus and damping in dynamic centrifuge tests," *Journal of Geotechnical and Geoenvironmental Engineering*, vol. 131, no. 12, pp. 1488–1497, 2005.

[119] A. Elgamal, Z. Yang, T. Lai, B. L. Kutter, and D. W. Wilson, "Dynamic response of saturated dense sand in laminated centrifuge container," *Journal of Geotechnical and Geoenvironmental Engineering*, vol. 131, no. 5, pp. 598–609, 2005.

[120] R. Conti and G. M. Viggiani, "Evaluation of soil dynamic properties in centrifuge tests," *Journal of Geotechnical and Geoenvironmental Engineering*, vol. 138, no. 7, pp. 850–859, 2011.

[121] B. L. Kutter, "Recent advances in centrifuge modeling of seismic shaking," in *Proceedings of the Third International Conference on Recent Advances in Geotechnical Earthquake Engineering and Soil Dynamics*, St. Louis, Missouri, 1995.

[122] D. R. Legates and G. J. McCabe, "Evaluating the use of "goodness-of-fit" measures in hydrologic and hydroclimatic model validation," *Water resources research*, vol. 35, no. 1, pp. 233–241, 1999.

[123] Y. Tao and E. Rathje, "Taxonomy for evaluating the site-specific applicability of one-dimensional ground response analysis," *Soil Dynamics and Earthquake Engineering*, vol. 128, p. 105865, 2020.

[124] B. A. Bradley, "A framework for validation of seismic response analyses using seismometer array recordings," *Soil Dynamics and Earthquake Engineering*, vol. 31, no. 3, pp. 512–520, 2011.

[125] K. Konno and T. Ohmachi, "Ground-motion characteristics estimated from spectral ratio between horizontal and vertical components of microtremor," *Bulletin of the Seismological Society of America*, vol. 88, no. 1, pp. 228–241, 1998.

[126] I. Idriss, "Use of VS30 to represent local site conditions," in *Proceedings of the 4th IASPEI/IAEE international symposium. Effects of source geology on seismic motion, California, USA*, 2011.

[127] K. O. Cetin and H. T. Bilge, "Cyclic large strain and induced pore pressure models for saturated clean sands," *Journal of Geotechnical and Geoenvironmental Engineering*, vol. 138, no. 3, pp. 309–323, 2012.

[128] E. M. Rathje, F. Faraj, S. Russell, and J. D. Bray, "Empirical relationships for frequency content parameters of earthquake ground motions," *Earthquake Spectra*, vol. 20, no. 1, pp. 119–144, 2004.

[129] R. W. Jibson and D. K. Keefer, "Analysis of the seismic origin of landslides: examples from the New Madrid seismic zone," *Geological Society of America Bulletin*, vol. 105, no. 4, pp. 521–536, 1993.

[130] R. W. Jibson, E. L. Harp, and J. A. Michael, "A method for producing digital probabilistic seismic landslide hazard maps," *Engineering Geology*, vol. 58, no. 3-4, pp. 271–289, 2000.

[131] J. D. Bray and E. M. Rathje, "Earthquake-induced displacements of solid-waste landfills," *Journal of Geotechnical and Geoenvironmental Engineering*, vol. 124, no. 3, pp. 242–253, 1998.

[132] J. Wartman, J. D. Bray, and R. B. Seed, "Inclined plane studies of the newmark sliding block procedure," *Journal of Geotechnical and Geoenvironmental Engineering*, vol. 129, no. 8, pp. 673–684, 2003.

[133] S.-Y. Hsieh and C.-T. Lee, "Empirical estimation of the Newmark displacement from the Arias intensity and critical acceleration," *Engineering Geology*, vol. 122, no. 1-2, pp. 34–42, 2011.

[134] K. Chousianitis, V. Del Gaudio, I. Kalogeras, and A. Ganas, "Predictive model of Arias intensity and Newmark displacement for regional scale evaluation of earthquake-induced landslide hazard in Greece," *Soil Dynamics and Earthquake Engineering*, vol. 65, pp. 11–29, 2014.

[135] J. D. Bray and J. Macedo, "6th Ishihara lecture: Simplified procedure for estimating liquefaction-induced building settlement," *Soil Dynamics and Earthquake Engineering*, vol. 102, pp. 215–231, 2017.

[136] A. Arias, "Measure of earthquake intensity, massachusetts inst. of tech," *Cambridge. Univ. of Chile, Santiago de Chile*, 1970.

[137] B. Bradley, "Correlation of Arias intensity with amplitude, duration and cumulative intensity measures," *Soil Dynamics and Earthquake Engineering*, vol. 78, pp. 89–98, 2015.

[138] R. E. Kayen, "Assessment of liquefaction potential during earthquake by Arias intensity," in *Journal of Geotechnical and Geoenvironmental Engineering*, 1997.

[139] S. Kramer and R. Mitchell, "An efficient and sufficient scalar intensity measure for soil liquefaction," *Earthquake Spectra*, 2006.

[140] E. Harp and R. Wilson, "Shaking intensity thresholds for rock falls and slides: Evidence from 1987 Whittier Narrows and Superstition Hills earthquake strong-motion records," *Bulletin of the Seismological Society of America*, vol. 85, pp. 1739–1757, 1995.

[141] L. Cabanas, B. Benito, and M. Herraz, "An approach to the measurement of the potential structural damage of earthquake ground motions," *Earthquake Engineering & Structural Dynamics*, vol. 26, no. 1, pp. 79–92, 1997.

[142] R. I. Borja, B. G. Duvernay, and C.-H. Lin, "Ground response in Lotung: Total stress analyses and parametric studies: Total stress analyses and parametric studies," *Journal of Geotechnical and Geoenvironmental Engineering*, vol. 128, no. 1, pp. 54–63, 2002.

[143] Y. M. Hashash, S. Dashti, M. I. Romero, M. Ghayoomi, and M. Musgrove, "Evaluation of 1D seismic site response modeling of sand using centrifuge experiments," *Soil Dynamics and Earthquake Engineering*, vol. 78, pp. 19–31, 2015.

[144] H. Seed and I. Idriss, *Ground motions and soil liquefaction during earthquakes*. Oakland: Earthquake Engineering Research Institute Monograph, 1982.

[145] J. Foschaar, J. Baker, and G. Deierlein, "Preliminary assessment of ground motion duration effects on structural collapse," in *Proceedings of the 15th world conference on earthquake engineering*, 2012.

[146] R. Chandramohan, J. W. Baker, and G. G. Deierlein, "Quantifying the influence of ground motion duration on structural collapse capacity using spectrally equivalent records," *Earthquake Spectra*, vol. 32, no. 2, pp. 927–950, 2016.

[147] J. J. Moughty and J. R. Casas, "A state of the art review of modal-based damage detection in bridges: development, challenges, and solutions," *Applied Sciences*, vol. 7, no. 5, p. 510, 2017.

[148] B. Bolt, "Duration of strong ground motions," in *Fifth World Conference on Earthquake Engineering*, Rome, 1973, pp. 1304–1313.

[149] M. Trifunac and A. Brady, "A study on the duration of strong earthquake ground motion," *Bulletin of the Seismological Society of America*, vol. 65, no. 3, pp. 581–626, 1975.

[150] A. EPRI, "Criterion for determining exceedance of the operating basis earthquake. report NP-5930 2848-16," *Electric Power Research Institute, USA*, 1988.

[151] T. O'Hara and J. Jacobson, "Standardization of the cumulative absolute velocity," Electric Power Research Inst., Tech. Rep., 1991.

[152] K. Campbell and Y. Bozorgnia, "A ground motion prediction equation for the horizontal component of cumulative absolute velocity (CAV) based on the PEER-NGA strong motion database," *Earthquake Spectra*, vol. 26, no. 3, pp. 635–650, 2010.

[153] K. W. Campbell and Y. Bozorgnia, "A comparison of ground motion prediction equations for Arias intensity and cumulative absolute velocity developed using a consistent database and functional form," *Earthquake Spectra*, vol. 28, no. 3, pp. 931–941, 2012.

[154] USNRC, "Regulatory guide 1.166 pre-earthquake planning and immediate nuclear power plant operator post-earthquake actions," *US Nuclear Regulatory Commission*, 1997.

[155] S. Dashti and Z. Karimi, "Ground motion intensity measures to evaluate I: The liquefaction hazard in the vicinity of shallow-founded structures," *Earthquake Spectra*, vol. 33, no. 1, pp. 241–276, 2017. [Online]. Available: https://doi.org/10.1193/103015EQS162M

[156] Z. Karimi and S. Dashti, "Ground motion intensity measures to evaluate II: the performance of shallow-founded structures on liquefiable ground," *Earthquake Spectra*, vol. 33, no. 1, pp. 277–298, 2017. [Online]. Available: https://doi.org/10.1193/103015EQS163M

[157] Z. Bullock, S. Dashti, A. Liel, K. Porter, Z. Karimi, and B. Bradley, "Ground-motion prediction equations for Arias intensity, cumulative absolute velocity, and peak incremental ground velocity for rock sites in different tectonic environments," *Bulletin of the Seismological Society of America*, vol. 107, no. 5, pp. 2293–2309, 2017.

[158] Z. Bullock, Z. Karimi, S. Dashti, K. Porter, A. Liel, and K. Franke, "A physics-informed semi-empirical probabilistic model for the settlement of shallow-founded structures on liquefiable ground," *Géotechnique*, vol. 69, no. 5, pp. 406–419, 2018.

[159] T. Blake, R. Hollingsworth, J. Stewart, R. D'Antonio, J. Earnest, F. Gharib, L. Horsman, D. Hsu, S. Kupferman, R. Masuda *et al.*, "Recommended procedures for implementation of DMG special publication 117 guidelines for analyzing and mitigating landslide hazards in California," *Los Angeles Section Geotechnical Group, Document published by the Southern California Earthquake Center*, 2002.

[160] J. Stewart, T. Blake, and R. Hollingsworth, "A screen analysis procedure for seismic slope stability," *Earthquake Spectra*, vol. 19, no. 3, pp. 697–712, 2003.

[161] R. Green, C. Olgun, and K. Wissmann, "Shear stress redistribution as a mechanism to mitigate the risk of liquefaction," *Geotechnical Earthquake Engineering and Soil Dynamics IV (David Zeng, Majid T. Manzari, and Dennis R. Hiltunen, eds.), ASCE Geotechnical Special Publication 181*, 2008.

[162] E. M. Rathje, N. A. Abrahamson, and J. D. Bray, "Simplified frequency content estimates of earthquake ground motions," *Journal of Geotechnical and Geoenvironmental Engineering*, vol. 124, no. 2, pp. 150–159, 1998.

[163] L. G. Baise, S. D. Glaser, and D. Dreger, "Site response at treasure and Yerba Buena Islands, California," *Journal of Geotechnical and Geoenvironmental Engineering*, vol. 129, no. 5, pp. 415–426, 2003.

[164] D. M. Boore, "Can site response be predicted?" *Journal of Earthquake Engineering*, vol. 8, no. spec01, pp. 1–41, 2004.

[165] G. Zalachoris and E. Rathje, "Comparisons of one-dimensional site response analysis and borehole array observations: Quantification of bias and variability," in *Proceedings of the 6th International Conference on Earthquake Geotechnical Engineering*, 2015, pp. 1–4.

[166] A. Papazoglou and A. S. Elnashai, "Analytical and field evidence of the damaging effect of vertical earthquake ground motion," *Earthquake Engineering & Structural Dynamics*, vol. 25, no. 10, pp. 1109–1137, 1996.

[167] J. Yang and T. Sato, "Interpretation of seismic vertical amplification observed at an array site," *Bulletin of the Seismological Society of America*, vol. 90, no. 2, pp. 275–285, 2000.

[168] C. M. Mok, C.-Y. Chang, and D. Legaspi, "Site response analyses of vertical excitation," in *Geotechnical Earthquake Engineering and Soil Dynamics III Conference*, 1998.

[169] A. Elgamal and L. He, "Vertical earthquake ground motion records: an overview," *Journal of Earthquake Engineering*, vol. 8, no. 05, pp. 663–697, 2004.

[170] J. Liu, X. Zhang, Z. Cao, B. Han, and S. Yang, "Analytical solution for vertical site response analysis and its validation," *Earthquake Engineering and Engineering Vibration*, vol. 18, no. 1, pp. 53–60, 2019.

[171] I. A. Beresnev, A. M. Nightengale, and W. J. Silva, "Properties of vertical ground motions," *Bulletin of the Seismological Society of America*, vol. 92, no. 8, pp. 3152–3164, 2002.

APPENDIX A – SUPPLEMENTARY MATERIAL

Table S1 Detailed list of input motions and properties

No.	Site	#	ID/EQ	Date	Earthquake Latitude (°)	Earthquake Longitude (°)	Moment Magnitude M_w	Epicentral Distance R (km)	Maximum Observed Acceleration Surface PGA_{obs} (g)	Maximum Observed Acceleration Downhole PGA_{obs} (g)	Peak Ground Velocity Downhole PGV (m/s)	Significant Duration Downhole D_{5-95} (s)	Arias Intensity Downhole AI (m/s)	Mean Period Downhole T_m (s)	Measured Max. Pore Pressure Ratio r_{u-max} (%)	Probability of Liquefaction PL (%)	Stockwell Transform
1	**KSRH07**	1	-	2013/02/02	42.702	143.227	6.5	102	0.574	0.255	0.106	7.88	0.428	0.23	-	100	
2		2	-	2003/09/26	41.781	144.074	8.0	152	0.499	0.211	0.247	65.88	0.851	0.32	-	100	
3		3	-	2004/11/29	42.946	145.274	7.1	80	0.123	0.050	0.091	73.22	0.043	0.40	-	0	
4		4	-	2004/12/06	42.848	145.343	6.9	89	0.126	0.042	0.038	71.34	0.022	0.43	-	0	
5		5	-	2003/09/11	42.676	143.891	4.9	62	0.121	0.036	0.009	9.16	0.004	0.13	-	0	
6		6	-	2003/09/27	42.735	144.341	5.2	45	0.111	0.018	0.008	18.48	0.002	0.27	-	0	
7		7	-	2004/06/07	42.541	144.431	4.9	67	0.085	0.016	0.004	14.58	0.001	0.15	-	0	
8		8	-	2007/07/01	43.543	144.908	5.8	65	0.077	0.016	0.009	26.12	0.003	0.29	-	0	
9		9	-	2010/07/08	42.573	144.528	4.7	65	0.070	0.019	0.003	9.48	0.001	0.13	-	0	
10		10	-	2003/09/29	42.360	144.553	6.5	88	0.076	0.017	0.017	95.54	0.006	0.46	-	0	
11		11	-	2012/08/25	42.327	143.110	6.1	134	0.069	0.016	0.006	37.32	0.005	0.31	-	0	
12		12	-	2009/03/20	42.600	144.535	5.0	62	0.062	0.013	0.007	23.88	0.001	0.19	-	0	
13		13	-	2005/05/19	42.920	144.720	4.8	40	0.055	0.012	0.006	21.28	0.001	0.20	-	0	
14		14	-	2003/10/08	42.565	144.669	6.4	69	0.062	0.010	0.013	108.08	0.005	0.52	-	0	
15		15	-	2005/01/18	42.875	145.007	6.4	63	0.061	0.022	0.015	62.40	0.010	0.39	-	0	
16		16	-	2018/04/14	43.175	145.737	5.4	115	0.056	0.015	0.003	23.92	0.001	0.21	-	0	
17		17	-	2017/11/03	42.563	143.748	5.0	79	0.044	0.007	0.002	22.94	0.001	0.14	-	0	
18		18		2019/04/15	42.485	144.817	5.1	83	0.015	0.003	0.002	40.82	0.000	0.18	-	0	
19		19		2018/12/30	42.327	143.113	5.3	134	0.012	0.004	0.001	43.22	0.000	0.18	-	0	
20		20		2019/05/05	43.177	146.427	5.3	171	0.008	0.002	0.001	56.36	0.000	0.14	-	0	
21	**TCGH16**	1	-	2011/03/11	38.103	142.860	9.0	301	1.126	0.176	0.299	57.74	1.007	0.45	-	100	x
22		2	-	2011/03/11	36.108	141.265	7.7	117	0.349	0.074	0.067	27.26	0.069	0.41	-	100	
23		3	-	2011/04/11	36.945	140.672	7.0	69	0.260	0.042	0.066	39.08	0.049	0.42	-	90	
24		4	-	2011/03/19	36.783	140.570	6.1	51	0.214	0.028	0.019	23.10	0.008	0.31	-	38	
25		5	-	2012/12/07	38.018	143.867	7.3	374	0.180	0.023	0.031	93.54	0.018	0.53	-	51	
26		6	-	2016/11/22	37.353	141.603	7.4	163	0.172	0.024	0.040	85.94	0.017	0.69	-	47	
27		7	-	2011/03/14	36.458	141.125	6.2	95	0.112	0.016	0.023	19.72	0.006	0.47	-	0	
28		8	-	2011/04/16	36.340	139.945	5.9	26	0.126	0.026	0.021	33.44	0.005	0.42	-	0	
29		9	-	2008/05/08	36.227	141.607	7.0	142	0.136	0.023	0.025	41.74	0.009	0.55	-	9	
30		10	-	2008/08/22	36.442	140.615	5.2	50	0.139	0.022	0.007	13.16	0.002	0.21	-	0	
31		11	-	2011/03/23	37.063	140.770	5.8	84	0.132	0.013	0.007	16.70	0.002	0.30	-	1	
32		12	-	2011/04/07	38.203	141.920	7.1	246	0.122	0.018	0.024	80.66	0.012	0.48	-	4	
33		13	-	2011/07/31	36.902	141.220	6.5	110	0.106	0.016	0.020	49.32	0.007	0.34	-	0	
34		14	-	2011/04/19	36.168	139.807	5.0	49	0.084	0.012	0.006	17.38	0.001	0.16	-	0	
35		15	-	2016/08/19	36.56	141.132	5.4	95	0.071	0.007	0.004	19.04	0.001	0.19	-	0	
36		16	-	2019/01/14	36.162	139.810	4.9	49	0.061	0.011	0.003	16.34	0.001	0.14	-	0	
37		17	-	2017/01/05	36.862	140.978	5.3	88	0.050	0.005	0.002	21.40	0.000	0.15	-	0	
38		18	-	2016/08/15	37.378	141.748	5.6	175	0.019	0.004	0.002	40.48	0.000	0.17	-	0	
39		19	-	2018/07/07	35.165	140.592	6.0	160	0.017	0.003	0.005	71.02	0.000	0.69	-	0	
40		20	-	2017/09/20	37.277	141.652	5.3	162	0.010	0.002	0.001	46.40	0.000	0.31	-	0	
41	**WLA**	1	-	1987/11/23	33.083	-115.775	6.2	15.6	0.131	0.072	0.069	15.44	0.080	0.42	10	33	
42		2	-	1987/11/24	33.022	-115.831	6.6	21.9	0.201	0.171	0.216	28.98	0.579	0.54	100	96	x
43		3	-	2012/08/27	33.021	-115.519	4.9	8.58	0.295	0.236	0.141	5.70	0.119	0.34	74	100	x
44		4	-	2012/08/26	33.028	-115.531	4.6	7.74	0.266	0.179	0.092	4.76	0.066	0.28	67	100	x
45		5	-	2012/08/26	33.019	-115.450	5.4	8.78	0.184	0.085	0.057	25.74	0.075	0.31	16	88	x
46		6	-	2012/08/26	33.016	115.536	4.6	9.23	0.072	0.038	0.019	24.32	0.011	0.25	5	0	
47		7	-	2005/09/01	33.178	-115.633	4.8	13.1	0.057	0.028	0.035	25.24	0.019	0.38	3	0	
48		8	-	2005/09/02	33.175	-115.631	4.5	12.74	0.095	0.048	0.044	19.08	0.035	0.38	6	0	
49		9	-	2009/12/30	32.464	-115.189	5.8	77.43	0.073	0.032	0.032	101.24	0.034	0.65	2	0	
50		10	-	2010/06/15	32.700	-115.921	5.7	57.36	0.055	0.029	0.033	101.72	0.023	0.63	2	0	
51		11	-	2010/06/15	33.017	-115.554	5.7	59.12	0.167	0.090	0.060	22.14	0.055	0.31	19	77	
52		12	-	2016/06/10	33.431	-116.443	5.2	92.66	0.013	0.007	0.006	90.84	0.002	0.55	4	0	
53		13	-	2012/08/26	33.014	-115.559	4.9	9.67	0.122	0.051	0.029	31.82	0.023	0.31	8	19	
54		14	-	2005/08/31	33.172	-115.612	4.5	11.25	0.067	0.052	0.056	16.92	0.025	0.41	6	0	
55		15	-	2010/12/15	33.033	-115.543	4.4	7.27	0.033	0.014	0.006	17.92	0.002	0.21	3	0	
56		16	-	2005/08/31	33.198	-115.589	4.3	12.45	0.042	0.016	0.014	31.86	0.004	0.40	2	0	
57		17	-	2010/04/05	32.664	-115.809	4.9	54.83	0.031	0.016	0.008	87.12	0.002	0.49	1	0	
58		18	-	2016/07/31	32.958	-115.760	4.0	26.45	0.018	0.013	0.010	33.12	0.002	0.57	8	0	
59		19	-	2008/02/12	32.447	-115.317	5.0	75.12	0.010	0.005	0.003	107.88	0.001	0.54	0	0	
60		20		2010/04/27	32.692	-115.847	4.8	53.97	0.013	0.006	0.003	85.28	0.001	0.48	0	0	
61	**CSP3**	1	Santa Cruz	-	-	-	6.9	-	0.020	0.009	0.004	34.93	0.001	0.31	6	0	
62		2	Santa Cruz	-	-	-	6.9	-	0.066	0.036	0.020	14.95	0.010	0.36	5	0	
63		3	Santa Cruz	-	-	-	6.9	-	0.060	0.027	0.017	12.13	0.008	0.39	4	0	
64		4	Santa Cruz	-	-	-	6.9	-	0.873	0.480	0.221	8.99	1.346	0.35	100	100	x
65		5	Kobe	-	-	-	6.9	-	0.999	0.219	0.252	8.00	0.717	0.53	100	96	x
66		6	Santa Cruz	-	-	-	6.9	-	0.202	0.105	0.058	10.22	0.063	0.38	55	13	
67		7	Santa Cruz	-	-	-	6.9	-	0.742	0.397	0.277	18.87	1.604	0.49	100	100	x
68		8	Santa Cruz	-	-	-	6.9	-	0.187	0.101	0.094	18.72	0.119	0.51	44	13	
69		9	Kobe	-	-	-	6.9	-	1.122	0.596	0.428	8.58	4.142	0.50	100	100	x
70		10	Santa Cruz	-	-	-	6.9	-	1.079	0.534	0.230	9.41	1.639	0.36	95	100	x
71		11	Santa Cruz	-	-	-	6.9	-	0.015	0.007	0.003	27.10	0.000	0.33	2	0	
72		12	Kobe	-	-	-	6.9	-	0.074	0.037	0.032	7.97	0.016	0.48	6	0	
73		13	Kobe	-	-	-	6.9	-	0.067	0.026	0.024	7.98	0.009	0.52	4	0	
74		14	Kobe	-	-	-	6.9	-	0.202	0.219	0.193	7.98	0.669	0.53	72	12	
75	**CFF2**	1	Joshua-L	-	-	-	6.9	-	0.027	0.016	0.018	26.47	0.005	0.54	5	0	
76		2	Kobe-L	-	-	-	6.9	-	0.096	0.355	0.448	11.55	2.161	0.66	100	0	x
77		3	Joshua-H	-	-	-	6.9	-	0.088	0.463	0.370	26.51	9.058	0.52	100	0	x
78		4	Northridge	-	-	-	6.9	-	1.674	0.835	0.567	16.42	6.435	0.68	100	100	x
79		5	Kobe-H	-	-	-	6.9	-	0.451	0.776	0.542	25.81	13.576	0.57	100	70	x
80		6	Joshua-H2	-	-	-	6.9	-	0.520	0.759	0.514	27.55	13.802	0.58	100	87	x
81	**LSST**	1	LSST4	1986/01/16	24.77	121.99	6.5	23.8	0.263	0.380	0.135	4.52	0.136	0.40	-	100	x
82		2	LSST5	1986/03/29	24.60	131.82	4.7	8.5	0.042	0.016	0.005	7.09	0.001	0.21	-	0	
83		3	LSST6	1986/08/04	24.39	121.79	5.4	31.4	0.036	0.013	0.014	13.04	0.002	0.33	-	0	
84		4	LSST7	1986/05/20	24.09	121.60	6.5	66.2	0.208	0.099	0.110	12.97	0.071	0.77	-	100	x
85		5	LSST8	1986/05/20	24.06	121.62	6.2	69.2	0.036	0.014	0.012	11.00	0.002	0.40	-	0	
86		6	LSST9	1986/11/07	24.63	121.79	4.5	5	0.072	0.029	0.013	2.16	0.002	0.18	-	0	
87		7	LSST10	1986-16-07	24.61	131.78	4.5	6.1	0.040	0.020	0.008	4.42	0.001	0.17	-	0	
88		8	LSST11	1986/07/17	24.67	121.83	5.0	6	0.104	0.062	0.020	2.87	0.011	0.18	-	22	
89		9	LSST12	1986/07/30	24.64	121.80	6.2	6.2	0.190	0.221	0.108	6.27	0.152	0.31	27	100	x
90		10	LSST13	1986/07/30	-	-	6.2	-	0.050	0.034	0.012	15.56	0.004	0.23	-	0	
91		11	LSST14	1986/08/05	24.64	121.80	4.9	4.7	0.050	0.030	0.014	2.97	0.002	0.17	-	0	
92		12	LSST15	1986/11/14	24.62	121.78	4.9	4.9	0.100	0.091	0.018	1.68	0.006	0.18	-	14	
93		13	LSST16	1986/11/14	24.97	121.84	7.0	77.9	0.171	0.085	0.200	27.60	0.207	0.62	27	100	x
94		14	LSST17	1986/11/14	24.00	121.84	7.0	77.9	0.038	0.026	0.088	16.16	0.020	0.78	-	0	
95		15	LSST18	1986/11/15	24.87	121.82	4.0	77.9	0.028	0.009	0.023	13.81	0.003	0.70	-	0	
96	**PIDA**	1	-	1994/11/09	34.92	135.39	4.0	32.6	0.004	0.003	0.001	8.16	0.000	0.23	0	0	
97		2	-	1995/01/17	34.60	135.04	6.9	17.8	0.348	0.688	0.665	9.08	2.599	0.50	100	100	x
98		3	-	1995/02/04	34.73	135.27	3.4	8.4	0.010	0.004	0.001	7.92	0.000	0.11	0	0	

Table S2 Effective Stress Analysis – List of the calibrations for all sites

Model	ID	f α α α s	p $Dr(\%)$ β β r	F $FC(\%)$ $D_{ru=1.0}$ - A	s - CSR_t - B	Y_{rup} - - - C	v v v v D	- - - - Y_{typ}	c_v	Boundary condition (I: Impermeable, P: Permeable)	Clay Model	SITES						
												KSRH07	TCGH16	WLA	CSP3	CFF2	LSST	PIDA
Dobry & Matasovic (1988)	**M1.1**	1	1	*	f(FC<5)	0.01	1	-	f(FC<5)	I	Matasovic and Vucetic (1995)	x	x	x	x	x	x	x
	M1.2	1	1	*	f(FC<5)	*	2.5	-	f(FC<5)	I		x	x	x	x	x	x	x
	M1.3	1	1	*	f(FC=15)	*	1	-	f(FC=15)	I		x	x	-	-	-	-	-
	M1.4	1	1.07	*	f(FC<5)	*	1	-	f(FC<5)	I		x	x	x	-	-	-	-
	M1.5	1	1	Mei (18) $c_{u\text{-}mes\ or\ 1.4}$	f(FC<5)	*	1	-	f(FC<5)	I		x	x	x	x	x	x	x
	M1.6	1	1.04	2.6	1.7	*	1	-	f(FC<5)	I		-	-	x	-	-	-	-
	M1.7	1	1	*	f(FC<5)	*	5	-	f(FC<5)	I		x	x	x	x	x	x	x
	M1.8	1	1	*	f(FC<5)	*	1	-	f(FC<5)	P		-	-	x	-	-	x	x
	M1.9	1	1	Mei (18) cu=3.8	f(FC<5)	*	1	-	f(FC<5)	I		x	x	-	-	-	x	x
	M1.10	1	1	*	f(FC<5)	*	1	-	f(FC<5)	I		x	x	x	x	x	x	x
Green-Mitchell-Polito (GMP) (2000)	**M2.1**	1	*	FC<5	-	-	1	-	f(FC<5)	I		x	x	x	x	x	x	x
	M2.2	2	*	FC<5	-	-	1	-	f(FC<5)	I		x	x	x	x	x	x	x
	M2.3	1	*	FC<5	-	-	2.5	-	f(FC<5)	I		x	x	x	x	x	x	x
	M2.4	1	*	FC=15	-	-	1	-	f(FC=15)	I		x	x	-	-	-	-	-
	M2.5	1	*	FC<5	-	-	5	-	f(FC<5)	I		x	x	x	x	x	x	x
	M2.6	1	*	FC<5	-	-	1	-	f(FC<5)	P		-	-	x	-	-	x	x
Park & Ahn (2013)	**M3.1**	*	0.7	*	*	-	1	-	f(FC<5)	I		x	x	x	x	x	x	x
	M3.2	*	1.4	*	*	-	1	-	f(FC<5)	I		x	x	x	x	x	x	x
	M3.3	*	0.7	*	*	-	1	-	f(FC=15)	I		x	x	-	-	-	-	-
	M3.4	*	0.7	*	*	-	1	-	f(FC<5)	I		x	x	-	x	x	x	x
	M3.5	*	0.7	*	*	-	2.5	-	f(FC<5)	I		x	x	x	x	x	x	x
	M3.6	*	0.7	*	*	-	5	-	f(FC<5)	I		x	x	x	x	x	x	x
	M3.7	*	0.7	*	*	-	1	-	f(FC<5)	P		-	-	x	-	-	x	x
	M3.8	*	Polito (2008)	*	*	-	1	-	f(FC<5)	I		x	x	x	x	x	x	x
Generalized (1985)	**M4.1**	f(PEC)	0.5	-	-	-	1	-	f(FC<5)	I		x	x	x	x	x	x	x
	M4.2	f(PEC)	1.4	-	-	-	1	-	f(FC<5)	I		x	x	x	x	x	x	x
	M4.3	f(PEC)	0.5	-	-	-	2.5	-	f(FC<5)	I		x	x	x	x	x	x	x
	M4.4	f(PEC)	0.5	-	-	-	1	-	f(FC=15)	I		x	x	-	-	-	-	-
	M4.5	1	0.5	-	-	-	1	-	f(FC<5)	I		x	x	x	x	x	x	x
	M4.6	f(PEC)	0.5	-	-	-	5	-	f(FC<5)	I		x	x	x	x	x	x	x
	M4.7	f(PEC)	0.5	-	-	-	1	-	f(FC<5)	P		-	-	x	-	-	x	x
Clay: Generalized Sand: Generalized	**M5.1**	f(PEC)	0.5	-	-	-	1	-	f(FC<5)	I	General.	-	x	x	-	-	x	x
	M5.2	1	0.5	-	-	-	1	-	f(FC<5)	I		-	x	x	-	-	x	x
	M5.3	0.15	0.5	-	-	-	1	-	f(FC<5)	I		-	x	x	-	-	x	x

*See Section 4.2 for more details

ADDITIONAL NOTES			
Calibration	KSRH07, TCGH16, CSP3, CFF2	WLA	LSST, PIDA
M3.1	Kayen	CPT	SPT
M3.2	Kayen	CPT	SPT
M3.3	Kayen	CPT	SPT
M3.4	Andrus	Kayen	SPT
M3.5	Kayen	CPT	SPT
M3.6	Kayen	CPT	SPT
M3.7	Kayen	CPT	SPT
M3.8	Kayen	CPT	SPT

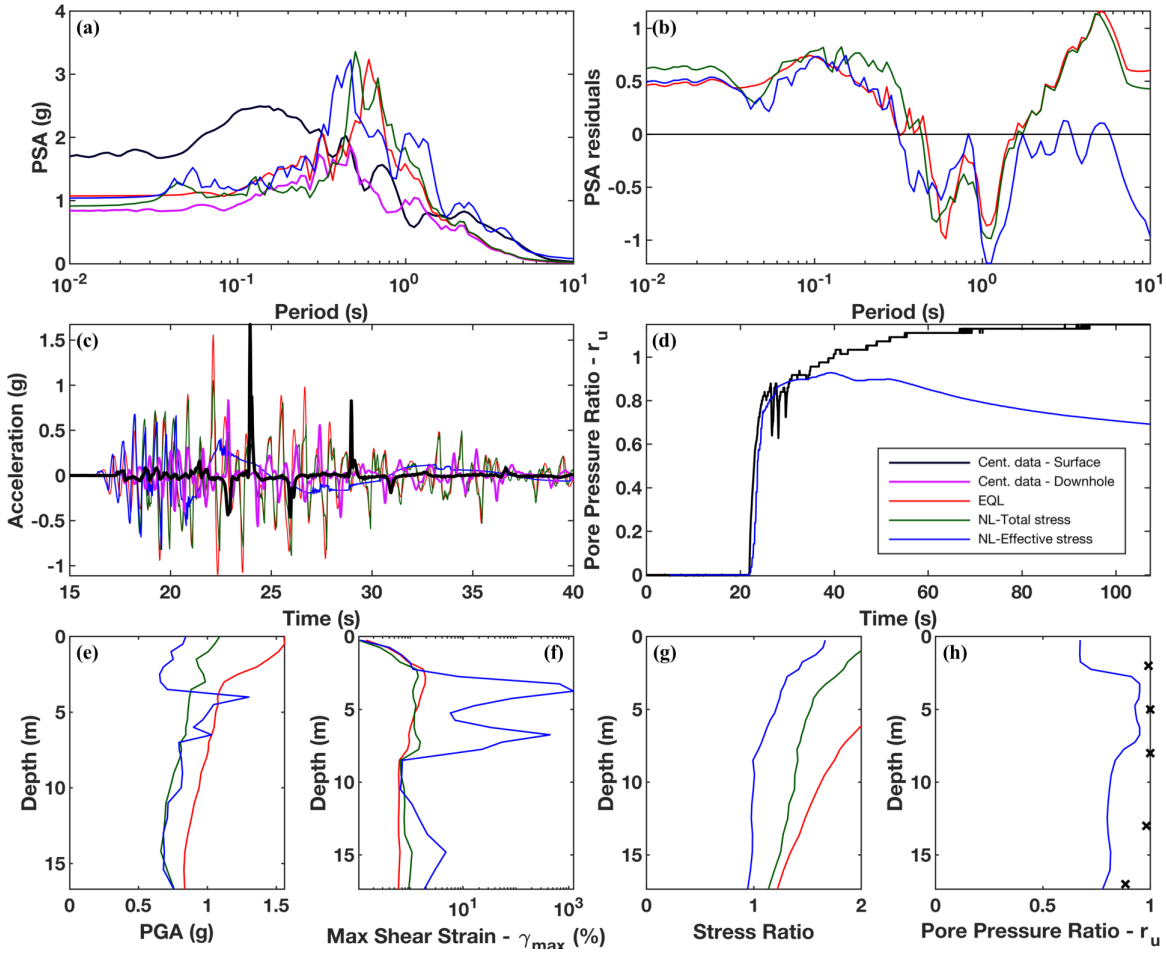


Figure S1 Results from total stress equivalent-linear (EQL), total stress nonlinear (NL-TS) and effective stress nonlinear (NL-ES) analysis with the Dobry and Matasovic model (M1) and calibration M1.1 for EQ#4 of centrifuge test CFF2: (a) Pseudo-acceleration surface response spectra, (b) Response spectra residuals, (c) Surface acceleration time histories for NS direction, (d) Pore pressure response at 5m depth, (e) Peak ground acceleration profile, (f) Maximum shear strain profile, (g) Stress ratio profile and (h) Pore pressure ratio profile for the NL-ES analysis.

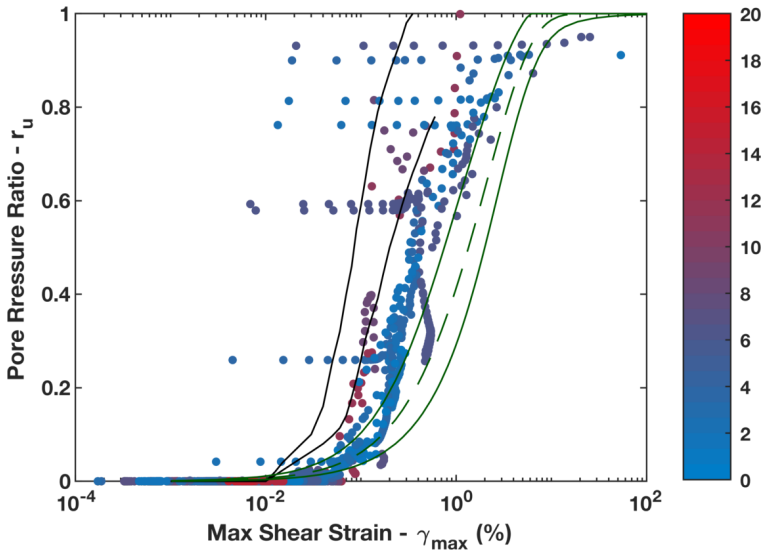


Figure S2 Pore pressure response vs the maximum computed shear strain for the Generalized model calibration M1.5.

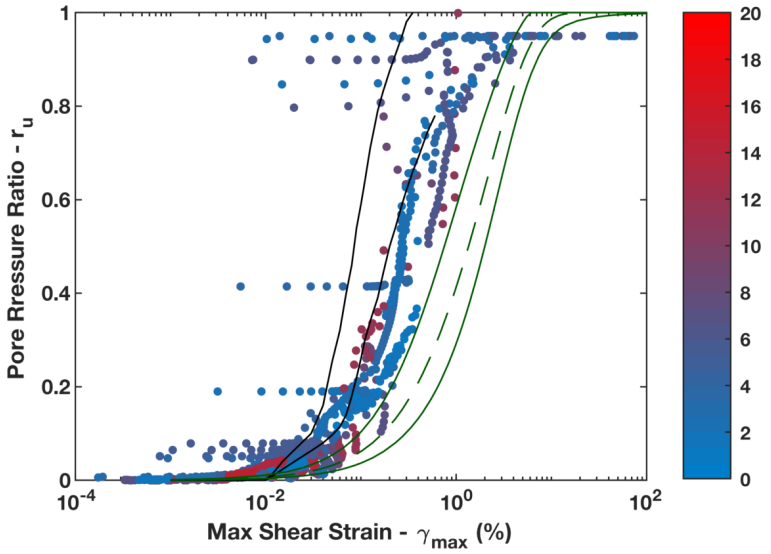


Figure S3 Pore pressure response vs the maximum computed shear strain for the Dobry and Matasovic model calibration M4.5.